POLITECNICO

MILANO 1863

SCHOOL OF INDUSTRIAL AND INFORMATION ENGINEERING

MASTER OF SCIENCE IN AERONAUTICAL ENGINEERING

DEPARTMENT OF AEROSPACE SCIENCE AND TECHNOLOGY

Numerical modeling and wind tunnel testing of an aeroelastic model equipped with active flutter suppression systems

Author:

Domenico DI LEONE -
905362
Francesco LO BALBO -
899550

Advisor:

Sergio RICCI
Co-Advisor:

A. DE GASPARI
P. MANTEGAZZA

Abstract

This work presents the analyses and tests carried out on an aeroelastic model representing a conventional passenger transport aircraft. The activities and results collected are part of the Active Flutter Suppression (AFS) project in cooperation between University of Washington and Politecnico di Milano. The aim of the project is the setup and the experimental validation of an accurate aeroelastic model to investigate and validate technologies for active flutter suppression. This work includes experimental and numerical analyses and the related correlations as well as the results of the tests undertaken in the last wind tunnel session in the Galleria del Vento Politecnico di Milano (GVPM), during the last week of January 2020 with the X-DIA model, in open and closed loop configurations. Finally, the lessons learned based on the obtained results and the possible future improvements and implementations are also reported.

Keyword: Aeroservoelastic Model, Flutter Instability, Correlation Techniques, Optimization Process, Wind Tunnel Test, Active Flutter Suppression, Optimal Control.

Sommario

Questo lavoro presenta le analisi e le prove eseguite su un modello aeroelastico che rappresenta un velivolo convenzionale da trasporto passeggeri. Le attività ed i risultati raccolti sono nell'ambito del progetto di soppressione di flutter per mezzo di tecnologie di controllo attivo (AFS) in collaborazione tra la University of Washington e il Politecnico di Milano. L'obiettivo del progetto è l'installazione e la validazione sperimentale di un modello aeroelastico accurato per studiare e validare tecnologie per la soppressione attiva del flutter. Questo lavoro include analisi sperimentali e numeriche e le relative correlazioni, nonché i risultati dei test effettuati nell'ultima sessione di prove in galleria del vento presso il Politecnico di Milano (GVPM), durante l'ultima settimana di gennaio 2020 con il modello X-DIA, in configurazioni ad anello aperto e chiuso. Infine, viene riportato quanto appreso in base ai risultati ottenuti e i possibili lavori ed implementazioni future.

Parole Chiave: Modello Aeroservoelastico, Instabilità di Flutter, Tecniche di Correlazione, Processo di Ottimizzazione, Prove in Galleria del Vento, Soppressione di Flutter con Controllo Attivo, Controllo ottimo.

Ringraziamenti

Desideriamo ringraziare il professor Ricci, nonostante la nostra inesperienza è riuscito a guidarci nel cammino di tesi con semplicità e con i giusti consigli al momento giusto. Grazie perchè in modo simpatico e pungente è riuscito a farci crescere in questo percorso e a farci diventare un po' più ingegneri. Grazie per la grande opportunità di lavorare al suo fianco e in un team così assortito, con cui ci siamo goduti ogni istante e momento sia a livello ingegneristico che umano. Grazie per le battute sempre pronte, abbiamo sempre apprezzato.

Immancabile e neccasario il ringraziamento per il professor De Gaspari, la sua gentilezza e disponibilità ci ha fatto sempre sentire accompagnati e desiderosi di portare a termine il nostro lavoro al meglio. Grazie per averci aiutato nella prima grande parte del lavoro, anche quando non c'è più stata l'opportunità di interfacciarsi è stato sempre un punto di riferimento. Ma soprattutto, grazie per l'amicizia.

Un ringraziamento particolare va al professor Bindolino, uomo di una sapienza e pazienza gigantesca. Sempre disponibile nell'accoglierci e nel condividere la sua enorme esperienza. Grazie perchè è riuscito nell'arduo compito di aiutarci non in una ma in ben due tesi: questa e Costruzioni Aerospaziali. Grazie per i pomeriggi interi nel suo ufficio.

Grazie al professor Mantegazza, seppur arrivato tardi nel nostro percorso è stato dirompente. Il suo contributo è stato fondamentale per l'ultima parte del lavoro, la ringraziamo per le intere lezioni tenute via mail. Grazie perchè ha sempre un libro da consigliare e grazie per aver cura della nostra 'cassetta degli attrezzi', ne faremo buon uso. Proviamo un'immensa stima nei suoi confronti.

Un dovuto ringraziamento va a Luca Marchetti, persona di una disponibilità infinita, sempre pronto ad aiutarci e illustrarci ogni singolo pezzo del X-DIA. Grazie a Luca Riccobene e Donato Grassi, avete allietato le settimane in galleria con la vostra simpatia. Grazie per averci fatto scoprire e affascinare all'aspetto tecnico di tutto questo lavoro.

A special thanks goes to John Berg and Sohrob Mottaghi. Thanks for the

company during the test week and for being guided by two young engineers to discover Milan. We hope that the memory of match at San Siro could accompany you for long time.

Grazie a Toffol e a Fonte, che abbiamo avuto modo di conoscere attraverso i loro fantastici script. Grazie perchè anche se non c'è stato modo di conoscersi meglio siete stati un grande aiuto per il conseguimento del nostro percorso.

Contents

List of Figures

List of Tables

Chapter 1

Introduction

Modern aircraft with the evolution of their traditional characteristics have now reached an optimal point. The overcoming of this excellent is now linked to the use of unconventional configurations not yet analyzed, innovative technologies or in the possibility of exceeding the characteristic limits of the envelope of an aircraft until reaching speeds considered so far taboo like that of *flutter* instability.

In addition, the search for greater structural flexibility in the future can no longer be separated from integration with Active Control (AC) technologies, which allow exploiting aeroelastic phenomena to improve aircraft performance. In the same way, aircraft over the years increasingly meet the need for weight reduction and with this the lightening of the structure. A lighter structure is more flexible, and increasingly long, light and flexible components are highly subject to instability phenomena such as that of the flutter.

According to Frazer et al. [6]: *In the practical sense "flutter" means an oscillation which grows, and finally either breaks the structure or remains bounded at some amplitude whose value is dependent upon the departure from linear laws.*

The flutter phenomenon could arise on a wing of an airplane but also on the blade of a turbine or any other structural component subject to the flow of a fluid that interacts with its dynamic behavior.

The research tries to move towards aircraft made, for example, of composite material, therefore subject to the characteristics listed, with a significant reduction in terms of weight. But the developments of the capabilities and reliability of aircraft control system hardware and software (the appearance of high-bandwidth actuators and developments in control systems theory) permits to avoid powerful but complex multidisciplinary optimization techniques (an example [18]) that do not leave residual design freedom, and to

obtain significant weight savings. So, these improvements seem to have made the implementation of Active Flutter Suppression (AFS) technology closer than ever before.

If used from the start of the design process, the technology is a key element in multidisciplinary design optimization that could lead to more efficient aircraft [9]. It will therefore be essential to study the current state of the art of AFS systems, taking into account the uncertainty, reliability and safety of the systems on the aircraft in which they have been installed.

The Politecnico di Milano (PoliMI) in the mid-2000s generated a scale model, with specific aeroservoelastic specifications, for the study of active control on a three-surface passenger transport aircraft with the aim of studying active control systems through tests in the tunnel at low speeds [10]. The model now used and in analysis is subsequent to the one mentioned above and represents its evolution for the study of control systems for the suppression of flutter in aircraft. The basic concept behind the modifications from the previous model is to make it representative in complexity and aeroelastic feature to real aircraft and also to have a model with aeroelastic characteristics defined prone to flutter in order to easily carry out such as stability analysis.

The project in which this work took place is done in collaboration with the University of Washington, as Principal Investigator and is sponsored by the Federal Aviation Administration (FAA) with the aim of investigating the possible adoption of active flutter control technologies and how to include them in the future regulations.

The FAA (`https://www.faa.gov/`) is a governmental body of the United States with powers to regulate all aspects of civil aviation in that nation as well as over its surrounding international waters. Its powers include the construction and operation of airports, air traffic management, the certification of personnel and aircraft, and the protection of U.S. assets during the launch or re-entry of commercial space vehicles.

The objectives of this work are: at first the realization of a well-correlated Finite Element Method (FEM) model representing the real eXperimental Dipartimento di Ingegneria Aerospaziale (X-DIA); second, the design of a controller based on the features of the numerical model of the first point, robust enough to bridge the uncertainties that can occur (flight conditions, manufacturing deviations, gaps between FEM model and the real one, etc.) and its validation through wind tunnel tests made.

1.1 Outline

This thesis work is divided into three parts, which analyses in detail the problems related to the numerical design of the reference aircraft, the active control design and the wind tunnel tests:

- **Chapter [2]** describes the background activities from which this work starts: the modified X-DIA aeroservoelastic model in detail, regarding configuration, construction, instrumentation and aeroservoelastic characteristics and reports the first analysis results of a stick model developed with MSC/NASTRAN which will be compared at a later stage with wind tunnel test results. Stick model main features are highlighted in this chapter with the related modeling hypotheses and model simplifications.

- **Chapter [3]** It contains all the laboratory and wind tunnel activities carried out before the last session of January 2020 and their results. At the end a brief comparison with the stick model already described in the previous chapter and the results obtained during the tests are presented.

- **Chapter [4]** It contains the correlation process made to align the FEM model output results to experimental tests ones.
  This chapter illustrates the changes made on the mathematical model during correlation and updating stage: the aircraft passes from a beam description, a simple choice that aims to the knowledge of the overall behavior of the structure, and arrives at a detailed model for the main component under analysis: the wing.

  The update improves the correlation on the dynamic behavior of the model that reaches its final configuration. This will be used in the next chapter for the realization of the flutter controller (AFS).

- **Chapter [5]** it focuses on the presentation of active control systems used and on their brief description.

- **Chapter [6]** The main topic is the latest January 2020 wind tunnel tests. It completes the wind tunnel tests of the chapter 3.
  Excitation types, simulink schemes of various blocks representing the transfer functions used and the list of the latest tests and their meaning are described here.

- **Chapter [7]** It is the final part and focuses on the comparison between data of the experimentation in the wind tunnel and extracted through

numerical simulations. The Simulink modeling scheme, reproducing the wind tunnel tests, is briefly described. The presentation of the results of some of the tests of chapter 6 are studied through an identification phase and a stability analyses of the closed-loop system.

- **Chapter [8]** closes the work with some comments on the results and a description of possible future works or improvements.

Chapter 2

Background

The eXperimental Dipartimento di Ingegneria Aerospaziale (X-DIA) model was initially conceived by POLIMI to study different topics concerning flight mechanics, aeroelasticity and active control. Its configuration can be subject to variations according to the purposes.

Figure 2.1: Wind tunnel configuration of the old X-DIA model.

The experimental model adopted in the present work is designed for AFS with characteristics suitable for the study of the flutter phenomenon and its analysis. The aim of the study is the validation of flutter suppression technologies and the impact of uncertainties on AFS performance and reliability.

The final model shows a more conventional configuration with a low positive arrow wing and a T-tail without the presence of the canard. The structural properties are based on already available components, and for new ones, they are estimated on the manufacturing technologies adopted, briefly described in the following sections.

The main characteristics of the new configuration chosen are shown in fig.2.2, taken from the MSC/NASTRAN stick model in figure, procedure illustrated in [4].

The description of the hypotheses and the structure and implementation of the simplifying model will be described in detail.

Table 1		
Mass	20.8	kg
x_{cg}	-0.389	m
y_{cg}	0	m
z_{cg}	-0.0276	m
I_{xx}	4.976	kgm^2
I_{yy}	12.082	kgm^2
I_{zz}	15.658	kgm^2
I_{xz}	1.519	kgm^2
span	3.0	m
chord	0.25	m

Table 2	
$C_{L/\alpha}$	6.13
$C_{mcg/\alpha}$	-4.65
$C_{L/\delta elev}$	0.67
$C_{mcg/\delta elev}$	-3.47
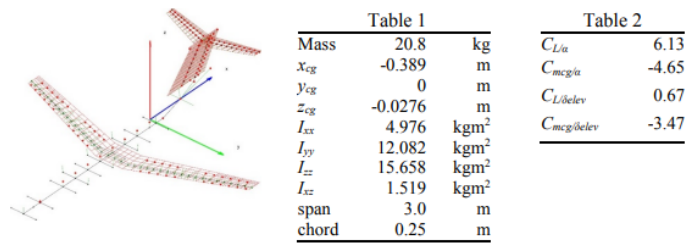
Figure 2.2: Aerolastic model X-DIA - main features - aerodynamic derivatives.

The following section will describe the modified X-DIA model in detail, with reference to the configuration, construction, instrumentation and aerolastic characteristics, reporting the results of the tests carried out in the wind tunnel.

2.1   Description of real model

The current X-DIA configuration is described in its peculiar features, highlighting structural modifications and added elements to carry out the experimental flutter tests. Tools and equipment used in order to collect data, to drive control surfaces in the desired way, to create conditions of stiffness and elasticity suitable for analysis purposes, and safety systems for the integrity of the model will be presented.
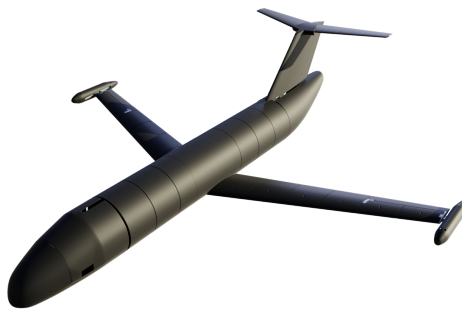
Figure 2.3: X-DIA configuration used in tests.

2.1.1 Structure

The skeleton of the X-DIA model is composed of aluminum beams connected to each other. The fuselage beam part is in a tubular structure with rectangular aluminum section.

The aluminum beam of the wing spar has an omega shape, while the vertical and the horizontal ones are cross-shaped. Connections of structural elements are designed and milled from aluminum blocks.

At the rear of the fuselage, a single aluminum frame connects the T-tail and the fuselage spar.
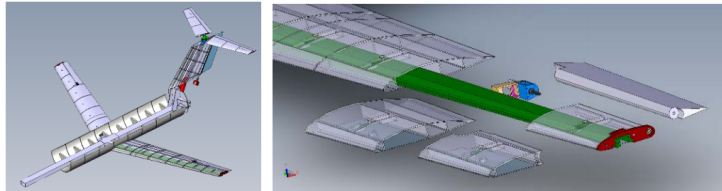
Figure 2.4: Main skeleton and wing detail.

In the detail of fig.2.4 there is represented the aileron, the motor that drives the surface motion, the part of the spar involved in its connection and the aerodynamic boundary sectors.
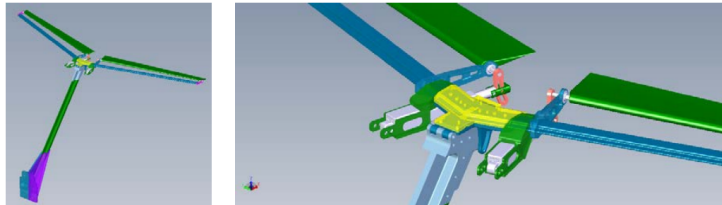
Figure 2.5: Details of tail structure and elevator execution.

In fig.2.5 there is the tailplane with vertical and horizontal stabilizers, with a zoom on the attacks of the horizontal one, where there is the actuation that allows the movement of the elevator.

2.1.2 Aerodynamic sectors and Components

One of the main components are the aerodynamic sectors. They are designed with two main purposes: to guarantee aerodynamic shapes, with enough stiffness, and to guarantee sufficient space for the installation of the instrumentation.

The contribution of the aerodynamic shape must be limited to the added masses, without altering the stiffness distribution designed for an already defined aeroelastic target. For this reason, all aerodynamic cover is splitted in smaller sectors and each one connected to the main beam in a single position along the wingspan. In this way, their stiffness contribution is negligible and the spar is the main responsible of the stiffness of the wing.

In the case of the wing and the horizontal plane, the aerodynamic sectors are produced in a block joined by 3D printer technology using a special material called X-Form, which combines high stiffness and low density. It also guarantees a smooth external surface. The wing sectors are designed to include elements for the connection with the spar, and in the case of control surfaces, for hinges and electronic motors.

Figure 2.6: Right wing, left wing, ailerons and spars.

In fig.2.6 it is possible to distinguish the sectors of each wing, six on the right and six on the left. The wing is tapered, so the chord length is variable along the opening and the last two sectors of each wing are cut to leave room for the insertion of the aileron. The chord point where the sectors attach to the spar, the internal structure of the profile with the spaces necessary to pass the cables of accelerometers and instrumentation and the cavity for inserting the spar are also visible.

The aerodynamic sectors of the vertical surfaces are in Styrofoam covered with carbon fibers. Finally, those of the fuselage are in honeycomb, also covered with carbon fibers. The distinctive elements of these sectors are in fig.2.7.

The same construction logic of the wing is implemented also for the fuselage, with a spar which performs the main structural and stiffness functions.

Figure 2.7: Vertical and fuselage sectors.

In addition, among the latest changes made to the new X-DIA model, there is a safety device placed in view of the flutter instability tests in the wind tunnel. This system allows to change the mass configuration of the aircraft and move the instability speed to higher values, so as to make the system damped again and regain control. Internally, the device contains a little mass of 200 gr sliding from two on-off positions (respectively forward and backward) thanks to a guide and a pneumatic actuation system. The slide length of the mass is about 15 cm.
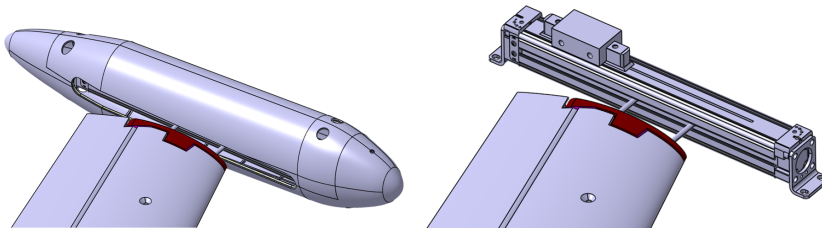
Figure 2.8: Anti-flutter device (internal and external view).

In order to be able to carry out correct modal analyses, it is decided to hang the aircraft in the tunnel using an elastic fixing system, a free-free constraint. A constraint of this type is used so that the structure can manifest some of the rigid body modes. This typology works all the better as it is possible to keep the rigid body mode band (at low frequencies) separated from the deformable one.

Figure 2.9: Free-free constraint in the wind tunnel.

2.1.3 Electronic devices

Inside the wind tunnel, the dimensions are limited and it is not easy finding an adequate actuation system to be inserted within the different sectors, in order to deflect the control surfaces. One of the features required within a tunnel test with a scaled model is to minimize the size of the devices.

Control surfaces It is decided to have the possibility to choose between a combined or separate movement of the control surfaces of the ailerons. As regards the elevator and the rudder, a control system is present, but it is not of particular interest for the aim of this thesis work.
This is accomplished through the use of a fully integrated system: sensors, control logic, electronics and pc for data processing.

Another requirement for an aileron actuation system is the need for a pass-band capable of exciting and controlling the structure modes relevant in flutter analysis. The aileron and rudder control system is based on Harmonic Drive electric motors connected to the control surfaces by means of elastic joints. For the excursion of the elevator, however, it is decided for a similar solution but based on a linear actuator that moves both the left and right surfaces.

A PID controller has been designed and adopted in order to comply with the requirements given by the aims of the project:

- A maximum frequency band of at least 15 Hz.

- Introduce typical saturation of real size aircraft.

Sensors The main sensors used are MEMS accelerometers, chosen for their high accuracy at low frequencies, but mainly because they require a normal data acquisition system. This does not force the use of an heavy and expensive systems such as the IEPE modules, that are usually used for piezoelectric accelerometers.

On-board pc This kind of setting admits the great advantage of a small computer (4 cores ATOM) incorporated in the model with the ability to deal with the needs of the acquisition of the data and process them for active control. The pc generates, according to the control law, electric signals that once reached the motor, are used to control the surfaces. The computer is equipped with the system developed within the Politecnico di Milano Real Time Application Interface (RTAI), developed in Linux.

(a) Linear actuator. (b) Harmonic actuator.
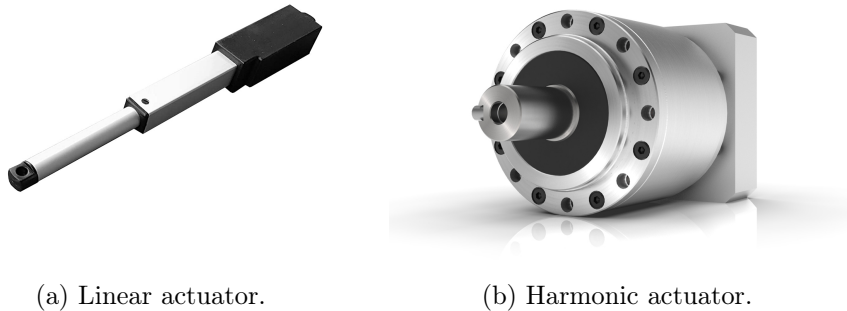
Figure 2.10: Actuation devices.

Figure 2.11: Box containing the drive control system (left), built-in computer with data acquisition system (right).
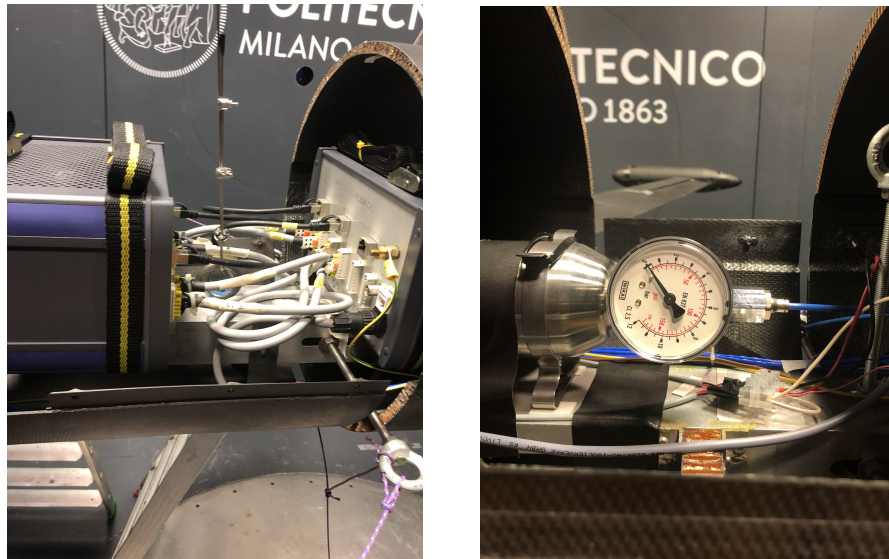
Figure 2.12: Instrumentation on board.

RTAI is an open source code, Linux patch, realized to accommodate all necessities inherent to AC activities and real-time simulation such as acquisition, identification and control implementing. It consists in a real-time interface tool between experimental hardware and software block scheme. In fact, it allows to modify parameters, monitor every type of signal processed by the on board pc and analyse them.

The embedded computers as well all the necessary acquisition cards are based on the PC-104 form factor allowing for a final small size and weight embedded system

In fig.2.12 there is on the left the box with the control of the drives for the control surfaces, connected with the RTAI system for the acquisition and processing of data in real time, while on the right the cylinder with the measurement of the pressure inside highlighted. The cylinder is used to operate the anti-flutter safety device in an emergency.

Anti-flutter device   The anti-flutter is connected to accelerometers which, when it reads an acceleration value above a limit set by the control room (4g), sends the activation signal to the cylinder. The cylinder, as long as it is under pressure, manages to keep the aircraft safe in conditions of high instability. The pneumatic system has two targets: to move the mass rapidly from backward to forward position and to keep the mass in safety condition without any compliance. This tank has the capacity of three shots, after which it must be refilled since it is no longer able to keep the model in safety.

During the tests the cylinder loses pressure due to excessive operations, it is necessary to interrupt the tests and reload it. This modality, however effective in terms of model safety, involves wasting time during tests.

2.2 Stick model

The need to have a numerical model that faithfully reproduces the features of interest can be traced back to the possibility of simulating the response of the model and predicting the results of the analyses.
So an aeroelastic FEM is built, with structural and aerodynamic properties that are as close to reality as possible.

2.2.1 Hypotheses and simplifications

Some hypotheses are introduced in the construction of the model in order to simplify the subsequent analyses without excessively damaging the final results. Otherwise it would be necessary to review the hypotheses getting closer and closer to a detailed model.

Beam modeling A first modeling of the aircraft is conceived using beam elements. This choice is linked to the simplicity of analysis and reading of the results, as well as to the less expensive numerical calculation. The beam elements allow to easily understand the global behavior of the structure, but not the local one.

Usually the model is built under these assumptions and its correctness is verified later. It is common practice to start from a more simplified model and then advance in detail if the results are not satisfactory.
In the case in question, the hypothesis of the beam can be justified by the fact that the aerodynamic sectors installed on the spar do not introduce further stiffness in the structure, which therefore can be assimilated to that of the spar itself.

Always following the intent to grasp the general behavior of the structure and not the local one, it is decided to simplify the structure modeling in some connection sections, such as the wing-fuselage and wing-pod attachment. Therefore rigid elements RBE2 are used as junction between the two end sections.

Concentrated parameters Some parameters are modeled as simple lumped elements. This is the case of the aerodynamic covers, reproduced in MSC/-

NASTRAN by CONM2 elements, or the case of the ailerons, represented through a single concentrated mass.

On the other hand, the opposite is true for the cables, for power supply and data transmission of the engine, for on-board PC and accelerometers. These masses are inserted in the model as masses distributed for unit length of the individual structural elements.

Aerodynamic modeling In MSC/NASTRAN, to recreate the aerodynamic behavior of a lifting surface, the *Doublet Lattice Method (DLM)* is implemented. This method is based on a linearized theory in aerodynamic potential and consists of an extension of the stationary method *Vortex Lattice* to unsteady flows.

The wing is seen as a lifting surface without thickness and divided into panels aligned with the direction of the asymptotic flow. On each panel there is a distribution of doublets of unknown oscillating intensity (vortex if stationary flow) arranged on the line at the 1/4 of the chord. The speed induced on a single panel is the sum of the contribution of all the panels.

2.2.2 Structure

The aircraft FEM model is built by discretizing all the components with beam elements. So it is done for wings, fuselage and tail planes. Rigid elements of the RBE2 type are used for control surfaces-structure and wing-fuselage connections.

In writing the MSC/NASTRAN code, the CBEAM cards are used, with relative PBEAM properties, and CBAR (PBAR properties). The CBAR cards are used exclusively for the construction of the wing-fuselage junction and for the wing-end pod attachment screws. No particular geometric and structural properties are required from the aforementioned components.

A stick model bases its validity on the exact reproduction of the inertial and stiffness properties, therefore it is necessary to assign the appropriate properties of the real model to the respective sections of the beams.

Beam elements are placed in correspondence with the elastic axis of the spar to have the same structural behavior.

The values of the moments of inertia and area of the section at each node are then included in the PBEAM card. These values are the result of experimental measurements or extracted from the aircraft's CAD model.

In these cards there is also the possibility of including a mass value per unit of length, which is added to the mass participating in the structural response, computed as density per volume. This field is useful to include in the model data cables for accelerometers and power cables for integrated PCs.
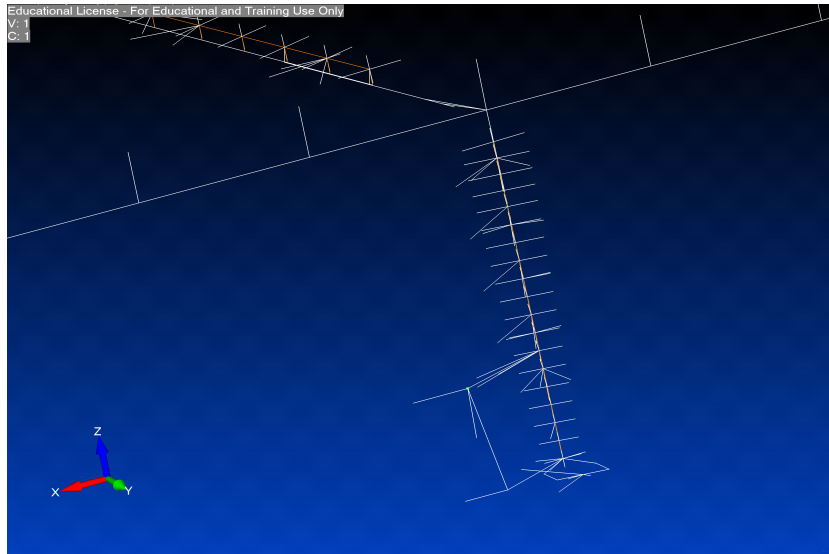
Figure 2.13: Wing detail

Finally, it is also necessary to model the suspension system of the X-DIA to maintain the fidelity of the results. The system includes the use of rigid cables for vertical support and elastic cables for horizontal connections. The ropes are stretched appropriately to leave the model completely free to move and respond with rigid body frequencies that depend on their tension. This results in MSC/NASTRAN through the use of CROD elements to simulate cables and CELAS springs to simulate assembly compliance.
In fig.2.14 note the free-free constraint with the cables that support the model on one side and bonded in all the Degree of Freedom (DoF) on the other.

2.2.3 Aerodynamics

The phenomenon under analysis takes into account dynamic interaction between aerodynamics and structure, so a aerodynamic description of the aircraft has to be provided.

Aerodynamic mesh In MSC/NASTRAN, in order to model aerodynamics, it is necessary to differentiate if it is a matter of lifting bodies (wing or tail planes) or of interference one (fuselage). CAERO1 and CAERO2 are used respectively. The system in question is modeled with lifting surfaces only, with the exception of the pod which will be treated later in section 2.2.5.
The wing surface, or the surface covered by the aerodynamic sectors, is
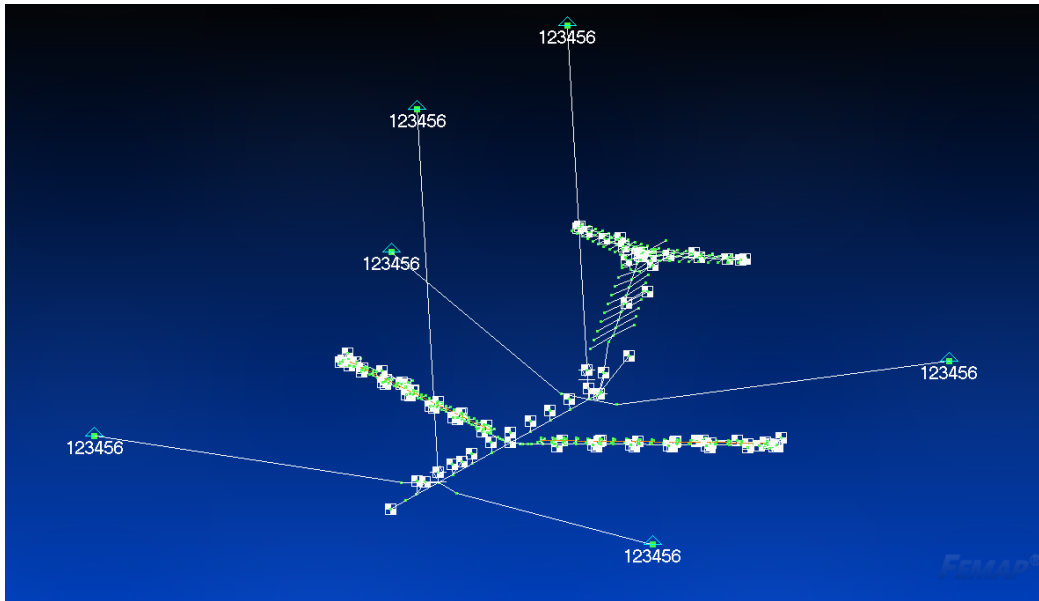
Figure 2.14: Beam MSC/NASTRAN model, stick model.

discretized into panels as indicated by the DLM method. The denser is the mesh, the more reliable the value of the aerodynamic coefficients. However, a high number of panels can unnecessarily burden the numerical calculation. To this purpose, a convergence analysis is performed to optimize the number of panels required.

Another factor to consider is of a numerical and modeling type: the aerodynamics resulting from the DLM is more effective than that experienced in the tunnel. This leads to a less nourished discretization to mitigate the extra effect that occurs in numerical reconstrunction.

The final result corresponds to 24 panels distributed spanwise and 10 chordwise. The final result in terms of discretization of the panels takes into account convergence analysis carried out on aerodynamics and coefficients. Fig.2.15 shows how the CAERO1 extend and cross the fuselage. This is essential to reproduce the correct lift distribution, which otherwise would go to zero in correspondence with the wing-fuselage attachment. Another precaution necessary during the construction of the aerodynamic mesh is to make sure that the borders of the panels are as much aligned as possible, with particular attention to the spanwise alignment, as numerical problems could be generated. In fact, as explained in section 2.2.1, the DLM uses a horseshoe vortex distribution with semi-vortex aligned with the velocity of the flow must not fall near a control point. The control points are the points in which the constraint conditions of the aerodynamics are imposed,
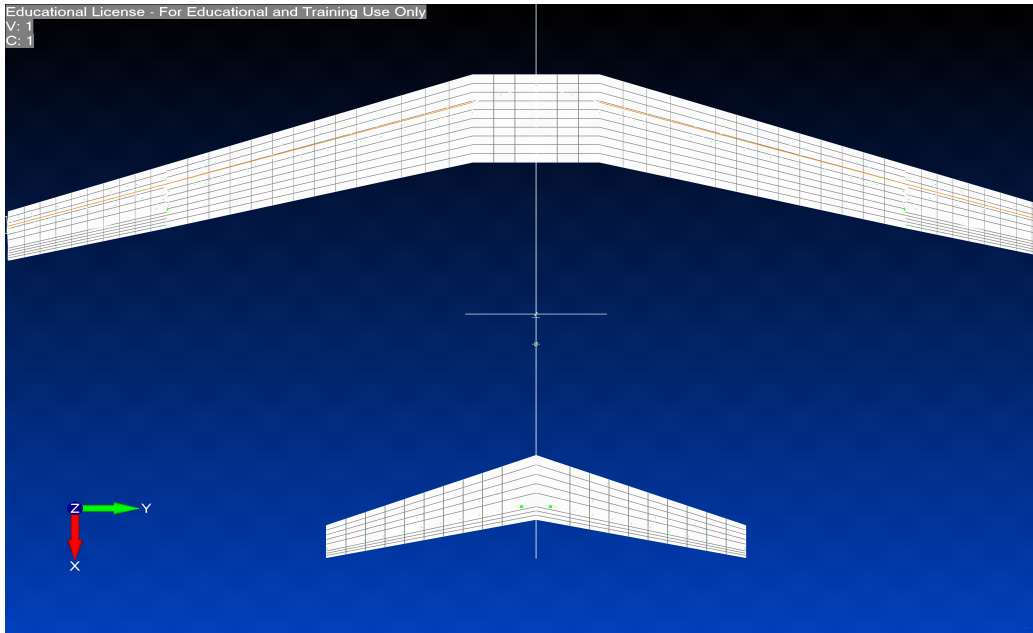
Figure 2.15: Aerodynamic discretization of the wing and tail planes.

for which it is possible to find the unknown factors of vortices and doublets. These points are placed at 3/4 of the chord of the single aerodynamic panel.

Splines The aerodynamic modeling of the lifting surfaces then requires a further conclusive step, i.e. the transport of the aerodynamic forces developed from the aerodynamic to the structural mesh.
Convergence and modeling usually leads to different discretizations for structural and aerodynamic calculation. The resolution of an aeroelastic problem however requires that they interface and that the effect of one affects the other and vice versa. The goal is to obtain the load at the nodes of the structural model starting from the aerodynamic load.
To do this it is used an interpolation scheme that, known the displacements in a discrete number of points $w_i = w(x_i, y_i)$, construct a continuous function of displacements $w(x, y)$. This operation will allow to define a set of displacements in the aerodynamic model starting from the structural set.
In MSC/NASTRAN this translates into the use of SPLINE1 and SPLINE2 cards, according to the type of structural model the user want to implement, respectively plate or beam type. They allow to connect the structural nodes of a component with the CAERO referred to it.
The numerical model is made with only linear splines, except for the vertical plane which instead contains superficial splines.

(a) Aerodynamic-structure interface modeling.

(b) Detail of the structural nodes and of the CAERO.
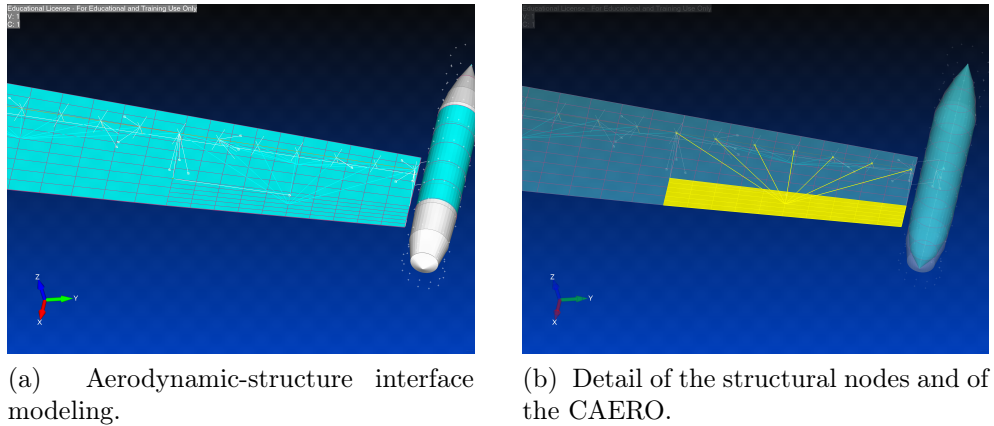
Figure 2.16: Interpolation performed in Femap.

2.2.4 Control surfaces

The control surface in the model are ailerons, rudder and elevators.

Structure   To represent them in MSC/NASTRAN a rigid connection RBE2 is used. This is a preliminary choice and in the future can be reviewed more in detail. This choice implies that the mass has to be modeled as lumped element, with a CONM2 element located in the center of mass of the control surface.

Regarding the kinematics and so the representation of the DoF associated (i.e. rotation along its hinge axis), the method provide the introduction of a *scalar point* (SPOINT card) as rotational DoF.
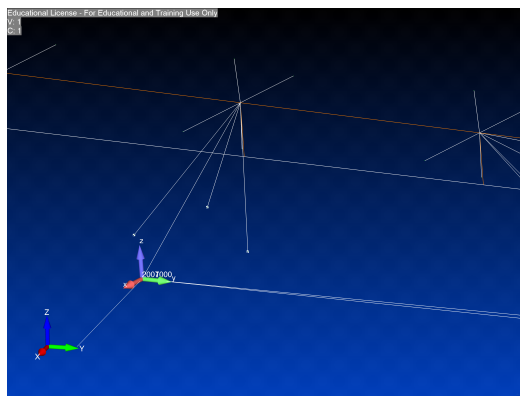
Figure 2.17: Detail of the aileron.

At the ends of the hinge axis, on each side two coincident node are created. One connected to the wing structure and the other to the opposite section of the aileron. So the scalar point can be now defined as the relative rotation between two coincident nodes, using MPC card.

SPOINT node requires being defined in properly oriented reference frame, having one of the axis directed along the hinge axis. The scalar point will be defined as relative rotation along hinge axis direction (fig.2.17), con-

ventionally y axis of the reference frame.

However there is the demand of constrain the coincident nodes along other directions, avoiding any kind of lability of the model. This can be done reproducing exactly the link mechanism of the real model. The modeling technique commonly used consists in constrain all the translations of a section and on the other side only two of them, leaving that node free of moving long the direction corresponding to the hinge axis of the surface. This means to simulate, respectively, an hinge and a sleeve.

Constraint	Direction
Hinge	T_x, T_y, T_z
Sleeve	T_x, T_z

Table 2.1: Constraint of control surfaces, refer to fig.2.17 for directions (x, y, z). T stands for translation.

It is worth to underline that constraints on translations and rotations between nodes are defined in the local reference frame of the surface, with the purpose of not introducing components of the reaction forces that do not exist, due to misalignments.

This modeling technique allows to convey the aerodynamic forces correctly on the wing structure. In fact, it would not be fair to spread the loads directly on the wing surface, because in reality the loads are transferred from the aileron to the structure by means of fastening mechanisms (i.e sleeve and hinge).

Aerodynamics The aerodynamic modeling of the control surface follows the same praxis used for the wing one, with a discretization of 10 boxes spanwise (in order to maintain the CAEROs alignment) and 6 chordwise.

MSC/NASTRAN requires also to state what aerodynamic boxes belong to the control surface in order to specify them in the aeroelastic problem setting. So the boxes of control surfaces are inserted in the AELIST passed later to AESURF card.

2.2.5 Pod

In preparation of the final flutter suppression test, in order to limit the risk of braking the model in case of a non-properly working of the flutter suppression system this safety device is designed, whose functioning is explained in [4].
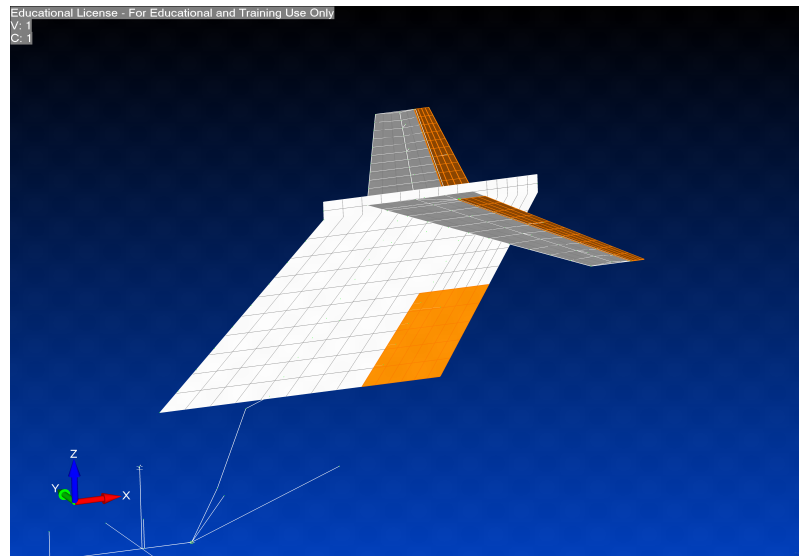
Figure 2.18: Detail of tail control surfaces.

This is very crucial point, since the introduction of this component changes in a significant way the dynamics of the aircraft, due to its distance from the axis of the aircraft, its connections compliance and its geometry.
An appropriated modeling is required to catch correctly the behavior of the structure.

Structure   As one can appreciate in fig.2.8 the anti-flutter device consists in a mass on a slider, covered by a cylinder for aerodynamic shape. A simple representation is adopted for it, with 4 lumped masses reproducing the components of the device.
The sliding motion of the mass is modeled with 2 nodes in correspondence with the 2 possible configuration of the anti-flutter mass. The corresponding CONM2 is located in one of these 2 nodes according to the type of analysis (anti-flutter on or anti-flutter off).
The connection between the tip section of the spar and the pod is a source of compliance due to its position and type of link. So there is the need to use an elastic element to represent it. Massless bars with circular section are introduced in order to catch the suitable stiffness of the attachment mechanism. The radius of the bars is the parameter with which one can play to change the stiffness value of the connection: the real screws have a threaded radius of 1.5 mm, in the numerical model instead they are built with a radius of 2 mm with the aim of improving the correlation between FEM and experimental model. All the lumped masses referring to the component are
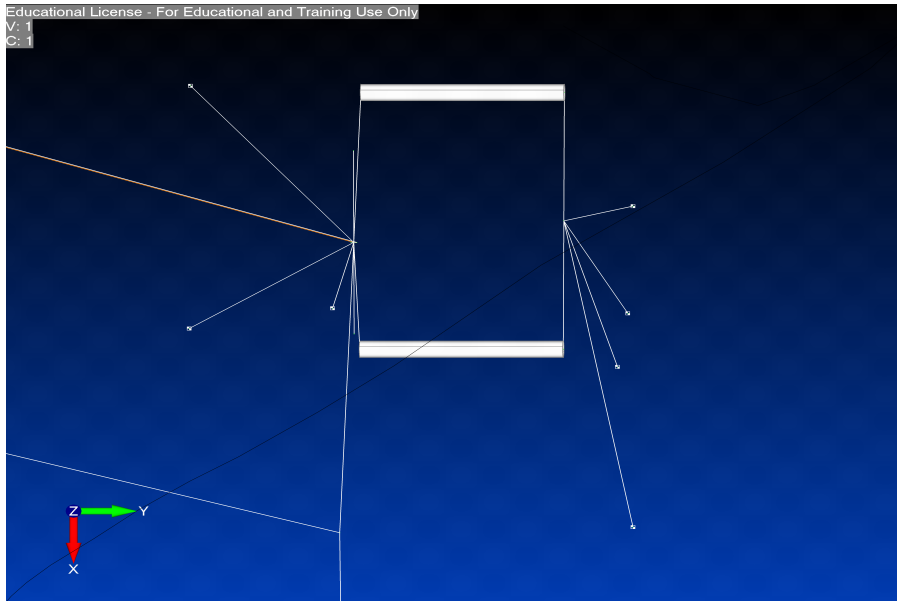
Figure 2.19: Anti-flutter in Femap. Here the device is off.

rigidly connected to the bars end points (fig.2.19).

Aerodynamics The pod is not a lifting surface, but its aerodynamics contribution is absolutely not negligible, as the experimental campaign showed. The presence of this device generates a different fluid motion such that a lift contribution raises, since there is a local variation of angle of attack. This additional part is limited but it has to be taken into account, the solid body modeling is carried out with a distribution of sources and sinks according to the *Slender Body Theory*.

The problem occurs when the interaction between wing and pod has to be considered. An *Interference body* should be introduced. It provides the interaction laws establishing impenetrability condition on the surfaces. The Interference Body Theory allows to take into account the simultaneous presence of lifting surfaces and other bodies. From the aerodynamic potential theory, MSC/NASTRAN implements the method of images: proper singularities (vortexes and doublets), mirrored quantities of DLM ones, located inside cylindrical bodies to match each singularity external to the body with an internal one at the image point. The image singularity exists to negate the flow through the body surface generated by the external singularity. These theories are enclosed and implemented in MSC/NASTRAN with the use of PAERO2/CAERO2 cards. They allows to create both slender and interference bodies.

(a) Slender body.   (b) Interference body (white dots).
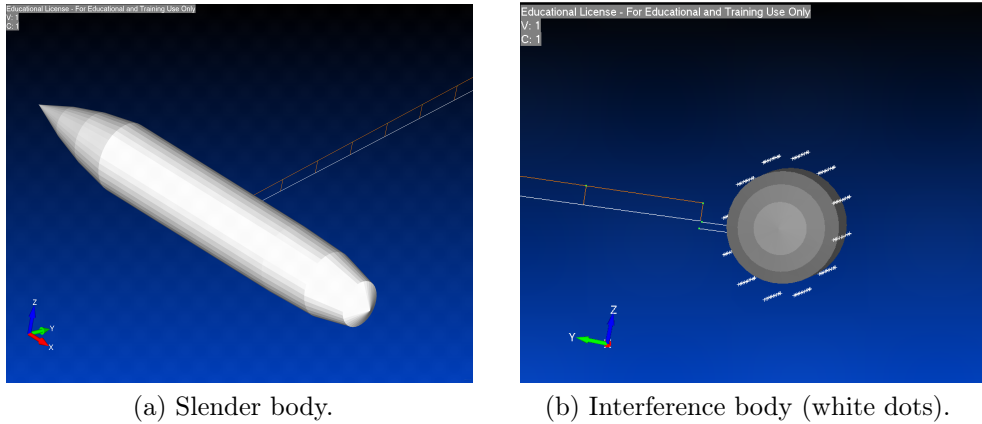
Figure 2.20: Modeling of the pod aerodynamics in FEMAP.

The slender one requires as input the radius of every sections which compose it, since the only possibility of modeling is with a circular section. The complexity of modeling closed bodies can be avoided representing them by a cruciform lifting surfaces. It can be that the model is not always coherent with the reality but what matters is that it reproduces global effects and it is respectful of constraints of the methodology applied.

The limitation on the shape of interference bodies is even more restrictive than the slender case. In fact MSC/NASTRAN allows only to build it with constant circular section. The only degrees of freedom are the radius of the section and the disposition of control points, along the circumference, where to impose boundary conditions.

Splines   As in the control surfaces case, a beam spline is used for the pod, giving as structural points the nodes belonging to the mass and to the guide.

2.3 Modal analysis

In order to get an acceptable correlation between the experimental model and the analytical one, it is necessary to perform a modal analysis to verify if the dynamic behavior of the structure is well caught.
The analysis results will be compared with the Ground Vibration Test (GVT) data on the real model. The attention is fixed on the lower frequency modes because they are the most significant for the dynamic behavior of the structure, especially for flutter phenomenon.
It is possible to carry out a modal analysis in MSC/NASTRAN by means of

SOL 103 solution type and EIGRL card. The extracted modes are only 25, with particular attention on the first 3 deformable modes since these are the ones involved in the flutter process.

2.3.1 Preliminary checks

The preliminary aspects to examine are the mass and inertia checks. Every component of the X-DIA model is weighed, computed the position of its center of mass and its moments of inertia. So at the end of the modeling phase the FEM model must have the same mass properties of the real model, keeping attention both on the local and global ones. Same outline to reproduce the moments of inertia.

Thanks to the CAD model of the real aircraft it is possible to find the moments of inertia of every modeled component and insert them in FEM model through CONM2 or PBEAM elements. Ensuring the respect of the inertia of all components it is easy to match also the global aircfraft values.

One important aspect to monitor is the aircraft symmetry. The structure is symmetric along y axis, so the mixed moments involving that axis have to be null, $I_{xy} = I_{zy} = 0$.

2.3.2 Frequencies

The results in terms of frequencies are listed below in tab.2.2.

Mode	Freq [Hz]	Mode	Freq [Hz]
1	0.307	11	9.228
2	1.209	12	11.81
3	2.497	13	12.25
4	3.348	14	14.43
5	5.196	15	14.50
6	7.334	16	18.79
7	7.472	17	20.11
8	8.079	18	21.10
9	8.793	19	23.06
10	8.938	20	24.14

Table 2.2: Frequencies with mass in backward position.

Mode	Freq [Hz]	Mode	Freq [Hz]
1	0.307	11	9.240
2	1.209	12	11.85
3	2.500	13	12.28
4	3.347	14	14.44
5	5.225	15	14.68
6	7.107	16	18.80
7	7.136	17	20.45
8	7.863	18	21.21
9	8.793	19	23.37
10	8.921	20	24.13

Table 2.3: Frequencies with mass in forward position.

The first 4 values of frequencies are relative to the rigid modes, result of free-free connection with cables.

The 5th mode is the first bending, the 6th and 7th are the torsional ones, respectively anti-symmetric and symmetric. These modes are the most involved in the flutter dynamics.

2.3.3   Mode Shapes

For the flutter point of view, the most important features are the mode shapes. Indeed it is necessary to reproduce accurately the pattern of the vibrations to well capture the flutter mechanism.
The scaling process chosen for the analysis is the unitary mass.

The outcomes of this analysis will be presented later in sec. 3.2 by way of a comparison with real model results.

2.4   Flutter analysis

According to the purpose of this work, the flutter analysis is the most relevant topic. The aim of the numerical model is to predict the flutter point, in terms of velocity, and its mechanism, typical bending-torsion coupling.

The numerical analyses, conducted with MSC/NASTRAN (SOL 145, that implements the $p-k$ method) at several velocities, are summarized in V-g (velocity versus aeroelastic damping g) and V-f (velocity versus modes frequencies f) plots.
As expected, with the backward configuration (fig.2.21), the bending-torsional coupling appears, at a speed of about 45.5 m/s. Fig.2.21a shows how the damping of the symmetric torsion mode becomes positive, so the aerodynamics start to provide energy to the structural vibrations. The interaction between 2 modes can be observed in V-f plot (fig.2.21b) where the 5th and 7th, with the increasing velocities, tends to vibrate at the same frequency.

Instead with the safety system switched on the behavior changes.
The damping associated to the symmetric torsional mode in this configuration remains negative, indication of the fact that vibrations do not diverge. However this result suggest to proceed with caution since it is recommended to guarantee always a minimum level of damping to avoid explosions due to errors or undesired conditions. The requested value of aeroelastic damping ratio for flutter is 3%.
In the case presented the bending mode has an outset of flutter, restoring in shortly time the stability (as it is possible to infer from fig.2.22a and 2.22b).
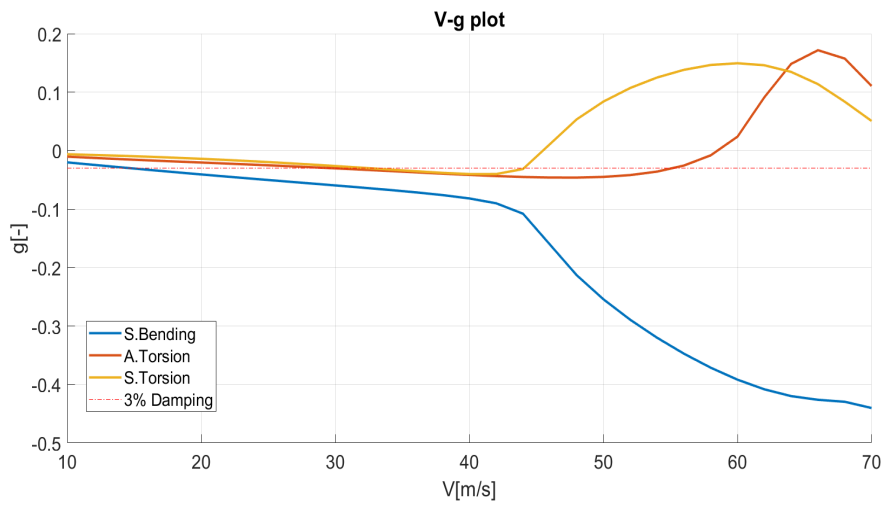
(a) Damping variation.
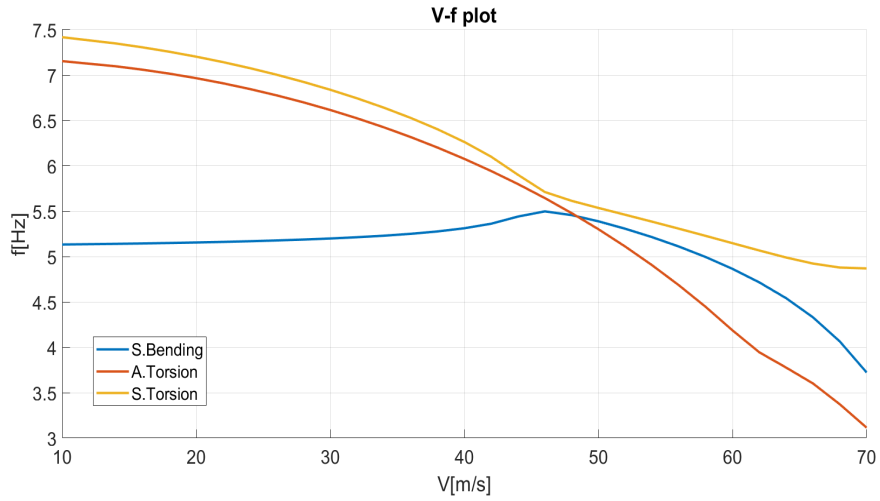
(b) Frequency variation.

Figure 2.21: Flutter analysis results with mass in backward position.
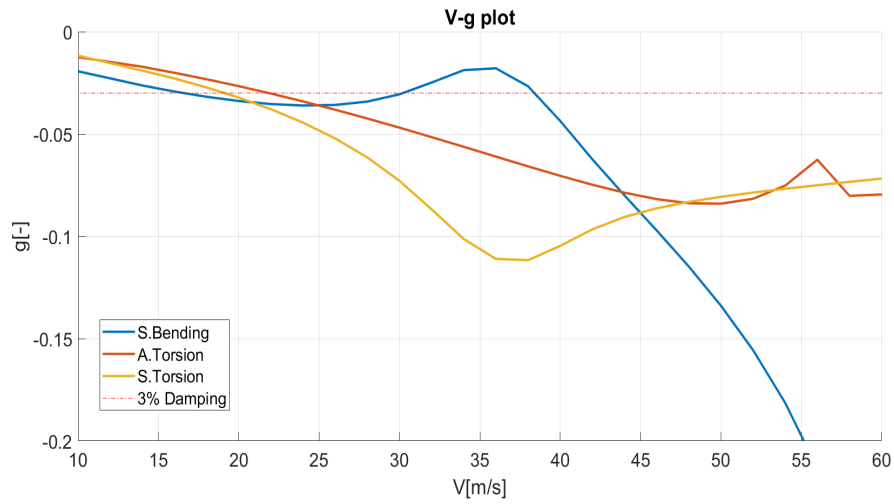
(a) Damping variation.
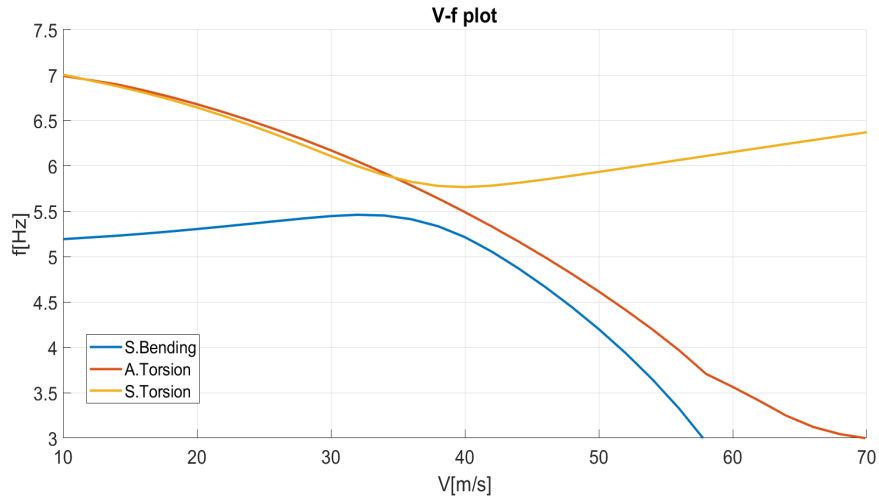
(b) Frequency variation.

Figure 2.22: Flutter analysis results with mass in forward position.

Chapter 3

Preliminary Experimental Activity

The chapter takes over the short explanation of the tests performed in the wind tunnel test session of July 2019. These are not the only wind tunnel tests carried out on the X-DIA model but the initial ones in order to identify the flutter point on the model and draw the graphs V-g and V-f of the aircraft, without any type of control action.

An other session of wind tunnel tests took place later in the last week of January 2020 and are fully described in chapter 6. These have a brief analysis and comparison in open and closed loop, they also present various robustness analyses with tests to vary the gain and phase lag on the controllers.

Previously to the wind tunnel tests of July 2019, a GVT was needed to extract the natural frequencies and the damping at zero speed, in order to have a fully descriptive database of experimental data, useful to compare them with the stick model results presented in the chapter 2. This first GVT session was conducted in the DAER laboratory. Subsequently, after the first tests carried out in the wind tunnel in July 2019, the need to increase the precision of the GVT data emerged with the aim to improve the correlation of the MSC/NASTRAN stick model. Therefore, with a new experimental modal campaign, mounting the X-DIA aircraft in the same final configuration used during wind tunnel session hung with the later mentioned free-free constraint.

For description purposes, only the results of the second and more specific GVT are illustrated. This GVT is later than the wind tunnel tests presented in the following chapter, but is presented earlier as the final data coming from it will be used throughout the correlation phase.

The fig.3.1 shows GVTs settings.

(a) Laboratory GVT.

(b) Wind tunnel configuration GVT.

(c) GVT chamber.

Figure 3.1: GVT configurations.

In fig.3.2 the aircraft in the wind tunnel before the tests bound with a free-free constraint.

The second part of the chapter briefly presents the results of flutter analysis and wind tunnel identification, the type of excitation used and a comparison with the results of the stick model already in possession.

(a)   (b)
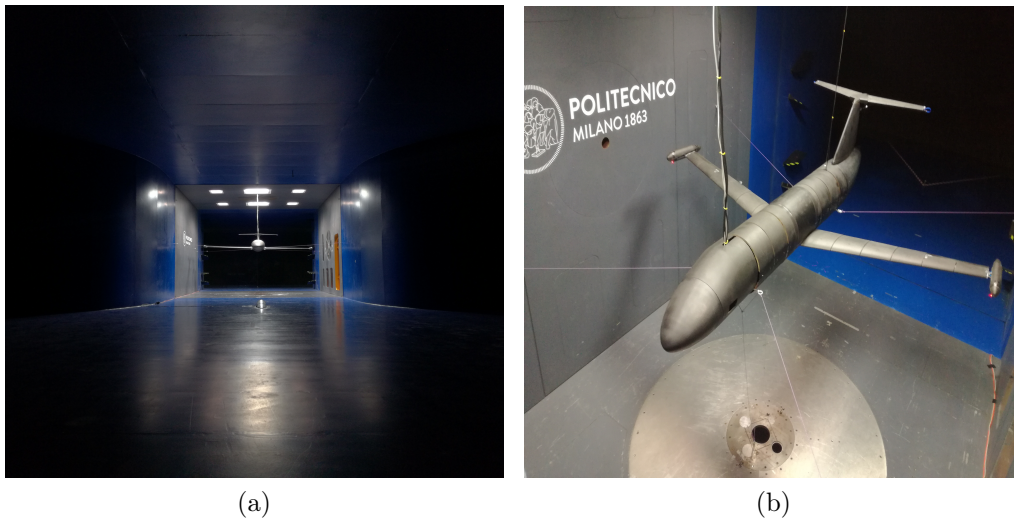
Figure 3.2: Model in wind tunnel before tests.

3.1   Experimental model

The features of the experimental model and its main components have already been expressed previously, in sec.2.1.

The final objective of this part is to arrive at a comparison between the stick numerical analysis, that leads to a V-g and V-f graph, and the experimental ones that will bring to necessarily different results but which must be comparable with the previous ones.
The comparison will allow to understand if the numerical stick model need an updating or if it requires a detailed modeling in some of its parts.

Tests to measure natural frequencies, damping and mode shapes are shown in this section and define the modal analysis of the experimental model.
Once the quality of the modal analysis measurements are established, the work on the flutter analyzes begins, bringing the model to its limit to create the V-g (damping as a function of speed) and V-f (natural frequencies as a function of speed) graphs.

Finally, the results of the correlation of the two models are presented and the outcome of this phase of the tests will be commented.

3.1.1 Modal test

In order to be able to carry out a comparison between the numerical and experimental model, it is necessary to have an instrument that is able to extract the frequencies and modal shapes of the model in the wind tunnel in a simple and effective way and then allow them to be compared with the numerical values.
This tool is the Ground Vibration Test (GVT).

TEST PHASE

The experimental modal analysis performed on X-DIA wind tunnel model is fully described in [20]. During GVT the model is free-free suspended by means of ropes. The component configurations analysed are two, depending on the anti-flutter safety device:

1. complete aircraft with mass of both anti-flutter devices fully forward.

2. complete aircraft with mass of both anti-flutter devices fully set back.

Two types of tests are carried out for each configuration:

1. GVT on all lifting surfaces: wings, horizontal and vertical tail plane. An instrumented hammer is used to excite the structure (*roving method*), with light sensors capable of measuring only the out of plane components.

2. GVT only on the left wing. In this case the impact method with fixed accelerometers (impact always through an instrumented hammer) is employed, with mass sensors not negligible but able to measure also the in-plane components of the structure and therefore permitting to study modal shapes in all their components (also in-plane).

For these analyses, Maxwell's theorem is used, which states that the response at a point P due to the entry at a point Q is equal to the one at the point Q due to the same entry at the point P. This assumption involves the symmetry of the mass, damping, stiffness and FrF matrices. A fundamental assumption for the use of the theorem is that the structure has linear behavior, this is verified for example by observing the symmetry in the FrF.

Constraint configuration All experimental tests are carried out on the aircraft in the same suspension conditions used during the future flutter tests in the wind tunnel.

In order to avoid discrepancies in the dynamic behaviour due to characteristics of the suspension system, the model is tested in the wind tunnel test chamber just before the aeroelastic tests.

Thanks to the GVTs it is possible to extract FrFs and to recover the first frequencies connected to the first four rigid modes. The rigid modes are strictly related to the suspension system and then with the ropes configuration chosen. These should be characterized by very low frequencies in order to not interact with deformable modes of the structures.

In table 3.1 are presented frequencies, damping and descriptions of rigid modes due to suspension system. The description is not so clear for each mode because sensors acquire in only z direction, making shapes not always intelligible.

Mode	Frequency (Hz)	$\zeta(\%)$	Description
1	0.50	0.27	—
2	2.58	0.23	Rotation around yaw axis
3	3.24	0.70	Front/back movement
4	4.94	0.82	—

Table 3.1: Identified rigid modes frequencies and damping.

Sensors set up for roving impact test Wireframe of the airplane is chosen in order to recover the first out of plane bending and torsional modes of the lifting surfaces: wings, horizontal tail, vertical tail.

Reference systems are defined as follows:

- x axis parallel to the length of the fuselage pointing towards the tail;

- y axis orthogonal to the symmetry vertical plane of the aircraft and pointing towards the tip of the right wing;

- z axis normal to the previous two axes, pointing from the floor to the ceiling;

- origin coincident with intersection point of the wings with the fuselage.

Component	X (m)	Y (m)	Z (m)	XY (°)	XZ (°)	YZ (°)
Fuselage	0.0000	0.0000	0.0000	0.0000	0.0000	0.0000
Left wing	0.0650	-0.2900	0.0000	-72.0000	0.0000	0.0000
Right wing	0.0650	0.2900	0.0000	72.0000	0.0000	0.0000
Vertical tail	0.9200	0.0000	0.3100	0.0000	0.0000	0.0000
Horizontal tail	1.3600	0.0000	0.7050	0.0000	0.0000	0.0000
Left pod	0.0650	-0.2900	0.0000	-72.0000	0.0000	0.0000
Right pod	0.0650	0.2900	0.0000	72.0000	0.0000	0.0000

Table 3.2: Definition of the coordinate system of components.

Component sub-coordinate systems are defined too in order to simplify the description of the geometry in the acquisition system software. Seven components are defined and the orientation of their coordinate systems are reported in table 3.2.
The acquisition directions in each point depends on the component in which it is defined. In this test phase all directions are in z axis of local coordinate system of each points, except those of the vertical tail that are set in y directions.

The whole set of acquired FrFs is made of 46 signals, composed of points on vertical and horizontal tail, wings and pods reference systems. All the fuselage points, from 1 to 7, are not acquired and they are left in the wireframe only as visual reference.

Local coordinate system and each point with its location are represented in fig.3.3.
The FrFs needed for the modal identification are acquired using an impact roving technique, changing step by step the excitation point and keeping fixed some accelerometers in strategic points. This technique takes to good results only if the reciprocity theorem hypothesis are satisfied.
The advantage of this method is the simplicity and rapidity of the measurements, but mostly the small number of accelerometers needed to put it into practice. The number of accelerometers is a key point for the experiment, a large number impacts in a not negligible way on test results, changing the mass distribution on the wings and consequently frequencies and shapes.
Five accelerometers are used as references in order to have good signals:

1. Tip of left wing, on the spar that brings the aileron, to acquire out of plane flexural and torsional modes of the wing. Local direction +z.

2. Tip of right wing for symmetry. Local direction +z.
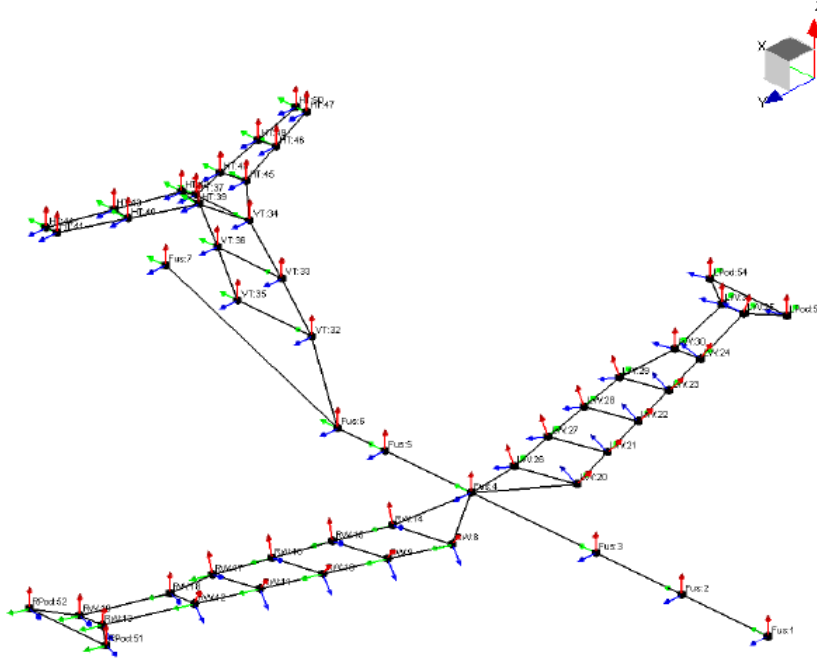
Figure 3.3: GVTs experimental wireframe.

3. Tip of the left horizontal tail, on the end rib, to acquire out of plane flexural and torsional modes of the horizontal tail. Local direction +z.

4. Tip of the right horizontal tail for symmetry. Local direction +z.

5. Nose of the fuselage. Local direction +z.

IDENTIFICATION

GVTs acquisition parameters   The test performed is so a MIMO impact test. As already explained 5 accelerometers are used as references while 46 locations are excited.

FrFs are acquired with a sampling frequency of 512 Hz and with a frequency resolution of 0.0625 Hz. Anti aliasing filters cut frequency is set at 80% of Nyquist frequency, about 200 Hz. The observation time of 16s is employed to give to the structure the time to decay autonomously. Each point is hammered five times in order to reduce measuring noise thanks to the averages.

Coherence analyses of acquired signals showed values very close to one up to 200 Hz so the excitation method is considered suitable for test purposes. FrFs are estimated by H_v *method*, based upon the singular-value decomposition technique and suitable for modal analysis since it allows to eliminate the influence of uncorrelated noise both at the input and the output.[16]. It assumes that random noise and distortion are summing into both the input and output of the system.

For every excitation signal, the following functions are acquired:

- FrFs

- Autopowers

- Crosspower

- Coherence

All these tools are useful to provide solid results. Modal identification is carried out using the algorithm Polimax: the final modal base of each configuration is synthetized from the FrFs set, or multiple FrFs sets, that permit the best identification of the modes.

Configuration 1 (forwardMasses), test 1 (Roving Impact). The principal modes in the range 0-50 Hz for the X-DIA-FAA model in configuration 1, anti flutter mass in forwardposition, are numerically reported in table 3.3.

Configuration 2 (backward Masses), test 1 (Roving Impact) The principal modes in the range 0-50 Hz for the X-DIA-FAA model in configuration 2, anti flutter masses in backward position, are numerically reported in table 3.4.

VALIDATION

After the identification phase, validation/correlation is carried out. Once identified the model, a database which includes the measured natural frequencies, the measured dampings and vibrating modes is available.

At this point, known the measures, it is possible to decide whether to proceed with the activity or go back to the test phase and repeat some test: there is no single verification criterion. There are different verification criteria, which allow to substantiate the quality of the measurements and decide whether proceed in the activity or go bac. It is chosen to proceed mainly applying the Modal Assurance Criterion (MAC).

Mode	Damped freq [Hz]	Undamped freq [Hz]	Damping ($\zeta\%$)
1	5.20	5.20	0.13
2	7.14	7.14	1.22
3	7.78	7.78	1.08
4	8.26	8.26	1.03
5	9.00	9.01	1.65
6	10.43	10.43	0.48
7	12.55	12.55	1.00
8	13.45	13.45	2.65
9	14.98	14.99	1.60
10	16.36	16.36	0.83
11	19.69	19.69	0.54
12	24.12	24.12	0.65
13	26.03	26.03	1.29
14	30.02	30.02	1.84
15	32.02	32.02	2.04
16	45.03	45.04	1.80
17	48.92	48.93	1.24

Table 3.3: X-DIA modal parameters, configuration 1, test 1.

CROSS-MAC   It is a criterion to determine the degree of correlation between experimental and analytical modes. It can be calculated both on the reduced set of degrees of freedom measured (condensation of the numerical ones) and on the complete one of the numerical degrees of freedoms (expansion of measured ones). In this work the numerical set is always reduced to the experimental one.

$$CROSS - MAC\left(X_e, X_n\right) = \frac{|\{\Psi_e\}^T\{\Psi_n\}|}{\left(\{\Psi_e\}^T\{\Psi_e\}\right)\left(\{\Psi_n\}^T\{\Psi_n\}\right)} \quad (3.1)$$

$\{\Psi_e\}$ is the vector of modal shapes of the experimental set, $\{\Psi_n\}$ of the numerical one.

The AUTO-MAC criterion is completely identic to the CROSS-MAC one, but the difference stands in the eigenvectors set used for the calculation. In the AUTO-MAC case, the aim is to compare a mode set with itself. In particular this analysis is useful for the experimental mode set because it is an indication of how able is the experimental mesh to catch the actual structural behavior. An ideal AUTO-MAC should present a unitary diagonal and zero elsewhere, that means every mode is easily recognizable and can not be confused with any other one.

Mode	Damped freq [Hz]	Undamped freq [Hz]	Damping ($\zeta\%$)
1	5.20	5.20	0.17
2	7.43	7.43	1.14
3	7.88	7.89	0.75
4	8.28	8.28	1.30
5	9.10	9.11	3.07
6	10.38	10.38	0.39
7	12.49	12.49	0.90
8	13.46	13.47	2.73
9	14.74	14.74	1.23
10	16.28	16.28	0.85
11	19.20	19.20	0.57
12	23.35	23.35	0.65
13	25.94	25.94	1.16
14	29.82	29.83	2.86
15	32.21	32.21	1.67
16	44.72	44.72	1.83
17	49.05	49.05	0.82

Table 3.4: Identified modes of X-DIA-FAA model, configuration 2, test 1.

CROSS-MAC establishes whether two modal shapes coincide but not provides information on natural frequencies: it is not a correlation/validation on natural frequencies but exclusively on modal shapes; while the AUTO-MAC indicates whether the measured experimental modes are separate, not providing information useful for correlation but only for validation, the CROSS-MAC is advantageous for both.

Before using the CROSS-MAC it is necessary to make a geometric correlation: chosen a reference set (numerical or experimental), the modes calculated in an environment different from the reference one must be reported in the latter. The reference environment taken into consideration is the experimental one. The numerical environment is defined so as to reflect the features of the experimental one: in order to correlate modal shapes, they must be expressed in the same reference system, in tab.3.2.

Unlike the AUTO-MAC, which is a square matrix, the CROSS-MAC is usually a rectangular matrix: CROSS-MAC is rectangular as the numerically determined modes are much more than those found experimentally.

Since a priori it is not possible to know if experimental modes correspond to the numerical ones, generally it is exploited the first 'round' of the CROSS-MAC to understand what modes match: the result should be a rectangular

matrix, probably not diagonal, whose elements of interest are those with an high value (> 0.8), as these are likely to be the corresponding modes (i.e. the numerical mode which corresponds to that experimental one).

Configuration 1 (forwardMasses), test 1 (Roving Impact) Seventeen modes are identified in the range 0-50 Hz, thanks to the shapes it is been possible to have a description of features of each mode. Here, for the sake of simplicity and clarity, are reported the shapes of modes related to flutter instability. In the following figures are showed the first three deformable modes, two of these cause instability with mass in backward position.

Fig.4.11b and fig.4.11c show that the model is not perfectly symmetric since the two torsional modes, that in the numerical results are coincident and anti-symmetric and symmetric respectively, have some anomalies. It appears that, in both modes, one wing side has a bigger amount of energy with respect to the other and so one half-wing moves much more than the other.

If the structure were symmetric, the shapes of the two torsional would be completely symmetric or anti-symmetric and frequencies near to each other.

In order to validate these experimental results an AUTO-MAC matrix is calculated. The AUTO-MAC in fig.3.4a does not show pairings between the first 17 modes validating the test.

Validation of the test is completed thanks to other test goodness indices such as: Modal Phase Collinearity (MPC), Mean Phase Deviation(MPD), Mode Overcomplexity Value (MOV).

Configuration 2 (backward Masses), test 1 (Roving Impact) As for configuration 1, an AUTO-MAC matrix, to validate obtained experimental mode shapes, is shown in fig.3.4b
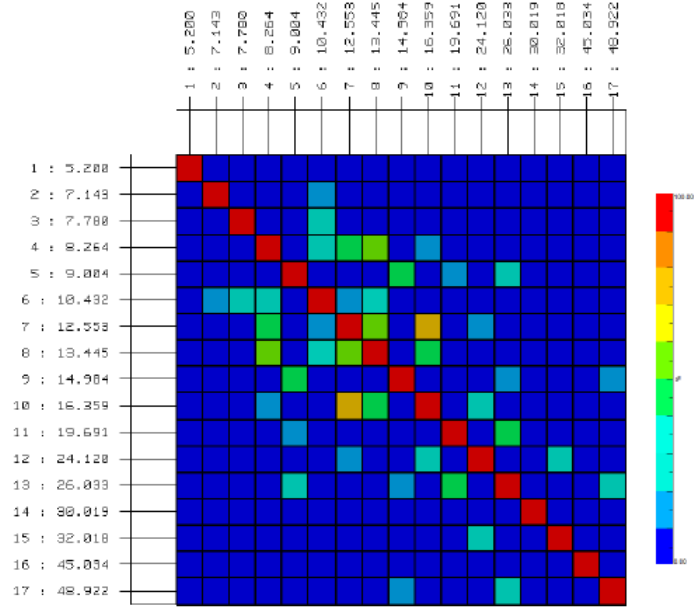
(a) Antiflutter device in configuration 1.
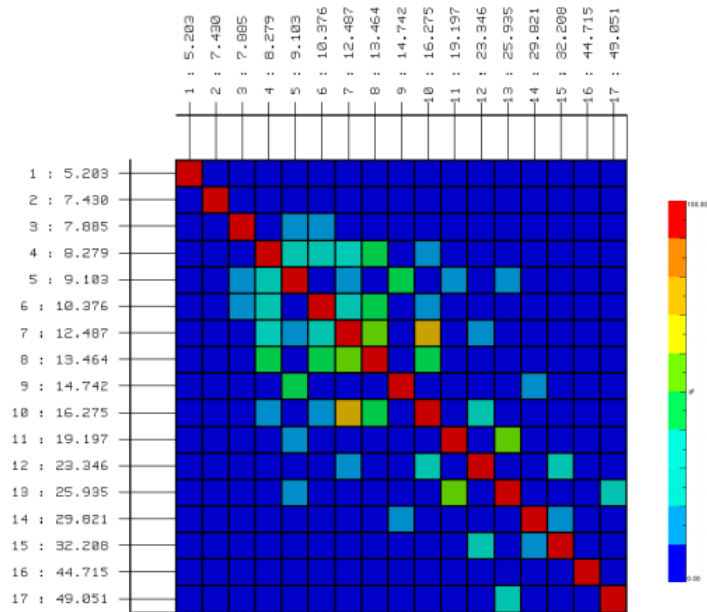
(b) Antiflutter device in configuration 2.

Figure 3.4: Experimental AUTO-MAC matrices of modes of X-DIA-FAA model.
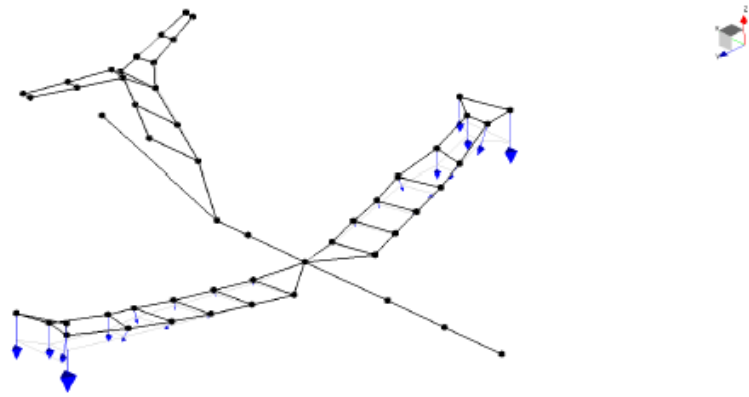
(a) Mode 1, 5.20 Hz.
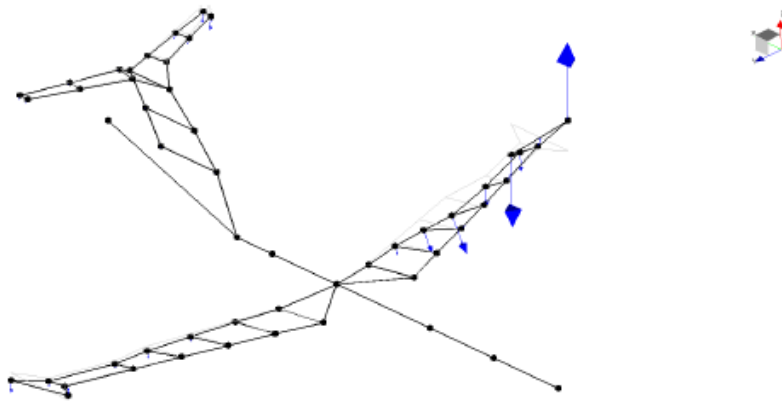
(b) Mode 2, 7.14 Hz.
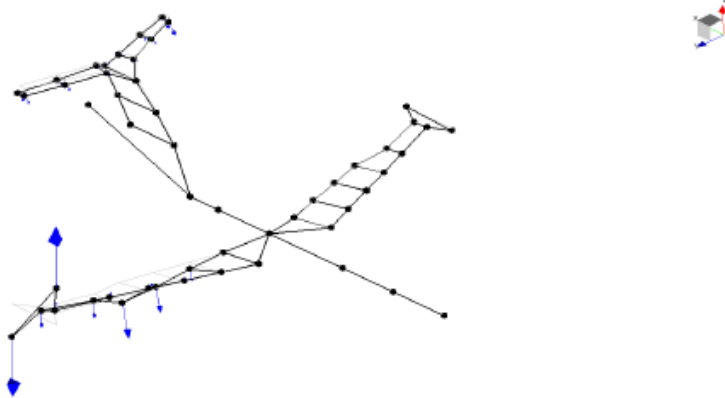
(c) Mode 3, 7.78 Hz.

Figure 3.5: Configuration 1: mode involved in flutter.

3.1.2 Flutter test

After the modal analysis through the tool of the GVT, which is the first tool to determine the characteristics of the structure and its dynamic behaviors, flutter analysis is introduced.

The study of the experimental flutter is necessary to have a comparison with the trend of the graphs V-g and V-f of the modes of interest, to find the exact position of the instability phenomenon and to be able to design a controller focused on details of the model in question.

In order to reconstruct the graphs of interest, wind tunnel tests are carried out at different flight velocities. The model is placed in the tunnel through a free-free constraint.

Data are recovered from sensors placed like in fig.3.6
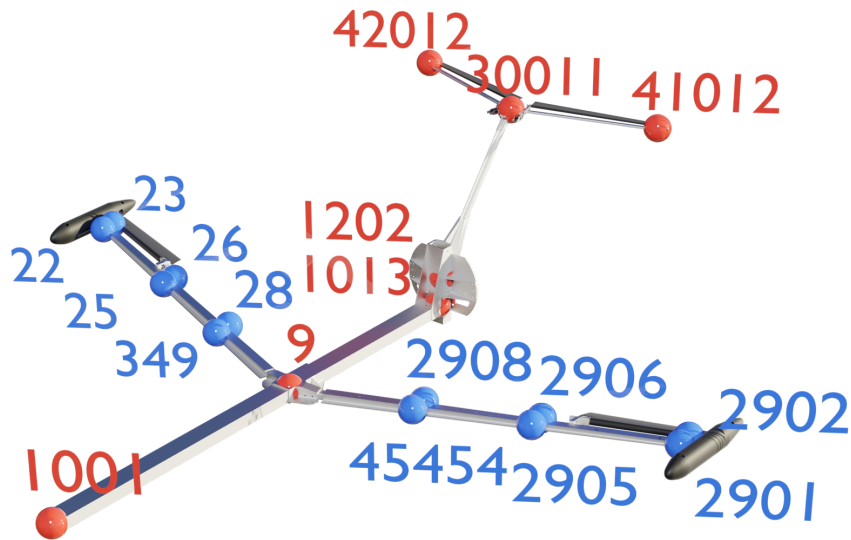
Figure 3.6: Accelerometer position

Numbers in fig.3.6 represents node ID in which accelerometers are placed in numerical model. The location in the numerical model reflects the location in the real model.

Tests are performed on the model in the two configurations under analysis: mass in forward and in backward position.

In tab.3.5 there are speeds at which data are acquired. Speeds starts from 0 to 40 m/s. At 0 m/s the result expected is the response of the structure forced with only inertia of the aileron motion. It's a result useful to the correlation phase and with GVT results. Reaching velocities greater than 40

m/s it is impossible at this stage, indeed without a controller that avoids the instability the structure would damage.

Speeds [m/s]								
backward mass	0	10	15	20	25	30	35	37.5	40
Forward mass	0	10	15	20	25	30	35		40

Table 3.5: Test speeds for each configuration.

Approaching the speed of instability, the incremental step of the wind tunnel velocity ΔV decreases as a protective measure. On the contrary, in safety configuration this is not necessary and ΔV remains unchanged.

Excitation methods   The excitation method chosen for this test consists in the deflection of the control surface. The choice to excite the structure through the aileron is due to the simple implementation and its convenience of use. This single system permits to give several kind of inputs to the structure and so to observe the different responses.

The types of excitations used are:

- Pulse

- Band-limited white noise

- Sine

- Sweep

The same type of input is made for both experimental and numerical tests. Fig.3.7 shows the representation in simulink of the excitation scheme.

The last green box in fig.3.7 is the sweep excitation. This is passed as an up-Chirp signal excitation and it is constructed in such a way as to give an input to the system in the whole frequency band ranging from 3 to 15 Hz, with the same amplitude. In fact the frequency content of a chirp can be precisely chosen by through its period and starting and finishing frequencies, possibly tailored so to optimize its processing. The chirp signal is given covering the desired frequency content in 45 seconds. As for the normal sweeps mentioned before it is common to repeat the transient event more than once, averaging the results to get the final outcome.

This is obviously an ideal behavior because between desired input and real deflection output there is the transfer function of the motor which leads to
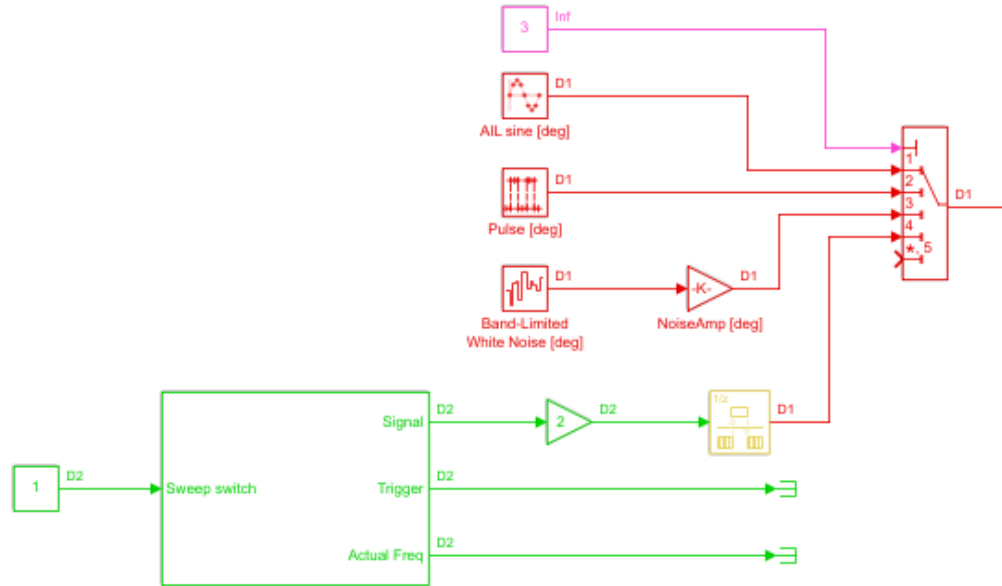
Figure 3.7: Simulink representation of inputs.

a loss of amplitude in frequency. All the features of the motor are available, including its input-output transfer function.

The most used excitation methods are the second and fourth: one manages to excite all the frequencies with a good energy content, allowing to take into consideration any type of dynamic response of the aircraft to an external excitation (always remaining limited by the transfer function of the engine); the other gives a sinusoidal input with a variable frequency over time, which covers the entire bandwidth of interest allowing us to analyze the response of the system in this range.

The pulse and the white noise excitation are equivalent in frequency domain. The advantage of using a pulse consist in being an *una tantum* excitation, it does not require a continuous intervention of the operator. In this way it is also possible to observe how damped is the mode. The same thing can not be done with a white noise forcing because it deals with a continuous signal. On the other hand it brings with it the technical disadvantage of being an instantaneous signal and so it forces to have an actuator with a fairly infinite bandwidth.

In addition, the pulse needs to have an higher value of deflection, because one single shot has to be able to cover with enough energy all the harmonics.

The band-limited white noise is random signal, by its definition, is un-

predictable and the values it assumes do not follow any deterministic law, hence the signal is not repeatable. A random signal can be characterized only using statistical indicators, e.g. its Power Spectral Density (PSD) in the frequency domain. Once more, the use of a random signal requires it has an approximately constant PSD in the frequency range of interest.

An advantage of this kind of excitation is the relative simplicity with which it is possible to define its frequency content through a shaping filter.

Experimental flutter results The methods used to calculate the V-g and V-f graphs are briefly presented below, starting from the experimental data acquired in the wind tunnel tests.

Data refer to the speeds previously presented in tab.3.5.

Fig.3.8b remark the coalescence of the modes, fig.3.8a shows the symmetrical torsional mode approaching to the 0 damping value with the increasing speed. In diagrams of fig.3.9 the expected behavior is respected, the aircraft become insensitive to the instability thanks to the pod mechanism and the flutter velocity moves forward.

Two different methodologies are adopted for the poles identification, in order to get more reliable values. They are labeled in the legends with (Exp) and (Exp-TestLab):

Exp In this case to draw the V-g and V-f diagrams is used a Matlab tool `modalsd`. The function `modalsd(frf,f,fs)`, provided FrF of the accelerometers at various points, generates a stabilization diagram. It estimates the natural frequencies and damping ratios from 1 to 50 modes and generates the diagram using the least-squares complex exponential (LSCE) algorithm. f_s is the sample rate. The frequency, f, is a vector with a number of elements equal to the number of rows of the FrF matrix. This diagram can be used to differentiate between computational and physical modes.

TestLab The same approach is implemented in TestLab, pLSCF (Polyreference Least-Squares Complex Frequency domain estimator) or PolyMAX. The main difference lies in a subsequent optimization of the modal model parameters through MMLM (Maximum Likelihood estimation of a Modal Model) made on PolyMAX, which gives a better estimate of the structural damping in the case under examination.
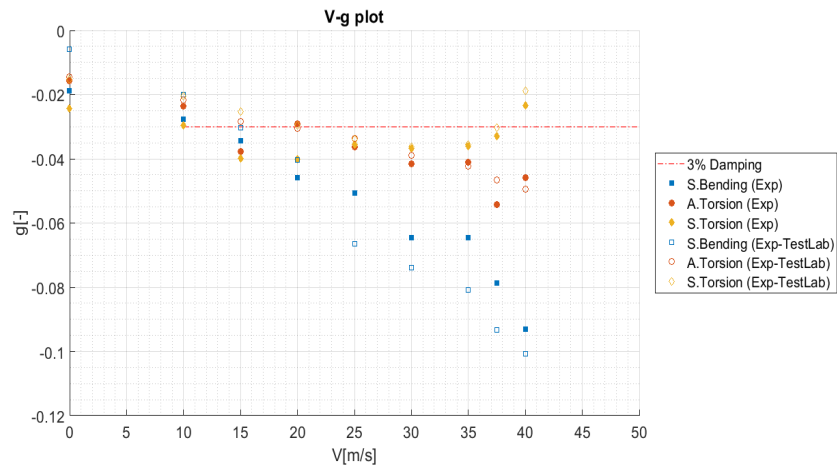
(a) Damping variation.
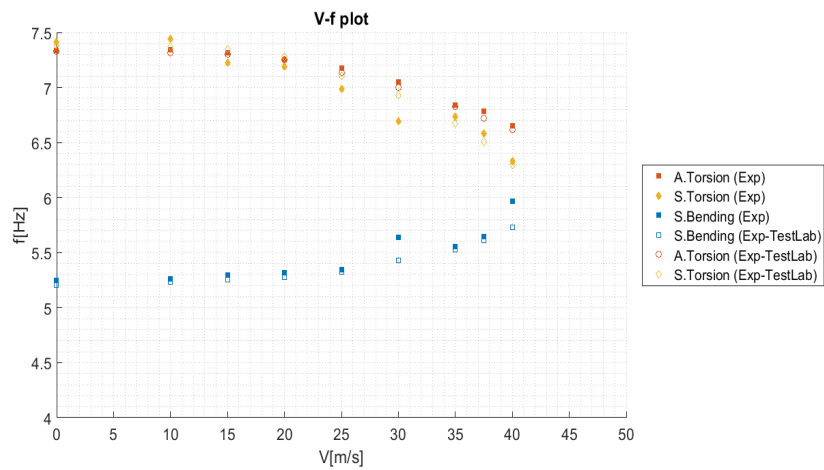
(b) Frequency variation.

Figure 3.8: Flutter analysis results with mass placed in backward position.

(a) Damping variation.

(b) Frequency variation.

Figure 3.9: Flutter analysis results with mass placed in forward position.

3.2 Comparison

After having collected all data of two model, a close examination establishes if the numerical model is actually well correlated with the real X-DIA. So, the graphical comparison between numerical and experimental results is reported below:

Modal properties A first acknowledgement is determined through the modal analysis.

In order to see what are the well correlated modes is useful a CROSS-MAC analysis.
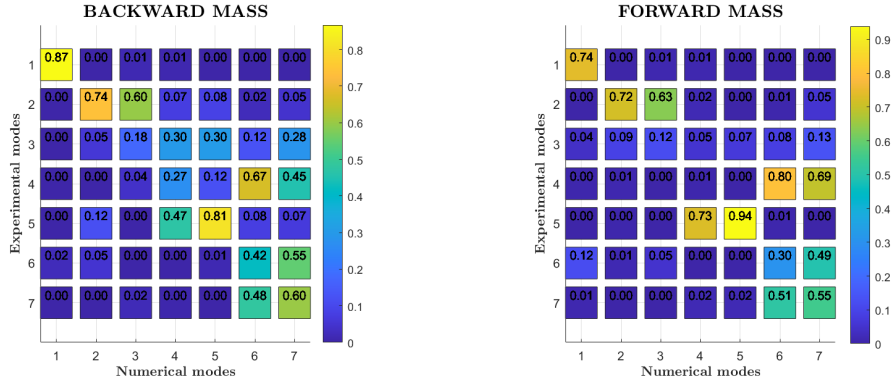
Figure 3.10: CROSS-MAC matrix of the stick model

Besides the error on the frequencies of these mode are reported in tab.3.6.

GVT	Freq [Hz]	Stick	Freq [Hz]	Error [%]
1	5.20	1	5.19	0.06
2	7.43	2	7.33	1.29
3	7.88	3	7.47	5.17
4	8.26	6	8.94	8.21
5	9.10	5	8.79	3.37
7	12.49	9	12.25	1.94
8	13.46	10	14.43	7.23

Table 3.6: Frequency error of stick model.

The errors on the frequency are limited and the CROSS-MAC is quite diagonal dominant, except for some coupling terms. But in order to certify the correlation for the work aim is fundamental checking the flutter condition.

Flutter condition   The check is done by overlapping the graphical results and comparing the mode evolution and the flutter point.
In backward mass configuration, the flutter speed changes from a value of $41.5m/s$ for experimental model to a value of $45.5m/s$ for numerical model. The error in capturing exact speed is 9.6%.
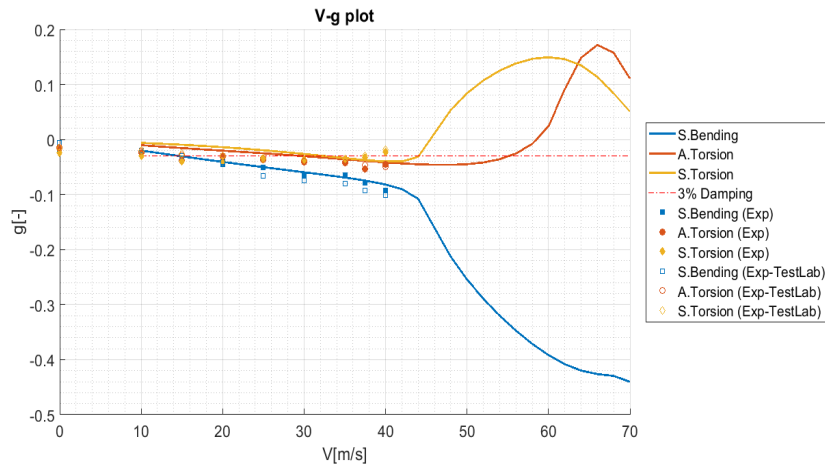
(a) Damping variation.
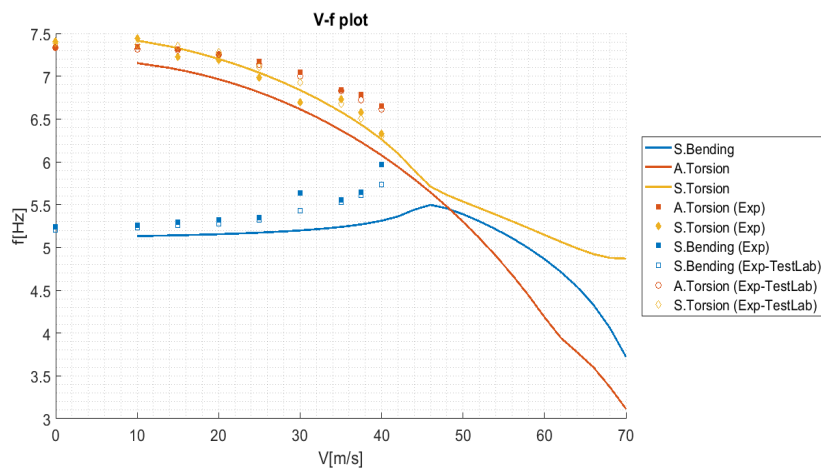
(b) Frequency variation.

Figure 3.11: Flutter analysis comparison with mass placed in backward position.
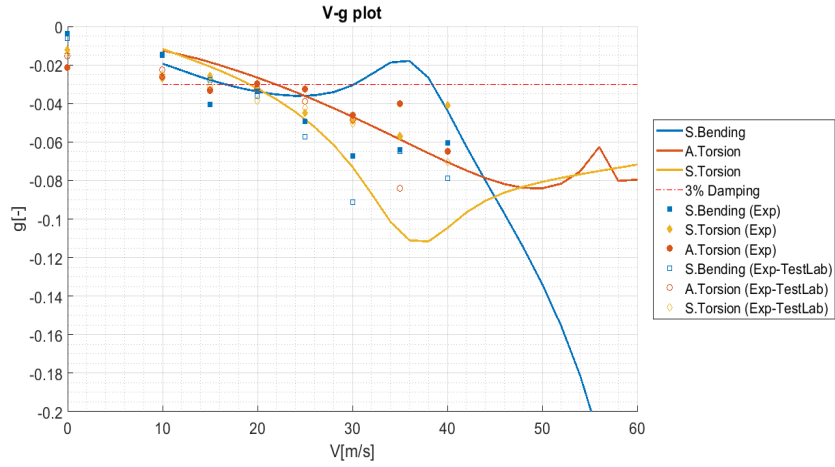
(a) Damping variation.
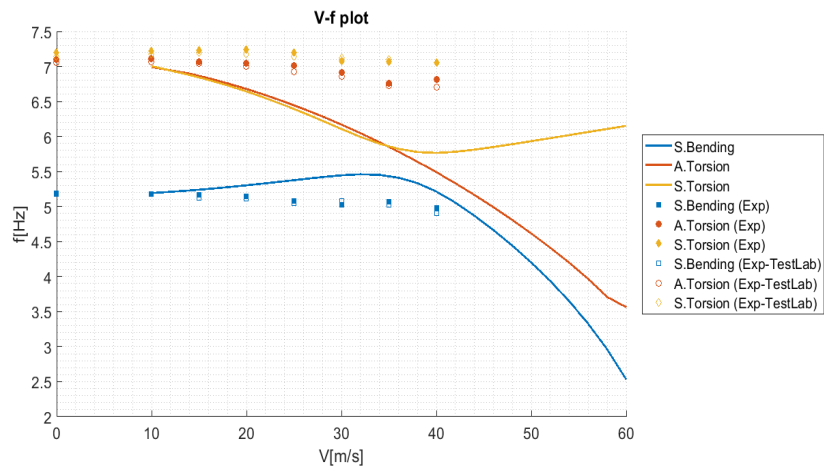
(b) Frequency variation.

Figure 3.12: Flutter analysis comparison with mass placed in forward position.

The frequency trend as a function of the speed of the first bending mode in the numerical model shows a different slope with respect to the experimental model. Variation probably due to non-exhaustive simplifying hypotheses (type of fuselage-wing attachment, error in identifying the behavior and stiffness characteristics of the main wing spar...).

With the mass in the forward position, on the other hand, the phenomenon of instability does not arise for the modes considered and in the speed range analyzed. From the graphs V-f of fig.3.12b it seems that somehow the modal behavior of the first three modes differs substantially from the real ones for this latter configuration.

A closer numerical examination instead clears the situation: the stick model is not able to catch perfectly the flutter behavior because the response is strongly dependent on the number of modes chosen for the numerical calculation. The fig.3.12 and 3.11 are the result of a SOL145 computed with 40 modes, that is an exaggeration and a useless calculation burden, since the modes interested in flutter are much less and correspond to the lower frequency ones. A series of analysis with the increasing number of modes are performed to verify if the model has more than one flutter mechanisms at higher frequencies. From those another problem could be observed: computing the response with lower number of modes the general behavior in this configuration changes completely and inexplicably, giving seriously wrong results (fig.3.13) in the forward mass configuration.
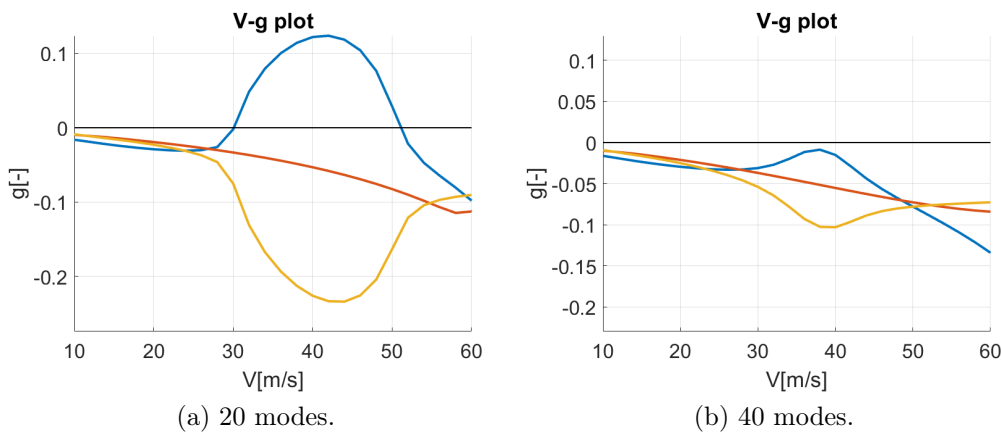
Figure 3.13: Flutter behavior changes by varying number of modes - forward.

Not fully satisfied with the behavior of the model in dynamic analysis, it is decided to move on to a detail model for the main component of analysis: the wing.

Chapter 4

Correlation phase

Once the experimental and numerical models are defined, it is necessary to compare them by means of indicators capable of highlighting if the simplifying hypotheses used are more or less appropriate for the purposes of the test in question. The correlation phase comes downstream of the identification and shows the goodness of the results.

The following chapter describes the method enacted to identify the models and extract fundamental data for the correlation phase. At the end of this process, thanks to the help of fundamental tools for validation, it is possible to understand the quality of the measurements made and the simplifying hypotheses assumed during the construction of the analytical model.
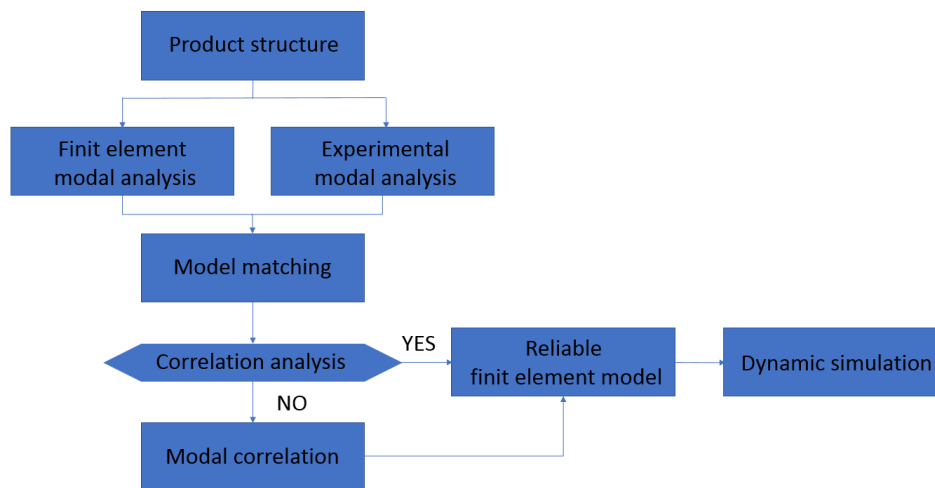
Figure 4.1: Procedure outline.

In fig.4.1 a typical correlation process is represented but also valid for the initial background phase just presented. The final output of this chapter is a model that accurately represents dynamic behavior. It will subsequently be used for the realization of a controller designed on the dynamics of the structure at low frequencies.

4.1 Numerical model

Previous results highlight how the mathematical model misses some important aspects of the real structure response, making a correction necessary. Since the flutter observed in wind tunnel tests involves mostly the wings, it is reasonable to act mainly on these and improve their quality.

The strategy adopted consists to leave the beam description of the wings and adopt a plate model reproducing exactly the geometry. In addition to the wings, it is decided to improve also the joining components between wings and fuselage or pod.

4.1.1 Plate model

The new approach to FEM model is founded on the dynamic properties recovery directly from the geometry, and not as result of an equivalent model. This procedure requires an exact knowledge of the real component: dimension, material, density etc. This kind of data are traced down in [3].

The wing response shows a more complex behavior with respect to the expected one. Certainly one of the reason is the complex shape of the cross section, an open omega geometry. This typology of cross section is particularly subjected to torsional effects, that are very important in flutter mechanism.

In this direction moves the choice of representing the geometry with a detailed FEM model. Obviously the FEM model is built in such a way to include only the component that contribute to the dynamics, so the decision is to reproduce only the main spar of the wing part, not the entire assembly that would include also the aerodynamic sectors.

SPAR

Structure So plate elements are used in place of beam ones, with a greater discretization, since the aim is to have an higher characterization of the local behavior.

This is translated in MSC/NASTRAN with CQUAD4 elements associated with PSHELL properties.
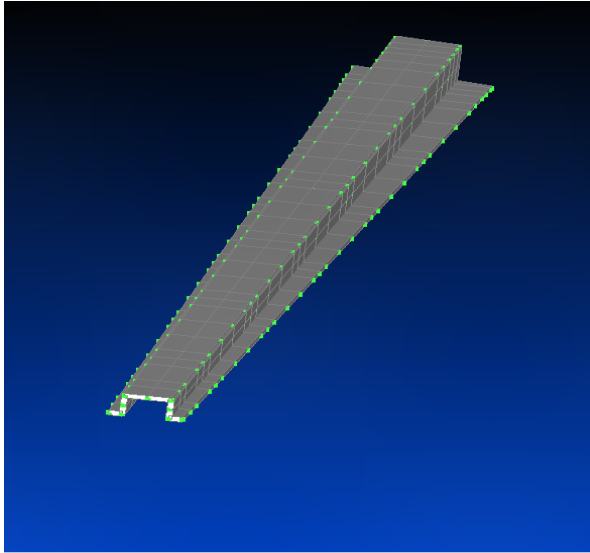
Component	Thickness
Side flanges	3.6 mm
Upper web	3.2 mm
Vertical webs	3.6 mm
Density	2717 kg/m^3

Figure 4.2: FEM model of the spar of the wing.

The thicknesses reported in fig.4.2 are not the real ones, in fact their nominal value (drawn from [3] - side: 3.4 mm, upper: 3 mm, vertical: 3.4 mm) is increased such that they can reproduce also the extra material that comes from fittings between the various web.

This model should follow the same cautions of the previous one, respecting the total mass and following the same distribution along wingspan.

The simpler requirement is to obtain the correct amount of structural mass, depending only on the density and thickness of the plate elements. But it only requires to built the model with the real values except in case of holes or discontinuities, corrected with small changes of these quantities.

Instead, in order to achieve the exact mass distribution (that is, transferring cables, sensors and bolts embedded in the structure into the numerical model correctly) several PSHELL cards are used with the aim of allocating to every sector the corresponding portion of mass.

A further adjustment consists in the type of element used to link the lumped masses (sensors, aerodynamic sectors, etc..) and the central core of the spar. In place of rigid RBE2 element, RBE3 are used. This choice is due to RBE2 element features: it transfers rigidly the displacement from one node to the other and this is a source of problem using plate elements, since the rotational degree of freedom normal to the shell plane (*drilling rotation*) has

a very low stiffness, so may be affected by numerical errors. More generally, extracting information from the rotational DoFs of shell nodes singularly is not recommended. Using RBE3 element, it is possible to recover the 6 DoFs of a selected node interpolating the displacement of a set of node, without using their drilling and rotational DoFs.

This strategy allows to have still a local description, but without being affected by numerical errors.

Splines   Since the structural mesh is changed, consequently the interface splines have to follow this mutation. A detailed model gives also the opportunity to reproduce the actual mechanism precisely. For this purpose it is suitable to use surface splines (SPLINE1) replacing the former linear ones. In particular, for the shell elements is strongly recommended use a surface interpolation method with the aim of avoiding the usage of the rotation DoFs of the nodes.

The set of structural nodes used for the interpolation is chosen with the aim of reproducing the actual transferring mechanism of forces. These nodes are created purposely to get this result.

One of them is placed in the middle of the aerodynamic sector, where the bolt connecting the cover and the spar should be. This node is connected with the rest of the structure with a RBE3 element interpolating the 3 translational DoFs of the surrounding part of the spar. This decision stems from the desire to give to this node a description of the local behavior of the connection zone. In fact the forces between the sector and the spar are exchanged exactly through the mechanism bolt-sector-spar.
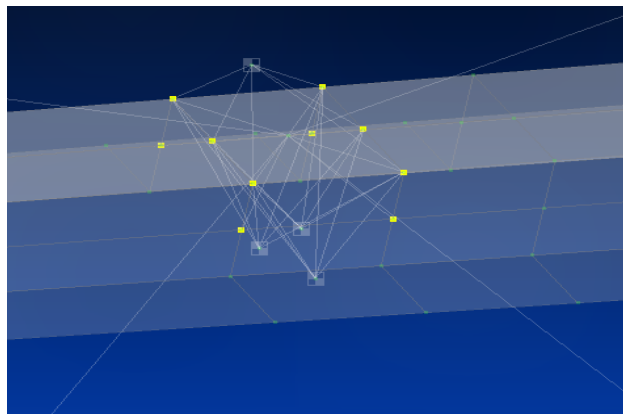
Figure 4.3: Nodes surrounding the cover-spar connection.

The rest of the set is composed of 4 nodes located in the corners of the

aerodynamic sector, with the intention of extent the spar behavior to the whole portion of the wing. These nodes inherit their displacements from the central node through an RBE2 element. The sector surface is hypothesized as rigid, whose DoFs are connected to the movements of the connection spar area. In fig.4.4 the RBE2 elements for the definition of the movements of the aerodynamic sectors for a correct setting of the surface splines.
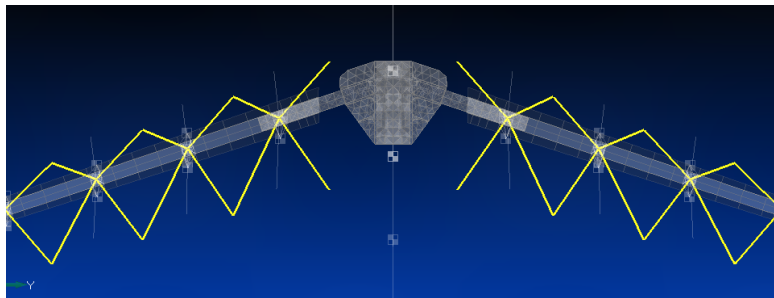
Figure 4.4: SPLINE1 structure.

CONNECTION COMPONENTS

The only modification on the wing spar may be not sufficient. From the experimental tests it appears that the bending and torsional mode are greatly influenced by the connection at both ends of the wing: the clamp (connecting the wing to the fuselage) and the bolts (connecting the pod to the last section of the wing).

(a) Clamp (from cad model).

Clamp Since the clamp has a large impact on bending mode (the constraint affect heavily the mode shapes) the decision is to model in an accurate way also this component. Due to its unusual geometry solid elements are used.
The problem of this kind of elements is the computational bur-
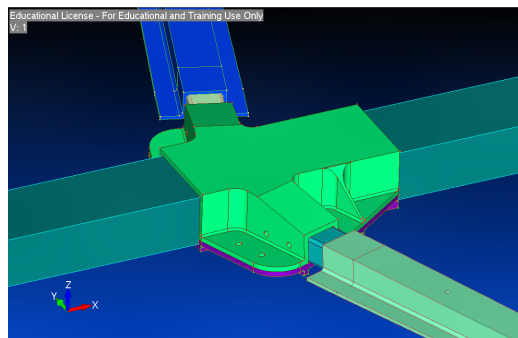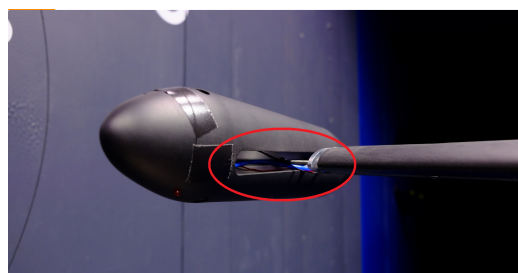
(b) Bolts.

den due to high number of DoFs. So the solution that should be adopted has to be a compromise between accuracy and computational cost.

A starting point is to verify that, modeling in this way the connection, its dynamics is actually separated from the wing one. The dynamic interaction between 2 components is not acceptable because the clamp has to hold the entire wing and attach it on the fuselage. Every possible dynamic amplification due to the coupling is not allowed.

This is a criterion that helps to choose the correct mesh refinement. After extracting the clamp from the CAD model, the meshing phase can start. Four different meshes are tested and analysed with a numerical modal test.

	Nodes	1st Frequency [Hz]
Mesh 1	616	1431
Mesh 2	1012	1318
Mesh 3	1929	1206
Mesh 4	6105	1119

Table 4.1: Convergence mesh analysis

Increasing the number of nodes the natural frequency of the first mode tends to settle around 1100 Hz (the higher is the number of nodes and the lower is the stiffness of the reproduced assembly).

One important thing to underline is that the modal analysis is performed on the half model, on the semi-clamp (like in fig. 4.5). This means that the frequencies of the real model are about half (settled around 500 Hz). In any case it is sufficient to assert the separation between the dynamic of the wing and clamp. In fact, it is shown in tab.3.4, the aircraft dynamic is very slow with respect to the clamp one, more than one order of magnitude.

So, all the meshes tested satisfies the coupling requirement. Therefore, the first one is chosen, since it has the lower computational burden and non-convergence will not unduly affect the structural dynamics of the rest of the model.

A correct FEM procedure involves also quality checks. They submit the clamp to some geometrical mesh checks in order to have the minimal mesh complying the quality requirements.

MSC/NASTRAN has many commands that allows to manage these inspections. The ones used are reported in tab. 4.2.

Type of check	Threshold
Q4_SKEW	30.
Q4_TAPER	0.5
Q4_WARP	0.05
Q4_IAMIN	30.
Q4_IAMAX	150.
T3_SKEW	10.
T3_IAMAX	160.
TET_AR	100.
TET_EPLR	0.5
TET_DETJ	0.0
TET_DETG	0.0
HEX_AR	100.
HEX_EPLR	0.5
HEX_DETJ	0.0
HEX_WARP	0.707
BEAM_OFF	0.15
BAR_OFF	0.15

Table 4.2: MSC/NASTRAN geometry checks commands.
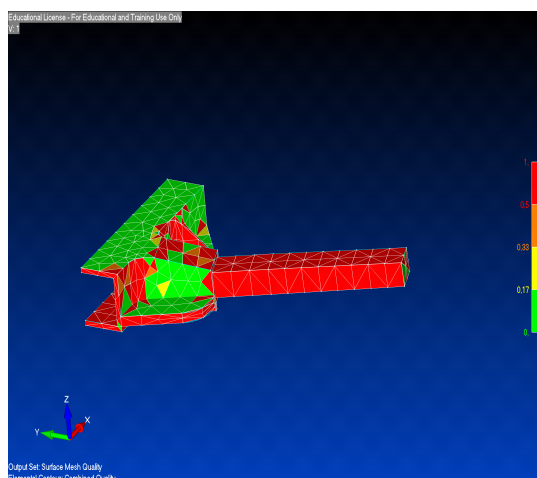
Figure 4.5: Mesh quality result.

As we can see in fig.4.5 this kind of mesh does not guarantee an high level of quality, also due to the specific geometry of the component. However this does not lead to problem for the purpose of flutter analysis since the clamp dynamics is greater than those excited in tests.

In the end, the mesh 1 (tab.4.1) is adopted for the FEM model.

The clamp is the joint element between fuselage and wing, so it has to be connected to both sides. The link with the fuselage is simply a rigid connection between the nodes of the end section of the clamp, dependent nodes in the RBE2 card, and a node of the beam at the same abscissa, this will be the independent one. On the other side the attach between the clamp and the wing spar needs some attentions. In the real X-DIA this is made indirectly, by means of an insert attached to the clamp and connected to the spar through 2 bolts, one per side (fig.4.5a). Implemented in MSC/NASTRAN, this solution does not provide the expected results, seeing the portion of insert preceding the bolts did not receive any loads. This can derive from some effect not captured, such that frictional effect due to interference between spar and insert. For this purpose the joint modeling is made by using GLUE elements along the entire length of the insert. These type of element introduce an elastic connection between 2 surface with a stiffness value (here it is used the default one) and suitable to reproduce friction phenomenon.

Pod attachment   This is a crucial point since presents a big cantilever mass linked with a fairly flexible connections (bolts) to a rigid section (fig.4.5b). From experimental test results, one can appreciate that the compliance introduced by this connection method produces a delay in the mode shape: the sensors on the pod read an acceleration out of phase with respect to the ones placed on the last section of the wing. Fig.4.6 shows clearly that when the
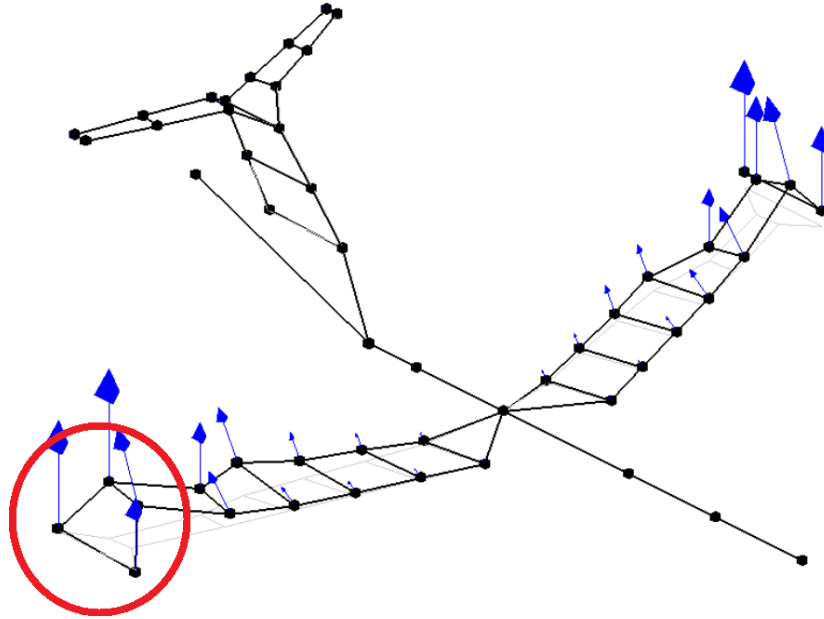
Figure 4.6: Experimental mesh: response delay due to the flexibility of bolts.

point at the end section of the wing gets its maximum vertical displacement, the point at the anti-flutter has not yet reached its top.

Spring elements are introduced in order to give this effect in the FEM model, as well as tuning the diameter of the bar used to model the connection bolts, and get a proper value of stiffness.

Choosing the values to assign to these variables is not so straightforward. To simplify the process it is decided to maintain the nominal diameter of the bars (1.5 mm) and to set the value of the stiffness of the springs that allows to match the experimental mode frequencies.

To build this strategy in MSC/NASTRAN the use of CELAS card is required. This card introduce a simple elastic element between two nodes, with a specific DoF and the respective value of stiffness about it. To insert

a spring on the aircraft FEM model is necessary to create a duplicate of the end connection bolts nodes. Given the couple of nodes, one of these will be related to the bar and the other linked to the pod. Then the coincident nodes are joined with a CELAS in the direction in which compliance is expected. In addition it is necessary to constrain the other DoFs of the couple of nodes with an RBE2 element, otherwise labilities are introduced in the system.
On the basis of several tests with different springs configurations has emerged that the only technique producing significant and suitable changes provides for linear spring along z direction. Flexibilities introduced in one of the other directions do not have remarkable effect on the frequencies of the modes of interest.
The CELAS adopted are shown below:

Bolt	Direction	Stiffness
Left forward	Tz	$5 \cdot 10^5$
Left backward	Tz	$5 \cdot 10^5$
Right forward	Tz	$5 \cdot 10^5$
Right backward	Tz	$5 \cdot 10^5$

Table 4.3: CELAS used in FEM model

A value of $5 \cdot 10^5$ for each spring is chosen to simplify the process.
The result of these choice is shown in sec.4.1.2.

AERODYNAMICS

The aerodynamic part does not require massive adjustments.

Aerodynamic mesh   The changes made on the structure bring only little attentions on the aerodynamics part. It is just necessary to translate the aerodynamic mesh since the position of the structural nodes is changed. Any other enhancement has no remarkable effect on the results since a convergence analysis has already performed. In fact, according to the recommendation illustrated in [12], the number of boxes has to be chosen on the basis of the quantities involved in the problem.
The illustrated condition is:

$$\frac{c}{\Delta x} > \frac{k}{0.08\pi} = 4 \cdot k \tag{4.1}$$

with a reduced frequency $k = 0.38$ considering a minimum velocity of interest $V = 30 m/s$ and maximum frequency of interest $f = 15 Hz$.

The left hand side of the eq.4.1 represents the number of box along the chord, the right side gives a result of 2 box on a chord approximately. This allows to obtain converged aerodynamic coefficient. Recent studies indicates that $k/0.02\pi$ is needed to get also converged stability derivatives.

$$n_{box} = k_{max} \cdot 4 = 0.38 \cdot 4 = 1.52 \qquad for\ coefficients.$$

$$n_{box} = k_{max} \cdot 16 = 0.38 \cdot 16 = 6.1 \qquad for\ derivatives$$

both request are satisfied, since the model presents 10 panel per chord. Moreover, for subsonic case, an aspect ratio between two dimensions of the panels less than 3 is acceptable. In this case, the value is about 2.20 respecting conditions on subsonic flows.

4.1.2 Modal analysis

The correlation process necessarily passes through the equivalence of the dynamic properties, as previously explained.

Mass Properties A first step is always to ensure the same mass properties (see sec.2.3.1) between the structure compared. The use of several PSHELL cards permits to fulfill the request of perceiving the mass distribution, both of structural and non-structural one.
The total mass of the aircraft:

FEM model	Real model	Error
	Half-wing	
1.37 kg	1.33 kg	3 %
	Structural	
58.55 kg	58.49 kg	0,12 %
	Total	
59.49 kg	59.42 kg	0.11%

Table 4.4: Mass properties comparison

With this mass distribution the center of mass of the structure has the following characteristics.

Figure 4.7: Global reference frame.
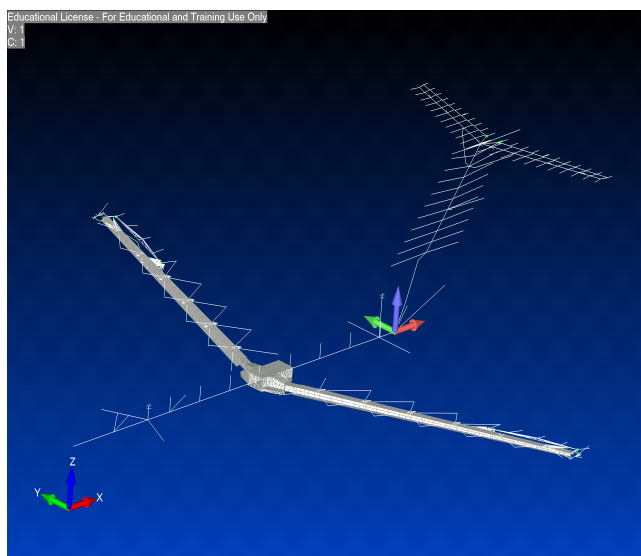
Global Reference Frame	
x_{CG}	-0.779 m
y_{CG}	0.0 m
z_{CG}	0.077 m

As can be noted in center of mass result, the aircraft is symmetric respect to xz plane, given $y_{CG} = 0$. This should also be reflected in the rigid inertia matrix.

$$\begin{bmatrix} I_{xx} & I_{xy} & I_{xz} \\ I_{yx} & I_{yy} & I_{yz} \\ I_{zx} & I_{zy} & I_{zz} \end{bmatrix} = \begin{bmatrix} 14.52 & 0 & -0.63 \\ 0 & 61.90 & 0 \\ -0.63 & 0 & 73.09 \end{bmatrix}$$

Mode Shapes   Verifying the modal correlation means to catch both modal parameters, frequencies and mode shapes. Only in this case the dynamic behavior of the models is equivalent.

In flutter phenomenon the mode shapes are very important and they can affect massively the structural behavior, because they are the tools that describe the divergent trend. So improving the quality of these results can be a key point for flutter analysis accuracy.
The new hybrid model, composed of both beam and shell elements, should exhibit mode shapes more descriptive of the X-DIA response.

The method to check the correct identification of the modes is the MAC matrix. For correlation purposes the procedure suggest to use a CROSS-MAC analysis, as already done with previous analysis in sec.2.3.3.
A CROSS-MAC that manages correctly the data should be built starting from DoFs of models under observation as much as similar as possible. To fulfill this condition, specific nodes are create on the exact position where ac-

celerometers are located on the experimental model, in order to have meshes that exactly match.
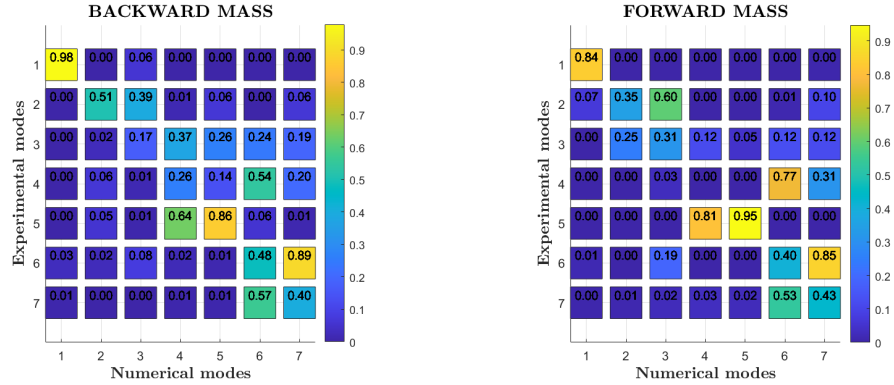
Figure 4.8: CROSS-MAC matrix of the hybrid model

Fig.4.8 reports the MAC analysis only for few modes and provides a good guidance on which modes are well correlated.

Some conclusions can be drawn from this indicators:

- The 1st bending mode is captured excellently, in particular in the mass backward configuration. This is very important for the flutter interest, because from experimental tests comes out that the divergent mechanism involves the 1st bending and the 2nd torsional (mode $n°3$).

- The torsional modes are not caught with a good accuracy. This can be due to the asymmetry of the real X-DIA model, as opposed to the numerical one.

- There are some couplings between the higher frequency modes - 6th and 7th, or 4th and 5th for backward mass one-. These mixing effects results from the bad interpretation of the accelerometers data: the sensors are mono-axial and directed along z axis in order to read out-of-plane displacement, so they miss all the other components (in-plane bending + out-of-plane bending results only in out-of-plane shape); furthermore the strong difference in the number of DoFs between 2 model (the analytical model has some modes that the experimental mesh used during GVTs did not catch).

Natural frequencies Analyses based on mode shapes are more complicated to carry out, since results are influenced by many variables, there can

be a lot of DoFs involved. Furthermore, the results of the GVT tests about the mode shapes are not so confident, usually the error committed measuring and identificating them can be even a 10% of the real value.
For these reason is recommended to focus on the natural frequencies, easier to deal with and more accurate (error committed is about on 1%.)

As done before, it is necessary to guarantee a small error only on the lowest modes. Moreover, since the flutter mechanism acts on the out-of-plane displacements, the in-plane modes are not interesting for the purpose of this analysis, so those frequencies are not involved in the following correlation process.

Mode	Freq [Hz]	Mode	Freq [Hz]
1	0.307	11	11.09
2	1.210	12	12.19
3	2.499	13	13.17
4	3.369	14	14.04
5	5.589	15	14.42
6	6.851	16	18.70
7	6.867	17	19.55
8	8.166	18	20.05
9	8.936	19	22.16
10	9.067	20	23.82

Table 4.5: Frequencies with mass in backward position.

Mode	Freq [Hz]	Mode	Freq [Hz]
1	0.307	11	11.14
2	1.210	12	12.23
3	2.501	13	13.31
4	3.367	14	14.37
5	5.429	15	14.42
6	6.293	16	18.73
7	6.567	17	19.82
8	8.165	18	20.78
9	8.933	19	22.29
10	9.067	20	23.57

Table 4.6: Frequencies with mass in forward position.

4.1.3 Flutter analysis

The modifications introduced in the model serves to improve the prediction of the dynamic behavior of aircraft, in particular in safety condition where the previous model was less precise.

It is decided to analyze the first 20 modes, in order to see if also higher frequency mode reach instability condition. The phenomenon to simulate has a bandwidth of interest going from 3 Hz up to 15 Hz (that is the bandwidth of the excitation). The interest is to observe and study the dynamic behavior around the flutter condition, that experimentally turns out to be at about 40 m/s.

So the range of reduced frequencies of interest is:

$$k_{min} = \frac{2\pi \cdot 3Hz \cdot c}{2 \cdot 40m/s} = 0.058$$

$$k_{max} = \frac{2\pi \cdot 15Hz \cdot c}{2 \cdot 40m/s} = 0.287$$

Identifying the frequencies in which the phenomenon takes place is important to built correctly the generalized aerodynamic matrix $H_{am}(k, M)$. It is good practise in aeroelastic analyses to extend the set of reduced frequencies with an eye to avoid erroneous estimation of H_{am}, since MSC/NASTRAN builds this matrix, for each step of the flutter resolution method, interpolating between specific values, passed to the software by means of MKAERO card. So, very small values (such as $k = 0.001$, $k = 0.005$, etc..) and high ones ($k = 1$, $k = 2$) serve to avoid extrapolation instead of interpolation between known configuration of H_{am}.

The results are expressed in terms of V-g and V-f diagrams in fig.4.9 and 4.10 for both configuration in question.

As expected the model presents flutter with the mass placed in the backward position (fig.4.9), at a velocity of about $32m/s$. In particular 5th and 6th mode are the ones involved in the instability, that are respectively the first bending and symmetric torsional, as observed by means of the experimental wind tunnel test. In reality, as the p-k method works, when the modes approach graphically it is possible that they exchange. So the 6th and 7th modes are likely to have reversed during computations.

Instead with the mass in forward position (fig.4.10) no modes couple and none cross the line of zero damping.

All the analyses are performed with 40 modes for flutter, but it is graphically useful to restrict the results only to the lower frequency modes, in fact in the figure is presented the evolution of only the first 20 modes (excluding the first 4 rigid modes).

For a better understanding of the graphs in fig.4.9 a description of the modal shapes of the first 15 modes is given below.

- 5:(5.59 Hz) First bending mode of the wing.

- 6:(6.85 Hz) First anti-symmetric torsional mode of the wing.

- 7:(6.87 Hz) Second symmetrical torsional mode of the wing.

- 8:(8.17 Hz) Tail vertical plane bending mode and slight bending + torsion of the wing.

- 9:(8.94 Hz) Tail vertical plane torsional mode.

- 10:(9.07 Hz) Bending mode of the horizontal tail plane and in general the main contribution is the tail plane one.

- 11:(11.09 Hz) Bending mode of the horizontal tail plane + in-plane mode for the wing.

- 12:(12.19 Hz) Bending mode of wing, horizontal tail plane and fuselage.

- 13:(13.17 Hz) In-plane of wing and tail plane contribution.

- 14:(14.04 Hz) Bending anti-symmetric mode of the wing.

- 15:(14.42 Hz) Bending horizontal tail plane + slight contribution of the wingtip.

The first 15 modes are those that have modal frequencies below the excitation frequency used in the wind tunnel that reaches up to 15 Hz in the case of the sweep. Modal frequencies of each mode are listed in tab.4.5 for configuration with mass in backward position and in tab.4.6 for forward one. The higher frequency modes were analysed but no description is reported.

In configuration with mass in forward position the description of the modal shapes in the frequencies of interest remain unchanged and for display simplicity they are not reported.

In the fig.4.11 the modal deformations of the modes involved in the flutter phenomenon for the new plate model are reported. They must be compared with the deformed ones of fig.3.5 to clarify the difference between the two models (real and implemented in MSC/NASTRAN) especially in terms of symmetry.
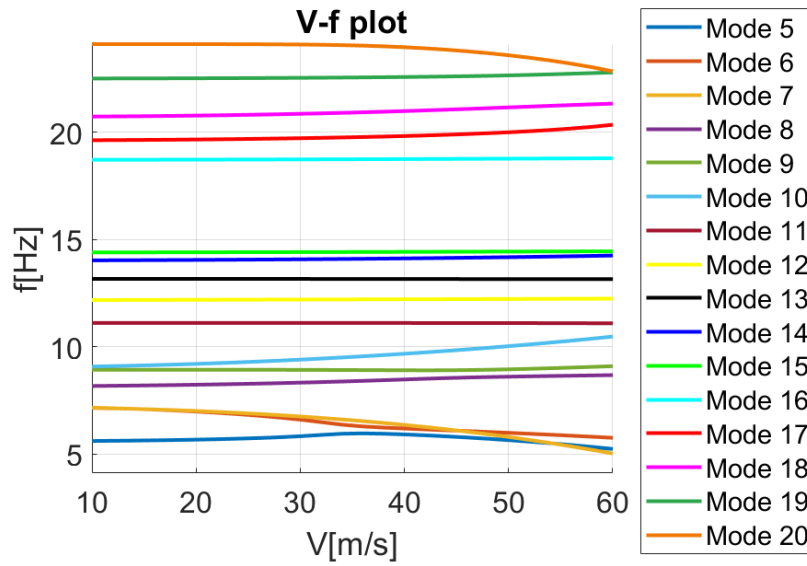
(a)
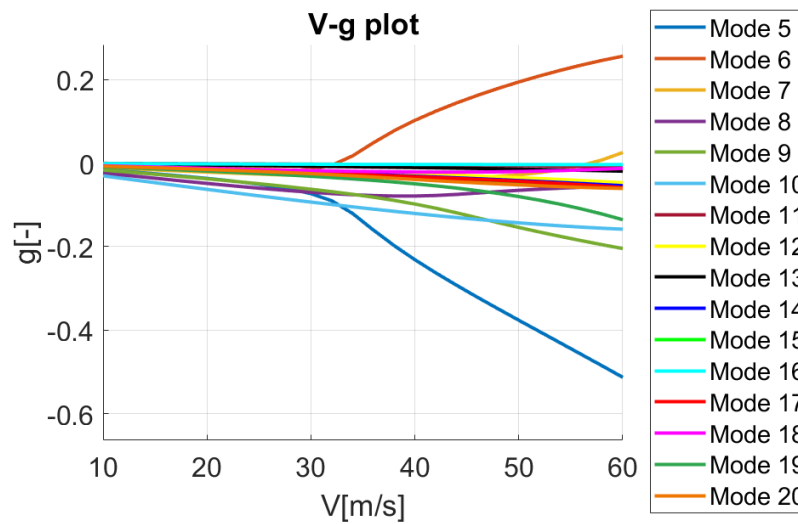
(b)

Figure 4.9: Flutter result with mass in backward position.
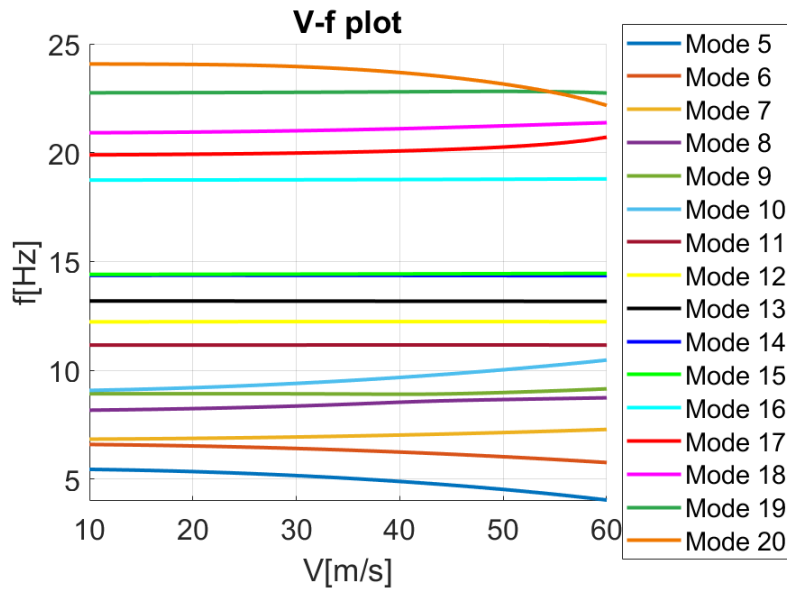
(a)
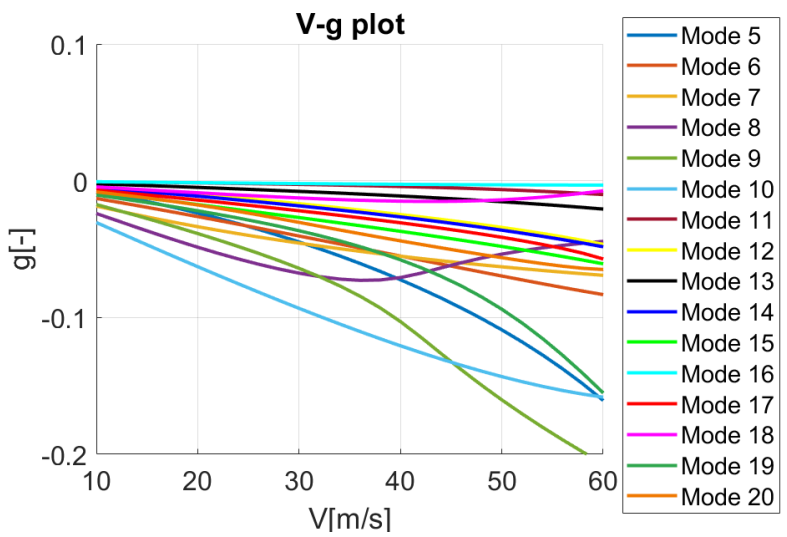
(b)

Figure 4.10: Flutter result with mass in forward position.
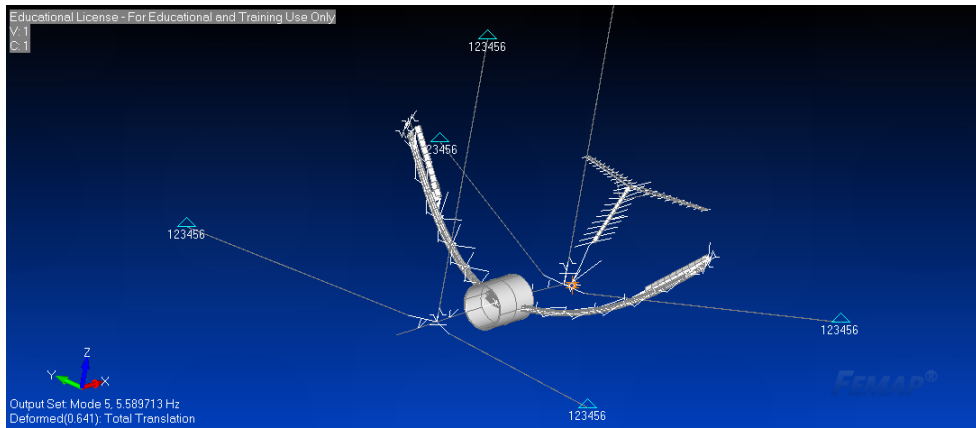
(a) Mode 5, 5.59 Hz.
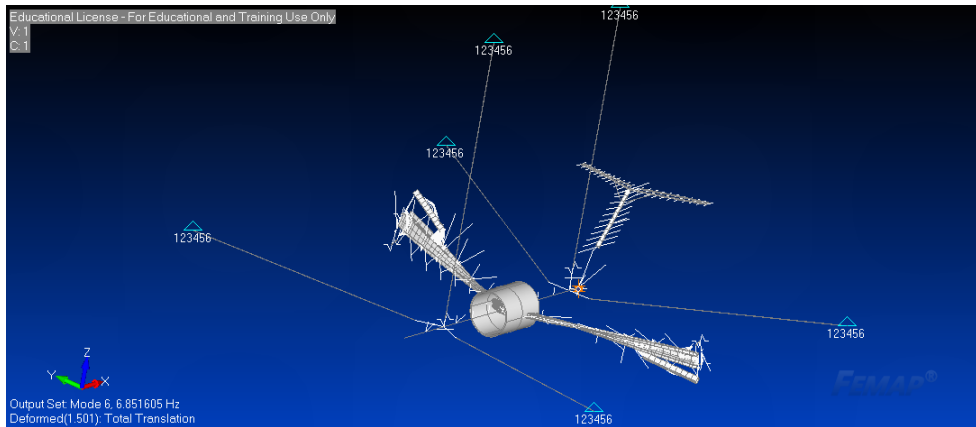
(b) Mode 6, 6.85 Hz.
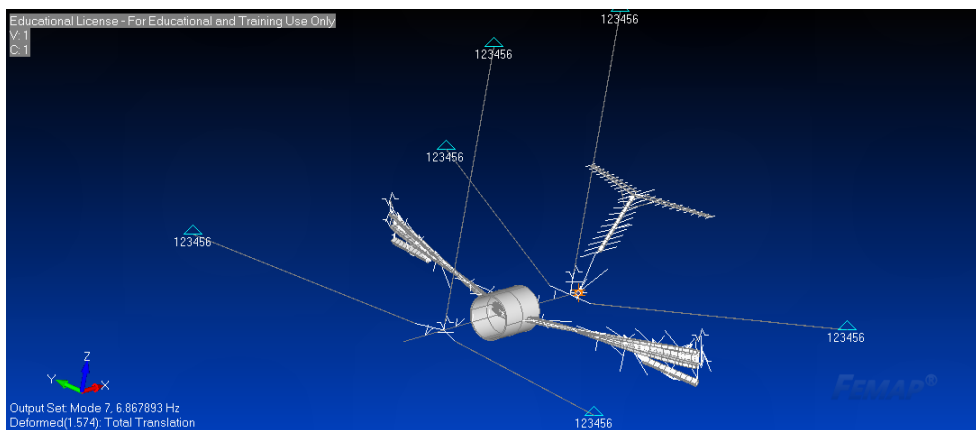
(c) Mode 7, 6.87 Hz.

Figure 4.11: Configuration 1: mode involved in flutter.

4.2 Comparison results

The new hybrid model, that mixes plates and stick elements, should show an aeroelastic behavior closer to reality. In fact, the stick model is unable to predict correctly the phenomenon, as already seen in sec.3.2.

4.2.1 Modal properties

During the modifications made on the FEM model the aerodynamic modeling has undergone only small changes, so all the improvement should come out from structural point of view.
For this reason and also for the simpler analysis tools, the structural properties are the first results to be inspected.

Mode shapes Performing an initial MAC analysis serves to identify the correlated modes (modes that have a correlation index greater than a certain value, commonly 0.8) and get the minimum set of numerical-experimental match, on which the final evaluation will be based.
Starting from the stick model results, it can be seen that, after the modification introduced in the model, the correlation with the bending modes is strongly improved, in particular with the first one that is one of the modes involved in flutter instability.

(a) Stick model. (b) Detailed model.
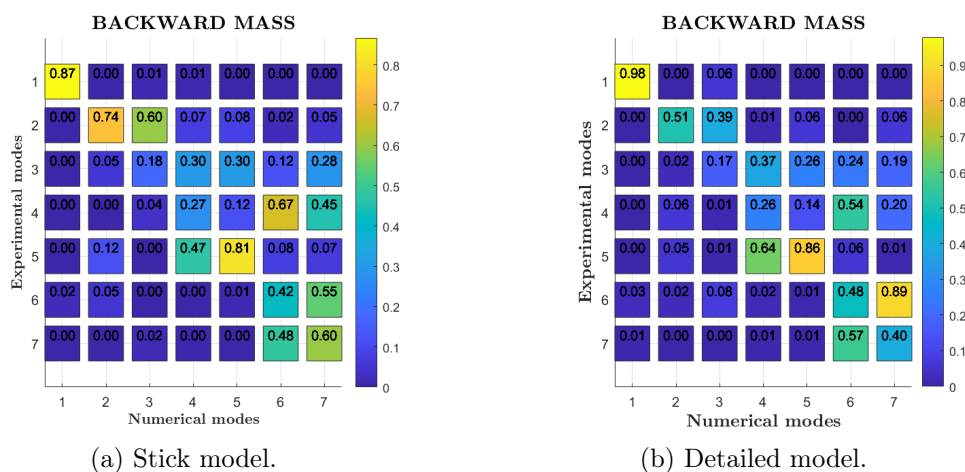
Figure 4.12: Mass backward

(a) Stick model.   (b) Detailed model.
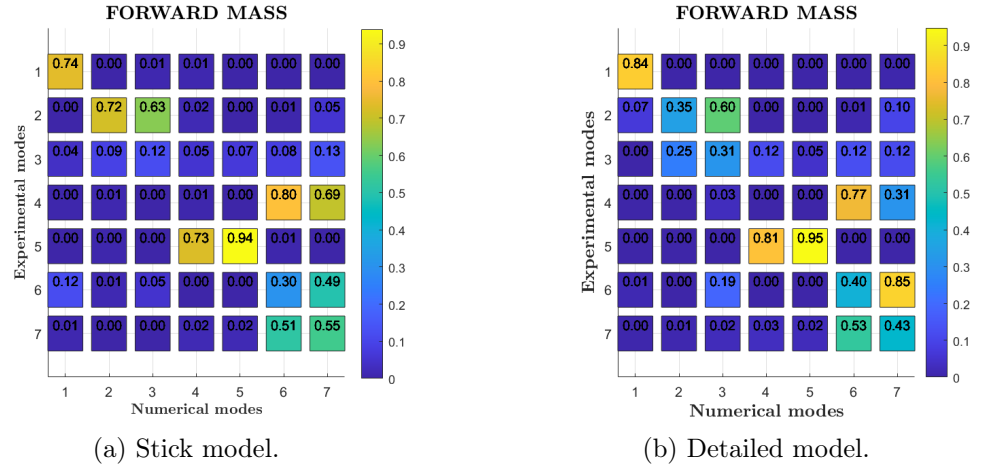
Figure 4.13: Mass forward

On the other hand, the torsional modes of the hybrid model worsen their correlation with respect the stick one. This can be due to 2 factors:

- the stick model is an equivalent model and its aim is to reproduce global quantities, so it is built in such a manner to show characteristics more similar as possible to the reality. In fact all the section properties are introduced manually in PBEAM cards, after having recovered them from CAD model.

  Instead the plate model is a detailed model, built to reproduce the geometry correctly and from it then obtains the section properties. The real change occurs in structure due to the different type of element and to the law that governs it. This takes to different laws dealing with structural behavior and leads to a different stiffness of the structure replacing its modal forms. The real difference is in the transition from global to local behavior.

- The confidence in the mode shapes results is not very high, this brings to not rely on MAC indices. In fact, from GVT data emerge that, in the 1st and 2nd torsional modes, only one half-wing per time takes part to the motion. Instead in numerical shapes both half-wings participate in each torsional modes (fig.4.14a). This means that necessarily there are some DoFs of 2 model that do not share the same displacement, so it provides a lower value of MAC index.

(a) GVT torsional mode.

(b) Numerical torsional mode.
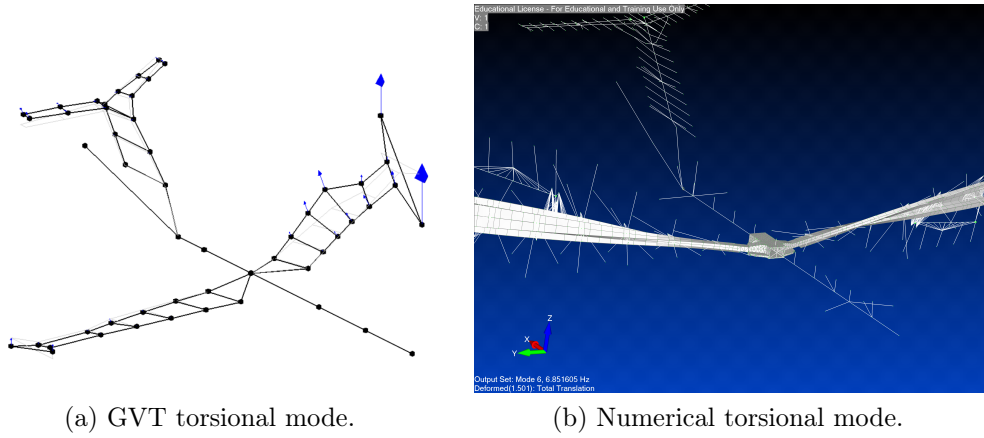
Figure 4.14: Comparison between torsional modes

Frequencies Thanks to the MAC analysis it is possible to show which modes correspond between numerical and experimental set and focus only on the correlated ones. Starting from this reduced set, the results of the comparison between the numerical and experimental frequencies are presented in tab.4.7

GVT	Freq [Hz]	FEM	Freq [Hz]	Error [%]
1	5.20	1	5.59	7.49
2	7.43	2	6.85	7.78
3	7.88	3	6.87	12.84
5	9.10	5	8.93	1.79
6	10.38	7	11.10	6.91
7	12.49	8	12.19	2.40
8	13.46	11	14.42	7.13
9	14.74	9	13.17	10.63

Table 4.7: Frequency error.

4.2.2 Flutter condition

As first approach to the problem the aerodynamic of the anti-flutter device is not taken in account in order not to introduce further variability in the analysis. Successively, for a greater completeness, it should be introduced.

In fig.4.9 and 4.10 it is possible to observe the flutter response of the hybrid model, but it is interesting to compare it with experimental results.
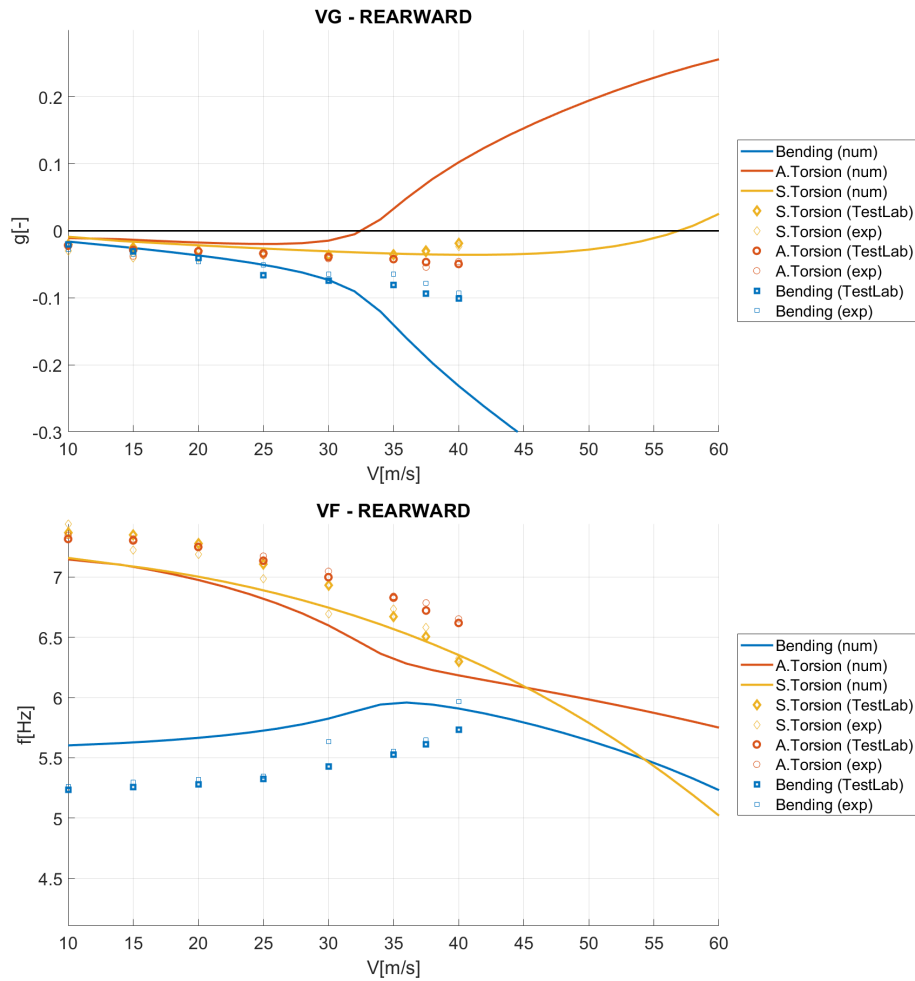
Figure 4.15: Flutter numerical vs experimental results.

From the V-g plot of fig.4.15 turns out that the velocity for which starts flutter condition is about 32.5 m/s, with an error of 21.7%. Also the evolution of the poles of flutter problem is not caught with enough precision.

The new FEM model is not accurate as required and the prediction is still too rough. The positive aspect is that now the model has sound basis and it is able to catch the general aspect of the flutter functioning, beyond the entity of the error. In fact, the detailed model does not present the numerical problem showed by the stick one in fig.3.13. Actually the structure does not alter its behavior by varying the number of modes used to compute the problem, but keeps the same attitude.

(a) 10 modes.   (b) 40 modes.
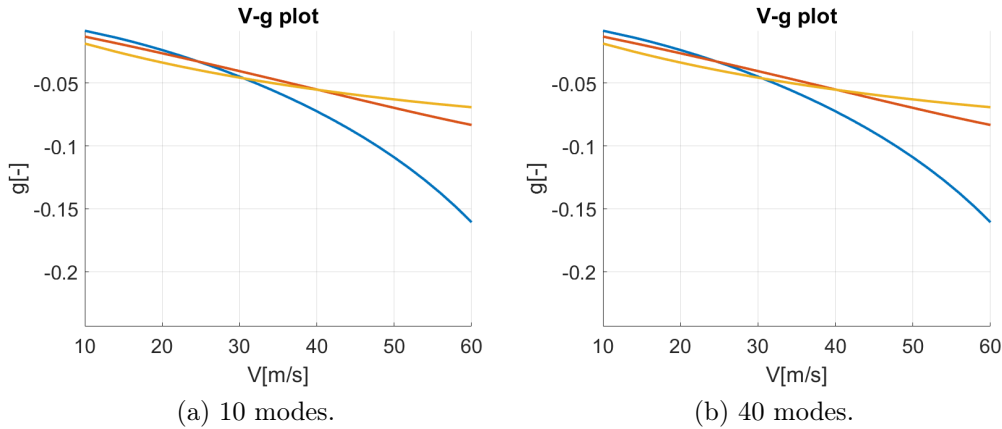
Figure 4.16: Flutter behavior changes by varying number of modes - forward.

4.3 Updating

With a prototype of an aircraft, GVTs are essential to validate and improve the dynamic finite element model. The improvement process, called *model updating*, is a numerical-analytical procedure to update the numerical model in order to produce results correlated with those measured during the experimental modal analysis. This optimisation procedure is established to minimise the differences between the analytical model and the experimental data.

However it is not straight-forward and in most cases requires significant user experience.

Various successful model updating methods have been developed to work on the matrices representing the dynamics of the system, i.e. mass and stiffness matrices. Such matrices can be extracted from a FEM model. The results of these updating methods are modified matrices representing an improved dynamic model.

However this powerful methods have inherent drawbacks.

- The original physical properties in the FEM, for example the translational and rotational stiffness of an element, the thickness of a membrane element, etc., cannot be reconstructed from the resulting matrices.

- It is difficult to maintain the physical meaning of the problem: the excessive number of variables with respect to the constraints imposed (e.g. reproduce the first n frequency properties) can provide solutions

that respect those constraints but not the properties of the real structure. Properties of FEM can be modified but, for example, final mass must remain the one of the real structure.

- Localized structural changes tend to spread throughout the entire model. Since most of algorithms are based on gradient calculation, the solution is modified in the whole domain even if the error is well localized

- It does not admit a unique solution.

- Usually the number of parameters is much higher than the number of possible constraints, which are related to the measured modes.

- Ill-conditioned: the solutions are very sensitive to small disturbances of the initial data.

In an industrial environment where loads and flutter analyses are mostly carried out using FEM approach, these drawbacks are considered to be significant. For the present work, updating methods which work directly on the FEM are therefore preferred. The results for this approach are updated physical properties of the elements which can be implemented in an updated numerical model and can be conveniently interpreted.

The analysis tools that benefit from the updated dynamic model have to be able to work with the updated matrices. MSC/NASTRAN has an own process, it uses a variety of optimization algorithms from the *MSCADS* suite of algorithms as well as the *IPOPT* algorithm [13].

Sources of error   There are many sources of error in an analytical model. These errors can be classified into several categories.

1. *Modeling errors* between the physics of the aircraft and the analytical model. Errors belonging to this category are mostly originated from an over-simplification of the physics, for example:

   - Linearization error of a strongly non-linear problem.
   - Simplified structural model that is not fully descriptive of the real behavior (e.g. a solid structure with three-dimensional properties is modeled using plate elements, etc.)
   - The use of too many lumped masses to model distributed mass, etc.
   - Wrong assumptions on the boundary conditions and joints, e.g. clamping for a flexible joint or boundary.

Overly simplifying hypotheses would lead to a reading of incorrect features of the model.

2. An *analytical model* is introduced by the analysis tool FEM or the more specific approximation such as static/Guyan condensation, etc. Can be present aspects such as the element type, i.e. linear or quadratic, and mesh density, etc.

3. Determination of the *parameters* for the numerical model. Typical examples in this category are:

   - The value of Young modulus, shear modulus, mass density, etc.
   - The property of the beams, i.e. sectional area, area moment of inertia; property of spring elements, etc.

The updating in this section focuses on the last category of error, i.e. model parameters. An automatic updating method based on optimisation technique is employed. It should be noted that, although the model updating is achieved through variation of the model parameters, this updating implicitly tries to compensate for errors of the first two categories as well. For the analysis and optimisation, it is decided to use MSC/NASTRAN instead of using a specialised model updating software for simplicity.

4.3.1 Procedure

The correlation is made starting from the GVT values and the initial analytical model to arrive at the final model with variations that should bridge any modeling errors or structural parameters.

For a dynamic FEM model, differences with respect to the results of a GVT can be evaluated from the natural frequencies, the mode shape and the modal mass. It is assumed that these differences are caused by the errors in the analytical model.

MSC/NASTRAN optimizer gives the possibility to base the error to minimize many kind of variables, flutter velocity as well. For simplicity, the initial setup is chosen to act on the modal parameters, in order to match the GVT's ones. In the event that this procedure is not sufficient, a possible solution could be setting the error directly on flutter velocity

Objective function is defined to minimize the differences in the natural frequencies and the differences in the mode shapes between the analytical model and the GVT data in this particular case. Unfortunately, although MSC/-NASTRAN has the possibility to set the objective function on the modal

shapes thanks to the extraction of the displacements from the output file f06. Due to technical problems with the new software version it was not possible to insert the modal shapes in the objective function. The chosen functional thus optimizes only the natural frequencies of the structure.

The algorithm requires to define an error function to be minimized that shows the differences between numerical model outputs and experimental data obtained. Since the variable chosen is the frequency, the error will be a vector of this type:

$$\varepsilon = \frac{|f_{GVT} - f_{numerical}|}{f_{GVT}}$$

Where $\mathbf{f_{GVT}}$ are natural frequencies extracted from measurements during GVT and $\mathbf{f_{numerical}}$ those of the numerical model found with SOL103, MSC/-NASTRAN solver for modal analysis. $\mathbf{f_{GVT}}$ and $\mathbf{f_{numerical}}$ are those reported in tab.4.7. Therefore it is desired that the modal shapes with the same characteristics have frequencies as close as possible.
So, the optimization process can be setup to minimize this error by defining the objective function to be the sum of squared error as

$$Obj = \boldsymbol{\varepsilon}\boldsymbol{\varepsilon}^T \tag{4.2}$$

As generally known, experimental data may contain inaccuracies. In most cases, the inaccuracy varies between modes. Therefore it could be appropriate to express the minimization problem with a weighted-squared sum type of objective function:

$$Obj = \boldsymbol{\varepsilon}^T \boldsymbol{W} \boldsymbol{\varepsilon} \tag{4.3}$$

With $\mathbf{W}$ weight matrix containing possibly different weights for each mode frequency as a function of the confidence on the data test acquired.

A complete cost function with the possibility of expressing all modal parameters it is presented below:

$$Obj = \boldsymbol{\varepsilon}^T \boldsymbol{W}_{freq} \boldsymbol{\varepsilon} + W_{shape_i} \cdot (1 - MAC_{reduced}) \tag{4.4}$$

Where $MAC_{reduced}$ is an entry of the $\mathbf{MAC_{reduced}}$ matrix, corresponding to a reduced set of key nodes and not to the complete set from the FEM model. Usually is the numerical mesh that is reduced and let coincide with the experimental grids. With this simplification the order of the problem under examination and the computational burden decrease.

4.3.2 MSC/NASTRAN implementation

The objective function passed to the optimizer has the form of eq.4.2 and appears as follows:

$$F\left(f_{gvt1}, f_{gvt2}, f_{gvt3}, f_1, f_2, f_3\right) = \left(\frac{f_{gvt1} - f_1}{f_{gvt1}}\right)^2 + \left(\frac{f_{gvt2} - f_2}{f_{gvt2}}\right)^2 + \left(\frac{f_{gvt3} - f_3}{f_{gvt3}}\right)^2$$

The equation written above is exactly the equation given to MSC/NASTRAN through the assignment of the DEQATN command.

Briefly, the description of the commands used and the process for setting up the optimizer using the SOL 200. The MSC/NASTRAN commands, the variables, the constraints and the setting of the problem are described below:

- DRESP1: Defines a set of structural responses that is used in the design either as constraints or as an objective function parameter.

  The DRESP1 cards used are 3 and define the modes inserted within the objective function. The modes are represented by the numbers 5, 6 and 7 in the DRESP1 card and indicate the first bending and the first two torsional modes (anti-symmetric and symmetric). The numbering starts from 5 because the first 4 rigid modes given by the presence of the free-free constraint are not of interest.

$$\text{DRESP1, 1, f1, FREQ, , , 5}$$
$$\text{DRESP1, 2, f2, FREQ, , , 6}$$
$$\text{DRESP1, 3, f3, FREQ, , , 7}$$

- DRESP2: Defines equation responses that are used in the design, either as constraints or as an objective.

  Here are included the data relating to the natural frequencies of the GVT through a DTABLE card, the ID of the DEQATN containing the objective function to be minimized and the DRESP1 used.

- DESVAR: Defines a design variable for design optimization.

  In this case, it is decided to use a number of project variables equal to the number of frequency errors to be minimized.

  The variables chosen are the thicknesses of the three parts of the section of the spar: side flanges, central web and the two vertical webs that compose the omega shape. Each thickness plays an important role

in terms of inertia of the spar, mass distribution and stiffness of the structure. Vertical webs for example affect the frequency of torsional modes, the thickness of the central web is closely related to the stiffness of the bending mode of the structure.

The nominal thickness of the plate elements is set as the initial guess of the card.

- DLINK: Relates one design variable to one or more other design variables.

  The properties that define the thickness of the central web of the spar are four. This is due to a different mass distributed per unit area along the wingspan which is expressed through the property of the central web element, making necessary to divide it into distinct properties while having the same structural features.

  In order to maintain the physics of the problem, an equality constraint between the thicknesses of the central web of the spar is employed in order to have constant thickness in wingspan. This constraint is expressed by the DLINK card.

- DVPREL1: Defines the relation between an analysis model property and design variables.

  In this card the previously described properties of the three spar parts are linked with the defined DESVAR.

- DVMREL2: Defines the relation between a material property and design variables with a user-supplied equation.

  Changing the thicknesses also changes the mass of the structure while keeping the density constant. This obviously is not allowed during the optimization phase. As an additional constraint,the mass of the global system must remain the same during SOL 200 computation. This is allowed thanks to the card in question.

  The card brings into play a fourth variable which is density. In reality it is a dependent variable as it is a function of the variation of the three independent ones (thicknesses of shell elements). The density is imposed constant along the spar in all its parts, thus recalling the physics of the problem. For the correct card setting it is necessary to define the density of all three spar parts, depending on an equation given via the DEQATN card.

  The eq.4.5 dictates variation of density as a function of independent variables.

$$\rho(t_1, t_2, t_3, c_1, c_2, c_3) = \frac{c_1}{t_1} + \frac{c_2}{t_2} + \frac{c_3}{t_3} \quad (4.5)$$

Where t_1, t_2 and t_3 are thicknesses of spar parts and c_1, c_2 and c_3 are constant coefficients which allow to link the changes in thickness to the total mass of the structure, in order to have it constant.

Example for the calculation of c_1 (similar for the other coefficients):

$$c_1 = \frac{V_{nom_1}}{V_{tot}} t_{nom_1} \rho_{nom}$$

Where:

 - V_{nom_1} is the volume relating to part 1 of the omega-shaped spar with nominal values

 - $V_{tot} = V_{nom_1} + V_{nom_2} + V_{nom_3}$ is the total volume in the nominal configuration

 - t_{nom_1} is the nominal thickness relating to part 1 of the omega-shaped spar

 - ρ_{nom} is the density in nominal configuration of the spar material.

From eq.4.5 the new density is calculated having changed the thickness but not the mass and it is weighed on the percentage of total volume that part had in the nominal configuration.

Hypothetical density of the part 1 keeping the same mass:

$$\rho_1 = \frac{\rho_{nom}}{t_1} t_{nom_1}$$

Volume fraction F_1 of the part 1:

$$F_1 = \frac{V_{nom_1}}{V_{tot}}$$

The contribution to the eq.4.5 due to the thickness variation of the part 1 is $F_1 \rho_1$.

The selection of a particular eigenvalue performing a normal modes analysis as a design response is done by specifying its mode number. The intent may be to design this particular mode number regardless of the physical nature

of the original mode shape. However, in many applications, the intent is to control a particular physical mode. In this case, the user's intent is actually to design the frequency of the physical mode shape but the mode number could vary due to the redesign. The eigenvalue analysis of SOL 200, includes a feature to 'track' the modes so that the modes are ordered based on their original physical behavior rather than on their frequency order. This is done by constructing cross-orthogonality check between the current design cycle and the previous cycle. This methodology is called *mode tracking.*
In this case, analysing only the three frequencies inherent to the flutter, it is easy to follow the modes. However, focusing on higher frequency modes, mode tracking has to be taken into account.

The design of the optimization is inspired by [15].
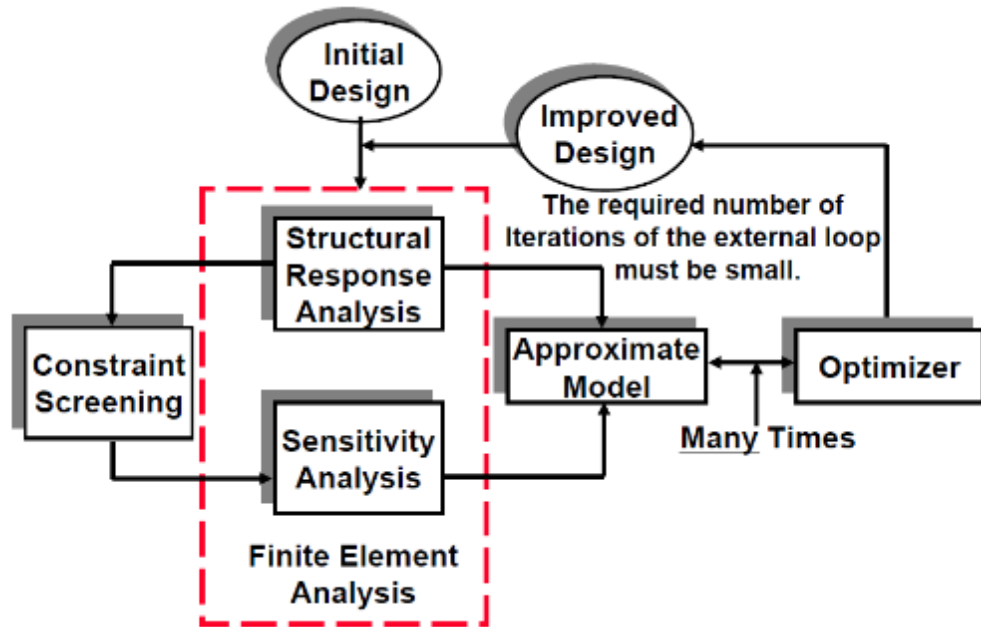
Figure 4.17: MSC/NASTRAN optimization process schematic diagram.

The default MSC/NASTRAN optimizer, used in the present work, is gradient-based [19].

4.3.3 Optimization Results

The nominal and post-optimization thicknesses are expressed in tab.4.8 with the percentage variation calculated with respect to the real thickness value, $\frac{t_{nom}-t_{opt}}{t_{nom}}$.

Omega Spar	Nominal [mm] thickness	Optimized [mm] thickness	Variation %
Upper web	3	2.6	13.33
Vertical web	3.4	4.0	17.65
Side flanges	3.4	4.0	17.65

Table 4.8: Optimization design variables.

In fig.4.2 the thicknesses are different from the nominal ones shown here, they are increased. This is done to take into account the increase in thickness in the corners and along the junction points.

Optimization converges after three iterations. The objective function passes from a value of $5.8 \cdot 10^{-2}$ to $8.8 \cdot 10^{-3}$, changing its initial value by almost an order of magnitude.

Natural Frequencies   The comparison between the pre and post optimization natural frequencies with those obtained through GVT is showed in tab.4.9. The frequencies under consideration are only those placed in the objective function. The optimized configuration is the one with mass in backwards position.

Mode type	GVT [Hz]	Pre - opt [Hz]	Post - opt [Hz]
1° bending	5.20	5.59	5.55
1° torsional	7.43	6.85	7.28
2° torsional	7.88	6.87	7.31

Table 4.9: Natural frequencies comparison.

In tab.4.10 the trend of errors before and after optimization and their comparison, $e_{pre} - e_{post}$.

Mode type	$\text{Error}_{\text{pre-opt}}\%$	$\text{Error}_{\text{post-opt}}\%$	Comparison
1° bending	7.5	6.7	0.8
1° torsional	7.8	2.0	5.8
2° torsional	12.8	7.2	5.6

Table 4.10: Error trend.

It must be said that, being the numerical model symmetric, the frequencies of the symmetric and anti-symmetric torsional are close; on the contrary the real model is not symmetrical and these two natural frequencies

are spaced as shown in the tab.4.9. In the objective function the frequencies to be reached are set equal to the values $f_{gvt1} = 5.2Hz$ $f_{gvt2} = 7.65Hz$ $f_{gvt3} = 7.65Hz$. So, the optimizer has the task of decreasing the natural frequency of the first bending mode and increasing the frequencies of the two torsional ones.

The reason why the frequencies f_{gvt2} and f_{gvt3} are not the same as those of the GVT, but at an average value between the two torsional frequencies calculated experimentally, is the desire to maintain the initial hypothesis of a symmetric model.

The changes made by the SOL 200 have thickened the lateral and vertical webs of the spar and decreased the thickness of the central one. It acts on the bending mode by lowering the natural frequency and thus decreasing the error about it. This occurs thanks to the decrease of thickness in the central web of the spar which mainly influences the bending frequency. On the other hand, the torsional is increased by acting on the mass distribution and on the plate elements which, in an omega section spar, contribute mostly to the torsional stiffness.

The mass distribution has changed by moving the mass from the central part to the two lateral ones of the spar. This increases the moment of inertia and therefore the torsional stiffness, which in turn increases its natural frequency. The plate elements which contribute mostly to the torsional natural frequency with their rigidity are the vertical part of the spar; the thicker they are, the more the torsional stiffness increases.

The last change made during the optimization falls on the value of the material density of spar, which passes from a value of 2717 Kg/m^3 in nominal configuration to 2697 Kg/m^3 in optimized configuration. The spar material is aluminum which leads to consider the density value reached acceptable.

Tab.4.11 contains the natural frequencies and the percentage errors with respect to the GVT of the modes which results to have a well correlated MAC. In the numbering of the modes the first 4 rigid modes are not taken into account, the first one is the bending.

In tab.4.11, in the mode number column, the first value corresponds to the numbering of the GVT and the second to the numbering according to the numerical solution.

Here a brief description of the features of the numerical and GVT modal shapes:

- 1-1 : Bending of the wing both for GVT and numerical solution.

- 5-5 : Tail movement plus pod twist.

Mode number	GVT [Hz] frequency	Post-opt [Hz] frequency	Error %
1-1	5.2	5.55	6.7
5-5	9.10	8.96	1.5
6-7	10.38	11.47	10.5
7-8	12.49	12.18	2.5
8-11	13.46	14.42	7.1
9-9	14.74	13.36	9.4
12-14	23.35	20.65	11.6

Table 4.11: Well correlated modes comparison after optimization.

- 6-7 : Symmetrical tail bending plus wing twist with a prevalence of pod movement.

- 7-8 : Bending of wing and orizontal tail.

- 8-11 : Bending of wing (light) and orizontal tail.

- 9-9 : Anti-symmetric bending of wing and orizontal tail.

- 12-14 : Torsional wing with slight contribution from orizontal tail.

MAC   For completeness, a MAC is calculated to compare the results obtained with the pre-optimization ones.
In the event of excessive worsening in modes already well correlated previously, the optimization carried out must be considered not optimal.
In fig.4.18 the MAC does not seem to have undergone excessive changes and the modes that had a high MAC value kept it, especially the 1° bending mode value remained untouched.

Flutter results post-optimization   The goal is to correctly capture the flutter behavior, but this type of optimization is carried out on modes at zero speed. When the aerodynamic forces come into play, the matrices of the system change according to the mach number and the reduced frequency.

To also include the contribution of a flutter analysis within SOL 200, optimizations are performed, with an ever-increasing variation range permitted to variables, interspersed with flutter analysis which gradually studied the actual flutter speed variation compared to that experimental calculated in the wind tunnel. The model that approaches closest to the real flutter speed is the one with the thicknesses presented above. Thus, the optimization is
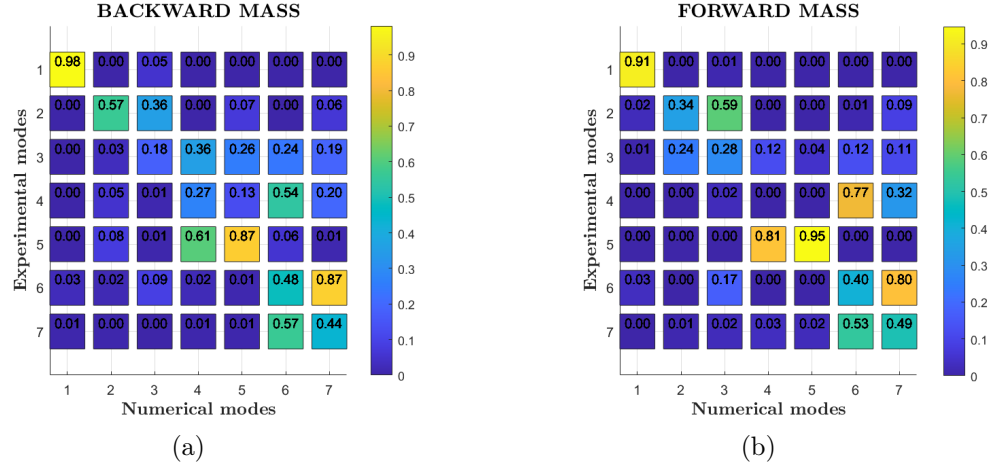
Figure 4.18: MAC in both configuration 1 and 2

not performed on the flutter parameters but on the modal analysis ones: the union of the two analysis, SOL 200 and SOL 145, leads to a complete analysis of the structural behavior, which reaches its fulfillment with the results in terms of flutter analysis presented below.

Remembering that the optimization is carried out only for the configuration with mass in backward position, the configuration with mass forward will help to determine if improvements impact on the entire model or are fictitious, acting only on a configuration and are not in globally sense.

In the V-g plot of fig.4.19b the intersection of the torsional mode with the zero damping axis occurs at a speed of $42m/s$, the speed for which the flutter instability is established in the mathematical model.
Flutter speed before and after optimization with percentage error and comparison of the instability limit:

- $V_{F_{tunnel}} = 41.5m/s$ wind tunnel tests flutter speed.

- $V_{F_{pre-opt}} = 32.5m/s$ flutter speed before optimization.

- $V_{F_{post-opt}} = 42m/s$ flutter speed after optimization.

- $E_{pre-opt} = \frac{V_{F_{tunnel}} - V_{F_{pre-opt}}}{V_{F_{tunnel}}} = 21.7\%$ error before optimization.

- $E_{post-opt} = \frac{V_{F_{tunnel}} - V_{F_{post-opt}}}{V_{F_{tunnel}}} = 1.2\%$ error after optimization.

- $E_{pre-opt} - E_{post-opt} = 20.5\%$ comparison between errors.
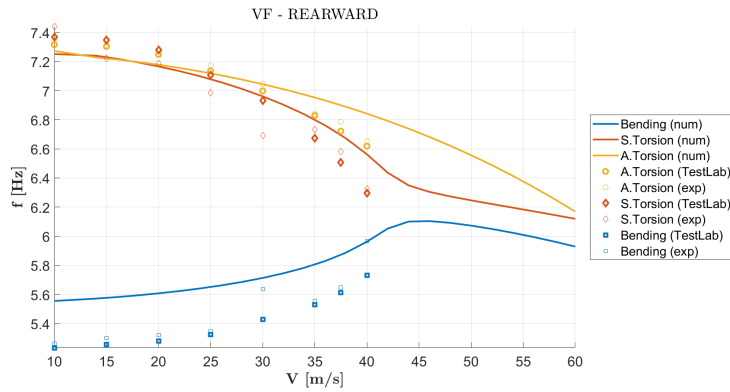
(a)
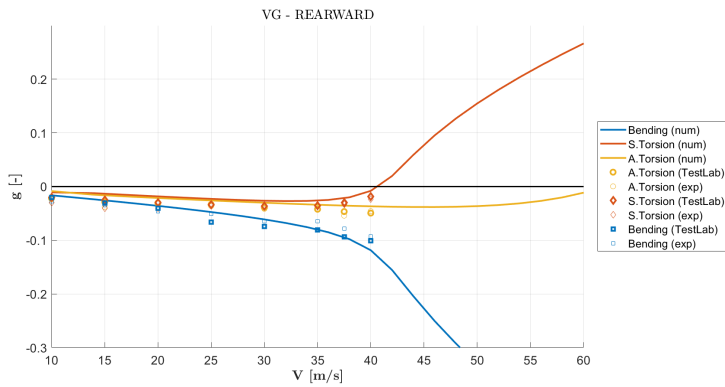
(b)

Figure 4.19: Flutter result in configuration with mass in backward position.

4.3.4 Sensitivity analysis

The optimization procedure is obviously not straightforward, may happen that various runs are needed to converge to an adequate error level. In fact, according to tab.4.10 the actual optimization stage is not sufficient to get an error under an acceptable threshold: in particular it is necessary to decrease the bending stiffness and, on the contrary, increase the torsional one.

Parameters   So another optimization step is required, acting more on the actual design variables or introducing new ones. The user's skill lies in detecting what parameters must be modified to decrease even more the error. The success in a modeling updating is significantly related to a smart parameter selection.
The following requirements are put forward as a general rule:

- the parameters should be selected in areas with modeling errors

- the objective function should be sensitive to the selected parameters

- it is good practice not to use a large number of parameters for optimization

Other settings of optimization analyses SOL 200 have been attempted from which useful information has been obtained on the behavior of the structure and on its sensitivity to the change of some parameters.

Two parameters are found capable of decoupling the two flutter modes:

Elastic modulus of the clamp It is the basis on which the wing structure is connected and has a relevant behavior in terms of modal shape and stiffness on all the elements connected to it.

In the analysis, its elastic modulus is allowed to vary from 72 GPa, the default value associated with aluminum, to a value of 45 GPa with a percentage variation of 37.5 %.

The results of a flutter analysis showed a downward shift in the V-f plot of the bending mode, leaving the two torsional ones almost unchanged.

Transverse shear thickness ratio Ts /T. Field of the PSHELL MSC/-NASTRAN card, is defined in [14] as the thickness resistant to transverse shear divided by the membrane thickness. This field has a default value of 0.8333 (for a homogeneous shell) and by acting on it, it is possible to increase the natural frequencies of the two torsional modes with minimal variations of the bending one.

The higher this value is and the greater is the shear-resistant area of the structure, leading consequently to a stiffening and so an increasing in frequency of the torsional modes.

MID3 A similar role is played by another parameter in the PSHELL card, called MID3. The plate element inherits the transverse shear stiffness from the material with ID specified in this field. Leaving it blank means to have an infinite stiffness along this direction.

So, on the basis of this research, tuning these parameter is a successful method to separate the bending behavior from the torsional one without affecting each other. A sensitivity analysis of the parameters is useful to identify the main role of each component.

After these study a new optimization process is run giving the possibility to the solver to work also on aforementioned parameters.

Another important aspect that makes necessary a further optimization stage is the need to consider also the aeroelastic behavior and so how the frequencies varies related to the velocities. So far the sensitivity analysis focused on the dynamics of the structure at zero velocity but an essential part of the work is based on aeroelastic phenomena. In this process the aerodynamic modeling of the pod fits: it has an massive impact on the overall aeroelastic behavior that so far has not taken into account. The system, and in particular the torsional participation, is very sensitive to its effect which lead in a changing of the slope of the torsional curves as the velocity (and so the aerodynamic contribution) progresses.

The new updating step aim to integrate also this aspect.

Implementation   Besides the already set thickness, extra design variable are introduced by means of DESVAR and DVPREL1:

- Young Modulus of the clamp, allowed to vary between (45; 72) GPa. This choice is addressed to decrease the bending frequency error.

- Young Modulus of the spar components, allowed to vary between (70; 72) GPa. This choice is addressed to decrease the frequency error.

Furthermore, outside the strict optimization setting, the model has undergone some modifications, such as:

- MID3 field of the PSHELL is set to be blank. This means to have an infinitely rigid in transverse direction plate, trying to increase the torsional stiffness of the wing.

- Introduction of the aerodynamics of the pod during the SOL145 following the SOL200 analysis, in order to see if the updated model is also able to catch this interaction

The post-optimization values of the mentioned variable are resumed in tab.4.12.

Omega Spar	Nominal [mm] thickness	Optimized [mm] thickness	Variation %
Upper web	3	2.6	13.33
Vertical web	3.4	4.0	17.65
Side flanges	3.4	3.8	11.76

Table 4.12: Optimization desing variables - 2nd run.

Mode type	GVT [Hz]	Optimization 1 [Hz]	Optimization 2 [Hz]
1° bending	5.20	5.55	5.27
1° torsional	7.43	7.28	7.42
2° torsional	7.88	7.31	7.47

Table 4.13: Natural frequencies comparison - 2nd run.

Modal analysis results The variation of the design variables considered produces the following frequency error, tab.4.13

Producing an error of:

Mode type	$\text{Error}_{opt1}\%$	$\text{Error}_{opt2}\%$	Comparison
1° bending	6.7	1.34	5.36
1° torsional	2.0	0.13	1,87
2° torsional	7.2	5.2	2.0

Table 4.14: Error trend - 2nd run.

From tab.4.13 and fig.4.14 it is possible to appreciate how significant are the results. Especially on the first bending and torsional modes, the error gets values lower than 1%, showing an important reduction.
The results produced highlight the excessive rigidity with which the clamp was modeled, it clearly present some internal compliance. On the other hand, plate elements are actually stiffer than the previous modeling.

The modal shapes instead are modified according to the MAC of fig.4.20, showing improvement as well.

Flutter analysis results The final V-f plot in fig.4.19a of the flutter after the first optimization seems to follow the trend (slope) of the experimental points for the bending mode but is upward shifted.

In the graphs V-g and V-f shown below in fig.4.22, with the last changes made on the sensitivity parameters found, the mentioned shift is completely cancelled.

The final model has a Young modulus of the wing-fuselage attachment of 45 GPa instead of the initial 72 GPa. Change that guides the bending curve to follow the experimental one in the V-f graph.The curve of the torsional mode assumes a slope more in line with the experimental data once the aerodynamics of the pod has been added. The introduction of this essential feature in the model leads to a rapid drop in the flutter speed which recovers its initial characteristics in the absence of the MID3 parameter in the PSHELL card.
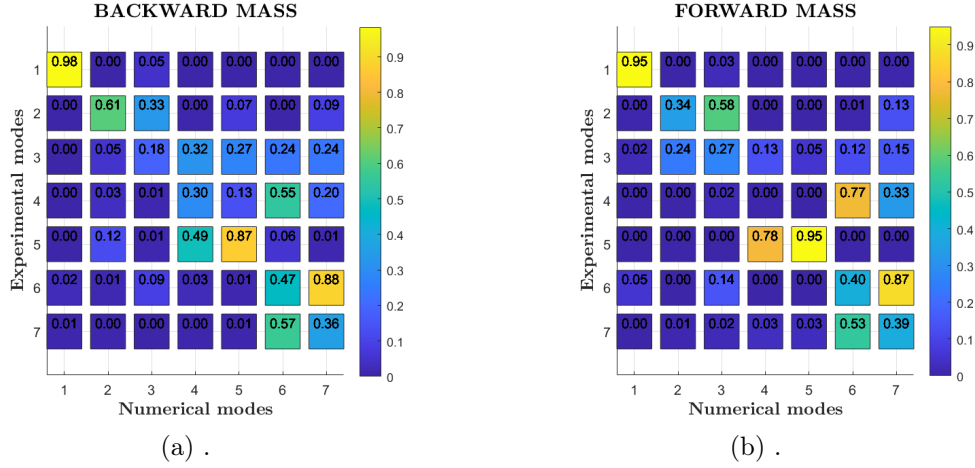
Figure 4.20: MAC of the final optimization

- $V_{F_{tunnel}} = 41.5 m/s$ wind tunnel tests flutter speed.

- $V_{F_{post-opt}} = 40.5 m/s$ flutter speed after optimization.

- $E_{post-opt} = \frac{V_{F_{tunnel}} - V_{F_{post-opt}}}{V_{F_{tunnel}}} = 2.4\%$ error after optimization.

For completeness, in fig.4.21 there is the comparison also for the forward mass configuration. This is a proof of the goodness of the results since all the procedure is based on the backward mass configuration, producing anyway indirectly improvements on the forward one.

Summary The correlation process described in this chapter follows many steps and model changes in its course. A summary scheme is needed to understand the procedure and to observe the modus operandi. In fig.4.23 is shown a summary scheme.

The comparison is carried out always in the same manner: CROSS-MAC and frequency error between experimental and numerical model, followed by a check on the trend of the graphs V-g and V-f to find out if anomalies arose during the changes brought on FEM model.

The scheme of fig.4.23 illustrates the transition from 4 models before reaching the final MSC/NASTRAN model:

1. Stick model: the initial and the simplest model.
   Problems: error on the flutter speed, too high; V-g and V-f charts with different trends compared to the experimental ones in forward mass
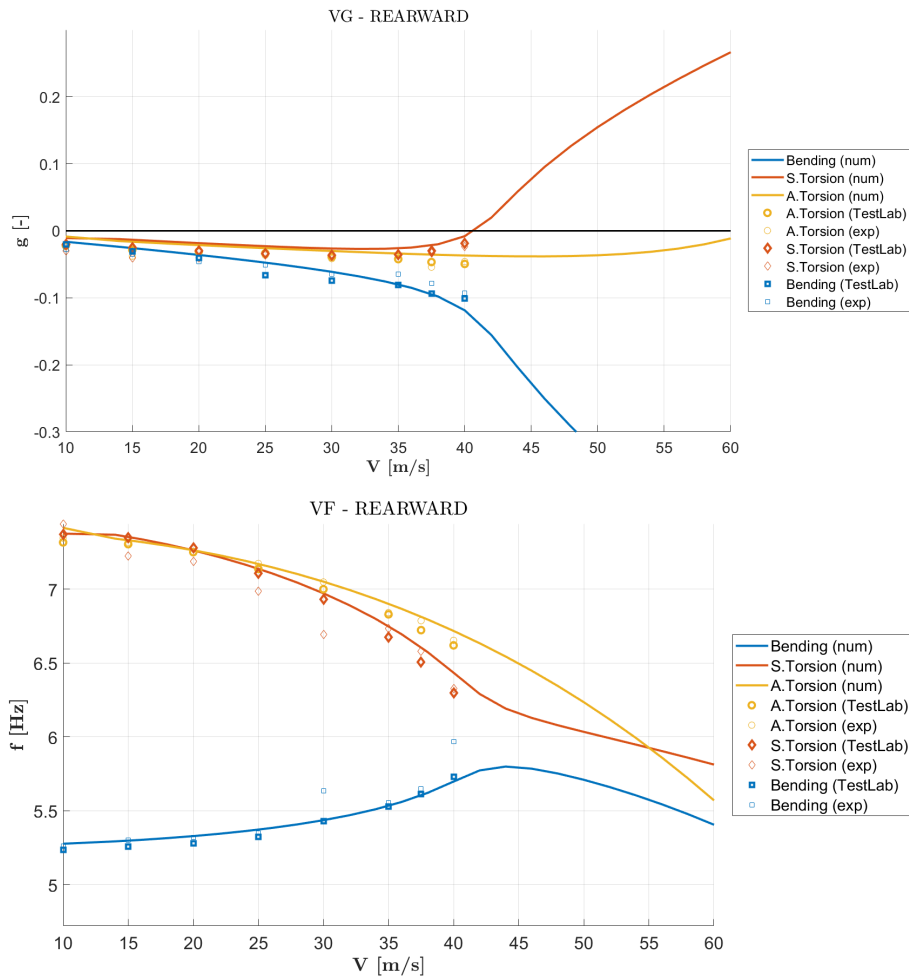
Figure 4.21: Flutter numerical vs experimental results (final updating) - backward mass.

configuration; above all the flutter analysis is strongly dependent on the number of modes chosen for the numerical calculation, strange and unacceptable behavior.

2. Plate model: detail model for the main component under analysis, the wing.
   Problems: the error on the natural frequencies on the first and main flutter modes is unacceptable (7.5% and 7.8%) as well as flutter speed is still too high (21.7%). The phenomenon is not picked up correctly.

3. 1st updated plate model: optimized using the thicknesses of the spar as variables.
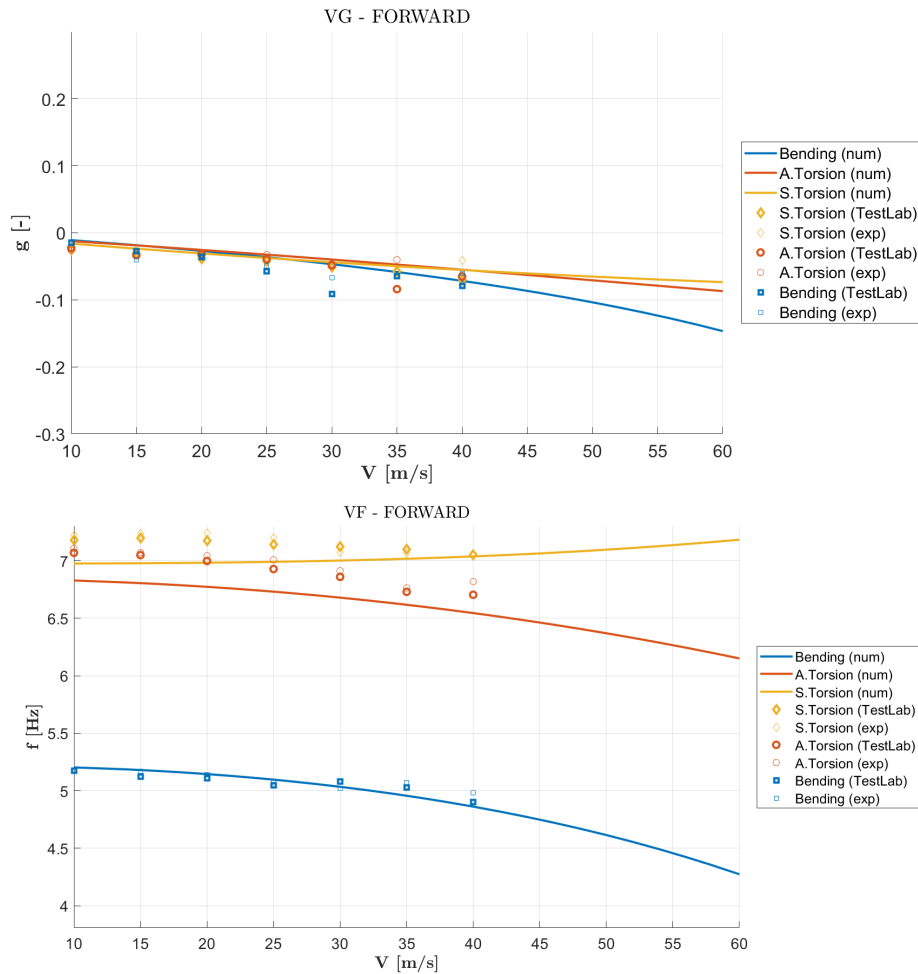
Figure 4.22: Flutter numerical vs experimental results (final updating process) - forward mass.

Problems: the error on the flutter velocity would be acceptable but the errors of the frequencies of the modes under examination at speed 0 m/s are still high and the V-f graph shows an evident shift in frequency as the speed increases.

4. 2nd updated plate model: the variables to be inserted in the SOL200 are increased. This leads to the final model abel to consider also the aerodynamics of the pod, with errors on the natural frequencies in line with those desired, and trends in the V-f and V-g plots optimal for both forward and backward mass configuration.

The last FEM model, product of the 2nd optimization run is the one with
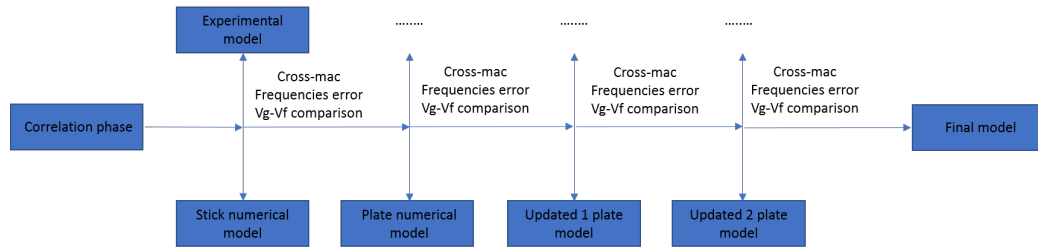
Figure 4.23: Summary scheme of the chapter.

the best results in terms of modal parameters and flutter behavior, and since the rest of the work is centered on AFS system design it figure as solid basis for next activity. Unfortunately the schedule of the experimental activities, as so often happens, did not allow to set up completely the mathematical model until its last version. From now on, the FEM model used is not the last produced with the best result, but the one that arises from the 1st optimization run described in sec.4.3.3. Future works may be developed starting from the more accurate version of it.

Chapter 5

Control Systems

The existing technologies and current state of the art see Active Flutter Suppression (AFS) as the main solution to this kind of instability [9]. Nowadays, the scientific development pushes for increasingly lightweight aircraft. Such weight reduction necessarily entails the drawback of having growing structural flexibility and hence potential flutter problems. This factor, combined with reliability of aircraft control system hardware and software, leads to rely widely on active control strategy to face the aeroelastic instability phenomena. Thus it results to be an important contributor to the effective solution of this kind of problems both in forward stage of the development of a new aircraft and from the start of the design process.

Substantially, it is a key element in multidisciplinary design optimization that could lead to more efficient aircraft. This is the framework in which the X-DIA project fits and it is the subject of research and implementation of several control strategies. The main scope of this research activity is the validation of flutter control technologies and the investigation of the impact of uncertainties on their performances.

5.1 Model setting

For this phase is necessary to work on an state space representation of the aeroelastic numerical model, that therefore it is used both for design and simulation of the active control system. The state space model produced describes only the configuration with pod mass placed backward since the controller has to act where the flutter is present.

So, starting from the optimized FEM model seen in the previous chapter, a conversion procedure is applied. In order to extract the modal matrices from MSC/NASTRAN, a Direct Matrix Abstract Program (DMAP) state-

ment is used. DMAP is a symbolic, macro-like programming language used to control the way in which problems are solved in the MSC/NASTRAN finite element solver. Running both modal and flutter analysis with free surfaces, it is possible to extract:

M_{hh} : Modal mass matrix, unitary diagonal matrix since the eigenvector scaling is perfomed with the unitary mass procedure.

C_{hh} : Modal damping matrix, null because no structural damping elements are introduced in the model.

K_{hh} : Modal stiffness matrix, diagonal matrix containing the stiffness associated to the respective mode.

Q_{hh} : Generalized aerodynamic matrix, it is a complex valued matrix representing the aerodynamic transfer function between modal coordinate and aerodynamic forces. It is know only in correspondence of a discrete set of reduced frequency k and Mach number of the airflow M_∞.

These are the matrices that compose the aeroelastic modal system in frequency domain:

$$\left[s^2 M_{hh} + s C_{hh} + K_{hh} - \frac{1}{2}\rho V^2 Q_{hh}(k, M_\infty) \right] q(s) = P(s) \qquad (5.1)$$

This is the most widely used form to express the dynamics of an aeroelastic system, a non rational frequency domain representation. For control purposes, and in particular for modern approach, a state space formulation in time domain of the aeroelastic problem is required since it is more suitable to achieve performance claims through the implementation of such theories. In order to implement the control strategies explained in sec.5.2, the aeroelastic system of eq.5.1 has to be converted to the form of eq.5.2, using state space formulation.

$$\begin{cases} \dot{x} = Ax + Bu \\ y = Cx + Du \end{cases} \qquad (5.2)$$

The state matrices illustrated in eq.5.2 are generated using NeoCASS (`www.neocass.org`).
Next generation Conceptual Aero Structural Sizing (NeoCASS) [2] is an open source suite of `Matlab` modules that combines state of the art computational, analytical and semi-empirical methods to tackle all the aspects of the aero-structural analysis of a design layout at conceptual design stage.

Once the MSC/NASTRAN finite element model is turned into a state space representation it is possible to build a reduced order of it, prone to the controller design.

The reduced order model is composed by the first 20 modes: the first 2 are rigid modes relative to the free motion of the control surfaces and the remaining 18 are the four rigid modes due to cables constraints and the first 14 deformable modes. In addition to these, two other states are added in order to model also the dynamic of the actuators driving the control surfaces, through a second order system with transfer function expressed in eq.6.1, later presented. This relation links the 2 deflections δ (left and right aileron) to the 2 commands δ_c of the servo-controller. This equation is the interface element between the structure and the controller, closing so the feedback loop. Once translated in time domain, effective commands δ are added to the system equations, for a total of 22 second order differential equations.

The final state vector is composed by 44 variables since a second order equation, representing the dynamic behavior of the structure, can be seen as a system of two first order differential equations.

5.2 Control strategies

Each university involved in this project has implemented its own AFS controller according to the preliminary agreements. There are three types of controllers developed during the project and they have all been tested inside the wind tunnel of the Politecnico di Milano university:

ILAF Identical Location of Acceleration and Forces.
In summary: integrating structural acceleration in one point, the ILAF system works to create a force in direction opposite with respect to the structural velocity at the same point. This force being opposite to the speed create a damper for the structure.

Key points:

1. Identical location of accelerometer and force
2. Approximate integration of acceleration to obtain velocity signal

This controller is designed by University of Washington, Seattle.

LQG Linear–quadratic–Gaussian control.
Time domain control theory, based on optimal strategy. An LQG controller is a combination of a Linear Quadratic Estimator (LQE) to-

gether with a Linear Quadratic Regulator (LQR). The LQE is a Kalman filter.

This controller is the product of the collaboration between the Aeroespace Engineering Department (DAER) of Politecnico di Milano and University of Washington, Seattle.

SOF Static Output Feedback.
Time domain control theory, based on optimal strategy. The control input $\boldsymbol{u}$ is linearly proportional to the measurements $\boldsymbol{y}$, providing so a direct control gain matrix, without introducing any delays (no undesired dynamics are involved, static controller).

This controller is designed by DAER of Politecnico di Milano.

Specifically, the three type of controller are discussed below:

ILAF The method of identically located accelerometers and forces is an elastic mode control system, known as 'physics-based approach'. The objective of the study is to design a simple, stable system to maintain system stability and to provide damping to the structural modes. So, the concept of the ILAF system is a structural mode damper [11]. In fact this kind of control law assumes that the aileron has a steady action on the system and hence its aerodynamics does not introduce any delays. That is, the controller reacts immediately to structural variations.
For this reason, briefly stated, the design synthesis locates the structural motion sensor (accelerometer) as close as possible to the force generator (aileron), following the idea of co-located control. In general, the ILAF system is more effective at supersonic than subsonic flight conditions because the aerodynamic forces generated by control surface deflections in supersonic flight are concentrated at the control surfaces, enforcing the co-location .
A simplified illustration of the key ideas involved in the ILAF system technique is displayed in fig.5.1.
The generalized control force is a measure of controllability of a particular structural mode. This force is the product of the normalized natural vibration mode shape $\phi_i{}^F$ at the force application point and the force magnitude F, better known as generalized force component. The structural acceleration at a given point is the product of the normalized mode shape $\phi_i{}^A$ in that point and the generalized coordinate acceleration $\ddot{\eta}^A$. For the control system stability, the polarity of $\phi_i{}^A$ and $\phi_i{}^F$ must always be the same. One way of insuring this requirement is to place the sensing element (accelerometer) at the force application point.
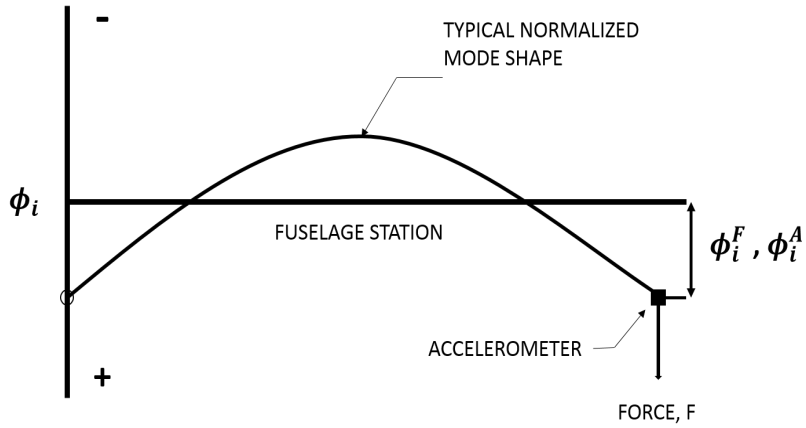
Figure 5.1: Application of ILAF features on a mode shape.

The second key idea in the ILAF system is the use of approximate integration of the accelerometer signal to obtain the required velocity measure to activate the damping force like in fig.5.2.
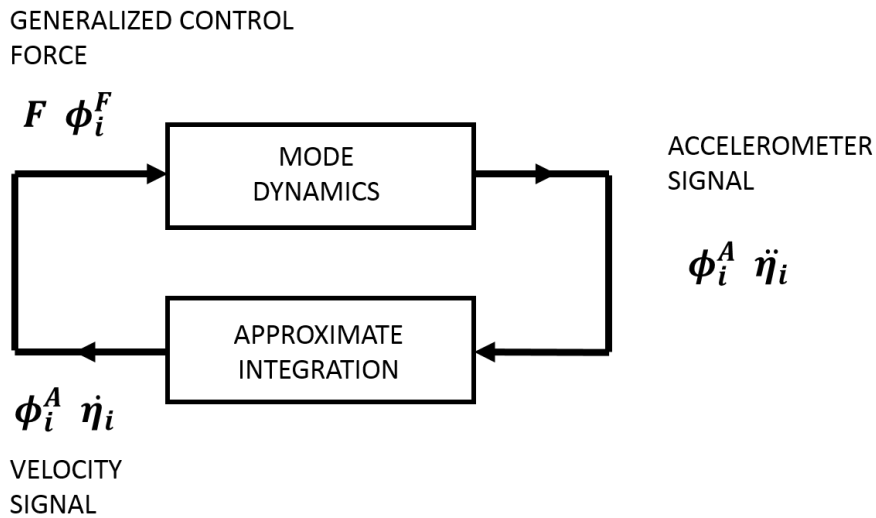
Figure 5.2: ILAF block scheme.

LQG It concerns linear systems driven by additive white Gaussian noise. The problem is to determine an output feedback law that is optimal in minimizing the expected value of a quadratic cost criterion [8]. As already mentioned, this type of controller puts together a linear quadratic estimator and

regulator, with their main features:

- LQE: an algorithm that uses a series of measurements observed over time, containing statistical noise and other inaccuracies, and produces estimates of unknown variables that tend to be more accurate than those based on a single measurement alone, by estimating a joint probability distribution over the variables for each time-frame. The algorithm works in a two-step process: in the prediction step, the Kalman filter produces estimates of the current state variables, along with their uncertainties; once the outcome of the next measurement (necessarily corrupted with some amount of error, including random noise) is observed, these estimates are updated using a weighted average, with more weight being given to estimates with higher certainty. The algorithm is recursive. It can run in real time, using only the present input measurements, the previously calculated state and its uncertainty matrix; no additional past information is required.

- LQR: The theory of optimal control is concerned with operating a dynamic system at minimum cost. The case where the system dynamics are described by a set of linear differential equations and the cost is described by a quadratic function is called LQ problem. The settings of a (regulating) controller are found by using a mathematical algorithm that minimizes a cost function with weighting factors supplied by the user. The cost function is often defined as a sum of the deviations of key measurements from their desired values. Controller construction will be an iterative process in which the engineer judges the 'optimal' controllers produced through simulation and then adjusts the parameters to produce a controller more consistent with design goals. The LQR algorithm is essentially an automated way of finding an appropriate state-feedback controller. The algorithm permits to determine the feedback gains.

The state estimator and the state feedback can be designed independently thanks to the separation principle.

System to be controlled, described as completely as possible, is in eq.5.3:

$$\begin{cases} \dot{\boldsymbol{x}} = \boldsymbol{A}\boldsymbol{x} + \boldsymbol{B}_u\boldsymbol{u} + \boldsymbol{B}_d\boldsymbol{d} \\ \boldsymbol{y} = \boldsymbol{C}_y\boldsymbol{x} + \boldsymbol{D}_{yu}\boldsymbol{u} + \boldsymbol{D}_{yd}\boldsymbol{d} + \boldsymbol{D}_{yr}\boldsymbol{r} \end{cases} \tag{5.3}$$

Where $\boldsymbol{x}$ is the state, $\boldsymbol{u}$ are the (controllable) inputs, $\boldsymbol{d}$ are the (uncontrollable, often even unmeasurable) disturbances, $\boldsymbol{y}$ is the output (in the sense of the sensor measures), $\boldsymbol{r}$ is the measurement error.

Direct state feedback (under the assumption that the state $\boldsymbol{x}$ is known):

$$\boldsymbol{u} = -\boldsymbol{Gx}$$

where G is a suitable gain matrix.

The objective is to determine G such that the closed loop system has the desired properties in terms of stability and performance.

In the case under exam instead of seeking a gain matrix to achieve specified closed-loop pole locations (classical approach of frequency-based algorithms), it is searching for a gain to minimize a specified performance criterion V (or *cost function*) expressed as the integral of a quadratic form in the state $\boldsymbol{x}$ plus a second quadratic form in the control $\boldsymbol{u}$:

$$V = \int_t^T \left[\boldsymbol{x}'(\tau)\boldsymbol{Q}(\tau)\boldsymbol{x}(\tau) + \boldsymbol{u}'(\tau)\boldsymbol{R}\boldsymbol{u}(\tau) \right] d\tau \tag{5.4}$$

where Q and R are symmetric matrices.

The limits on the integral: the lower limit t is identified as the present time, and the upper limit T is the terminal time, or final time. The time difference $T\check{}t$ is the control interval, or "time-to-go."

Once the problem is set, the goal is to find optimum gain matrix $\boldsymbol{G}$, by means of ARE (*Algebraic Riccati Equations*) [8].

SOF It is based on linear optimum control and consist in a Direct Measure Feedback control, where the feedback control input $\boldsymbol{u}$ is obtained from the available measurements $\boldsymbol{y}$, known directly from sensors installed on the structure.

This means to have control input vector in the form of eq.5.5, recalling eq.5.3 and neglecting the contribution of disturbances.

$$\boldsymbol{u} = -\boldsymbol{Gy} = -\boldsymbol{GC}_y\boldsymbol{x} \tag{5.5}$$

Thereby the knowledge of the states $\boldsymbol{x}$ is no longer necessary and so no observer is needed, resulting on a much simpler controller.

Anyway, extracting only a part of the states leads to some drawbacks. Performances can be significant limited, also using the same performance indicators and weight matrices, since this approach can rely on less parameter to get the minimum solution of the cost function.

For this reason this type of control is said to be *sub-optimal*.

However, its main disadvantage lies in the impossibility to obtain a Riccati equation by minimizing the cost function. Hence this results in handling a big numerical optimization problem in which it is necessary to minimize a complex expression depending implicitly on $\boldsymbol{G}$.

The strategy adopted to minimize the objective function applies a second order approximation on it computing its Hessian matrix and then finding the stationary solution through a simple Levenberg–Marquardt modified Newton–Raphson iteration, as implemented in [5].

The unknowns of the cost function are simply the element of the gain matrix. The dimension of the gain matrix depends on the choice of the quantities acquired through the measurement. To guarantee the best possible performances is strongly dependent on the type of output provided to the controller: the guideline is to select the quantities that permits to best describe the structural behavior. So the type of sensors and their positioning is aimed to enrich the knowledge of the structural motions.

So, the unknowns vector can be extended to include any system parameter available for optimization and this is the point that may be expressed as the great SOF advantage: a proper choice of the sensor locations and measures provided can produce excellent results in front of a simple control structure.

Chapter 6

AFS Wind Tunnel Tests

The following chapter completes the wind tunnel tests introduced before in chap.3. With the first test campaign the step was to identify the flutter point and its mechanism. The second step, once the flutter and the dynamic behavior of the modes connected to it have been identified, will take over all the tests useful for testing and validating the developed controllers.

The following pages contains a detailed description of this process and of the tests conducted in the January 2020 session.

6.1 Test setting

The assessment of the capacities of the AFS controls has to pass necessarily to validation process. The study of aeroservoelasticity is performed using both experimental and theoretical abilities, which should be strictly connected. So, the substantiation of the overall aeroservoelastic system follows the same steps covered in the previous chapter. Firstly a numerical analysis of the phenomenon: the application of the control law on the analytical model and simulation of the dynamic response of the aircraft. Secondly, extract suitable data to make a comparison with experimental measurements acquired during a further wind tunnel test session, in which the controller is applied to the real X-DIA model. Finally, verify the actual effectiveness of AFS system.

As regard the numerical simulation, the software used is `Matlab`, in particular the Simulink Graphical User Interface (GUI) environment, very suited for modeling, simulating and analyzing multidomain dynamical systems. This choice is dictated by the possibility to reproduce the measurement chain and obtain an high level of accuracy.

The model used for the simulation is the same Reduced Order Model (ROM) on which the controller design relied.

6.1.1   Excitation system

As previously discussed in sec.3.1.2 for excitation methods, there are several choices to employ. Among all, the sweep and the white noise command are selected, with a particular preference for the latter. Both are able to excite the frequency of interest, with various amplitude to guarantee the proper energy level transmitted to the structure, but the sweep signal exhibits problems in the correction reconstruction of the frequency response since the time spent on a single harmonic is very low.

(a) Sweep command features   (b) White Noise features.
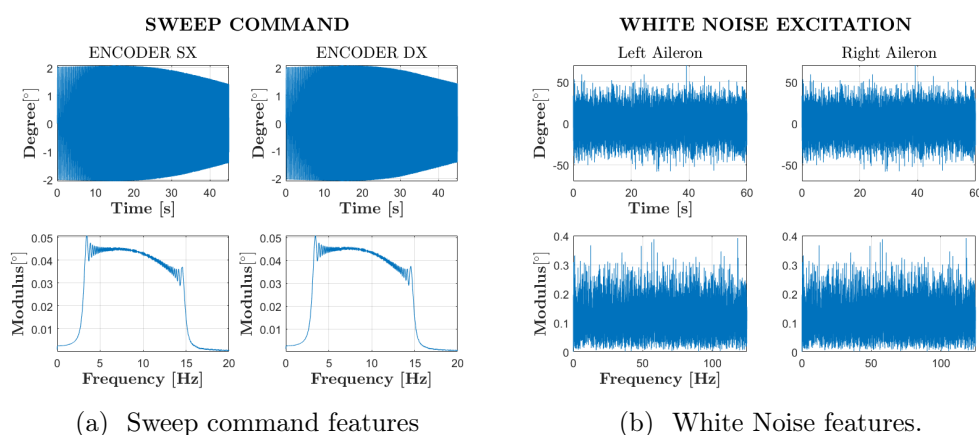
Figure 6.1: Excitation commands: time histories and PSD.

Theoretically, continuous white noise has a correlation time of 0, a flat PSD, and a total energy of infinity. In practice, physical systems are never disturbed by white noise. So the actually signal given as input is a so called *band-limited noise* consisting in a normally distributed random numbers.

In order to reach an high level of fidelity between experimental and numerical results it is decided to run the numerical simulation giving as excitation term the time history of the of input command extracted from experimental tests. In this way the numerical and real aircraft receive the identical entry.

During session test, nevertheless, errors occurred in the command feed and all data saved in the channel corresponding to the excitation measured are corrupted. In fact, as it is possible to see from fig.6.1b the command that should be provided to the aileron requests a value of 50 degrees, that is a not feasible amount. From there the decision to supply as forcing term the difference between the encoder reading and the command requested from servo-controller. Indeed the encoder measures the effective rotation of the control surface, result of the superposition of the input term and the controller action.

The resulting signal is showed in fig.6.2 and highlights as it is not a perfect white noise, but presents a marked amount of energy around the flutter harmonic and poor excitation for frequency higher than it. It should be due to all the compliance introduced in the kinematic chain from the electric motor until the sensor and its interaction with other systems.
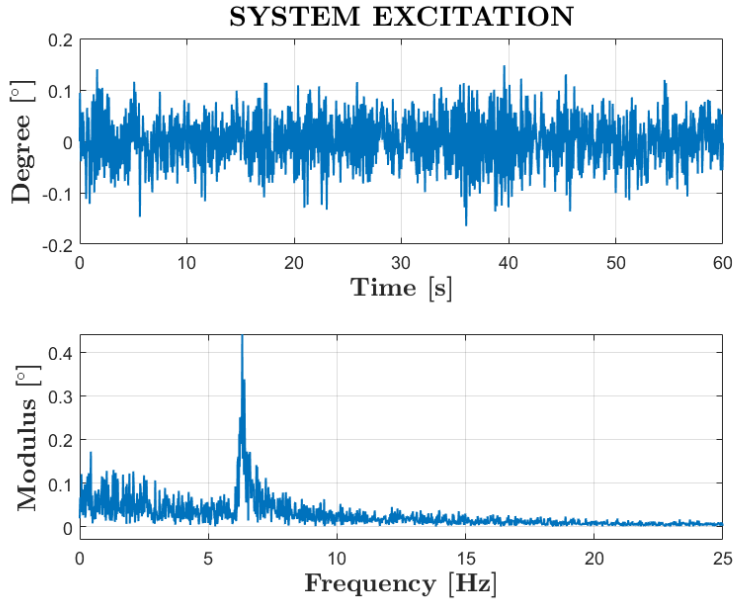
Figure 6.2: Resultant excitation signal.

6.1.2   Block diagram introduction

During tests three controller are processed. The Simulink representation is very simple and will be described for the only two control laws analysed in this work: SOF and LQG.

During the tests session many different SOF realizations are carried out, two of these are briefly described:

- Based on four outputs Leading Edge (LE) and Trailing Edge (TE) tip accelerations from which the local velocities and displacements are numerically computed by means of dedicated pseudo-integrator. The block scheme is in fig.6.3.

- With the idea of co-locating as much as possible the measures, the sensors outputs surrounding the aileron are taken and supplied to the controller. Eight acceleration are acquired (four per side), integrated

to obtain velocity measures and with them providing an input able
to restore the lack of damping typical of flutter condition, since the
damping phenomena are proportional to the velocities.

The block scheme in fig.6.3 is an example of representation in Simulink of
the only part of blocks belonging to the SOF controller. A double integrator
obtains speed and displacements from the accelerometers in LE. A set of
eight measures, containing accelerations, speeds and displacements, are given
as feedback through the gain matrix calculated with the SOF methodology.
Finally there is the possibility to insert a delay in the feedback system through
the last block highlighted in light blue in the fig.6.3. The output is the action
of the controller on the excitation input.
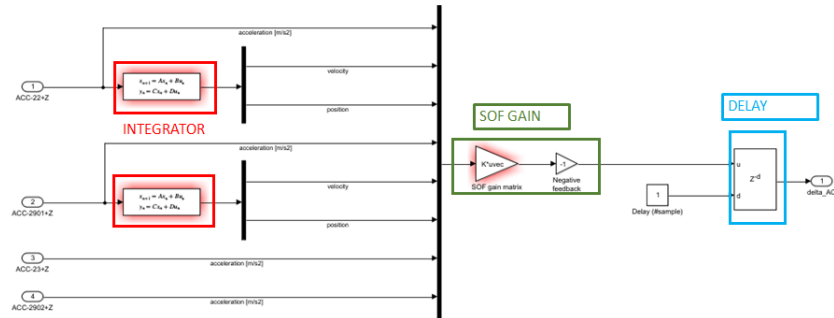
Figure 6.3: SOF controller scheme.

Similarly, the scheme for an LQG controller is constructed. In figure 6.4
the feedback takes place directly on the accelerometric measurements of the
four accelerometers indicated. They see the action of the LQG by switch-
ing from a Kalman filter (LQE) and being multiplied by the gain matrix
calculated by means of an LQR.
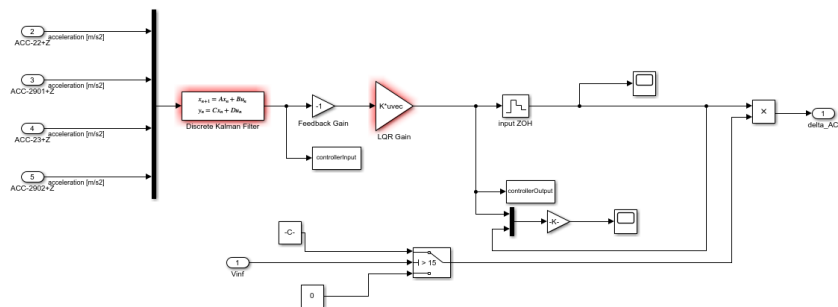
Figure 6.4: LQG controller scheme.

A switch has to be inserted to regulate the controller activation. It is commanded in velocity with a threshold value of 15 m/s. After that, the loop is closed.

Simulink GUI comprises some block diagrams to assist the analysis. Among those:

- Motor transfer function

- Washout filter

- Accelerometer transfer function

- Integrator

Motor transfer function   The aileron is used as a tool to energize the system.

Its transfer function is an index of its ability to introduce energy into the system in the frequency spectrum under analysis. The type of excitation desired in the tunnel tests is a symmetric one, capable of giving more energy to the modes that are subjected to instability. For this reason the actuation system must allow both symmetric and anti-symmetric displacements. To do this, two motors are placed to control the surfaces, one on the right and one on the left.

The model of the actuation system is known and included in the states as discussed before (sec.5.1). It can be identified by a second order transfer function of the form:

$$\delta(s) = \frac{\omega_0^2}{s^2 + 2\xi\omega_0 s + \omega_0^2}\delta_c - \frac{M_h(s)}{K_\delta} \tag{6.1}$$

Where M_δ is the relative hinge moment, K_δ is the motor stiffness 200 (Nm/rad), δ_c is desired command deflection and δ is effective command.
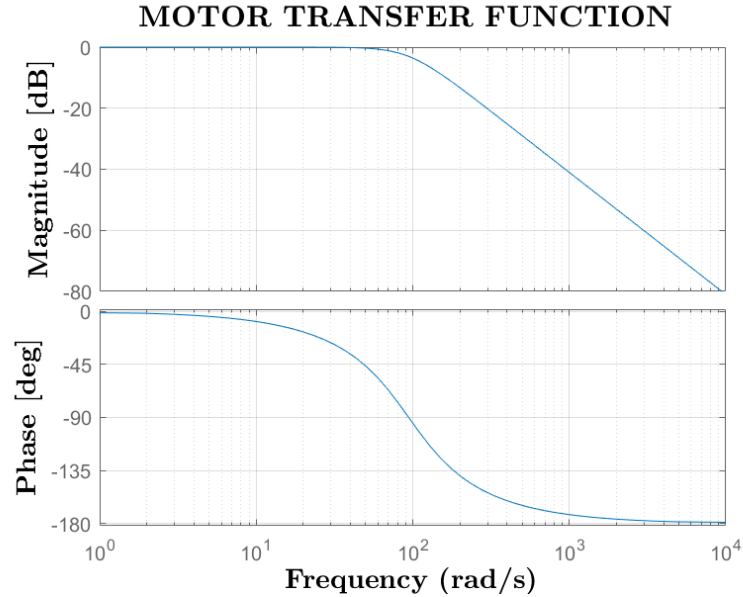
Figure 6.5: Motor transfer function bode.

Its transfer function acts as a 2nd order Butterworth filter, with bandwidth of 15 (Hz), $\omega_0 = 2\pi \cdot 15$ (rad/s) and $\xi = 0.707$.

Washout filter Accelerometers and integrators transfer functions can be chosen to improve performances of the closed loop system, thus they are design parameters of the controller together with the gain matrix.
A washout filter, which will function essentially as an high pass filter, is inserted in the feedback branch of the system reproduced in Simulink in order not to allow the controller system to impact on the low frequencies of the system, avoiding to excite rigid modes of the wing tunnel model.

$$a_{filtered} = \frac{s}{s + 2\pi \cdot 0.5 Hz} a \qquad (6.2)$$

The filter cuts and phase lag below 0.5 Hz, at frequencies of interest the signal should remains in phase. Since the lowest deformable mode is at a frequency of about 5.2 Hz, the loss of performances coming from a pole at 0.5 Hz should not be excessive. In fig.6.2 the bode diagram.
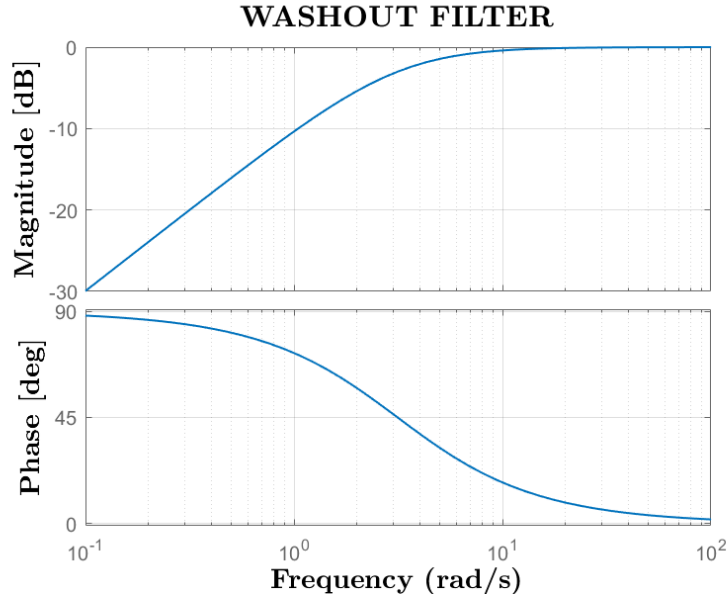
Figure 6.6: Washout transfer function bode.

Accelerometer transfer function   The accelerometers transfer function can be listed as a second order equation and relates the true acceleration of the model (in this case only along z direction) and measured acceleration.

$$a_{measured} = \frac{\omega_0{}^2}{s^2 + 2\xi\omega_0 s + \omega_0{}^2} a \qquad (6.3)$$

Eq.6.3 serves also as a low pass filter that reduces the bandwidth of the filter and thus a lower sampling frequency is required in order to avoid aliasing problems. The cut-off frequency is $f_0 = \omega_0/2\pi = 50 Hz$, damping used is $\xi = 1$.
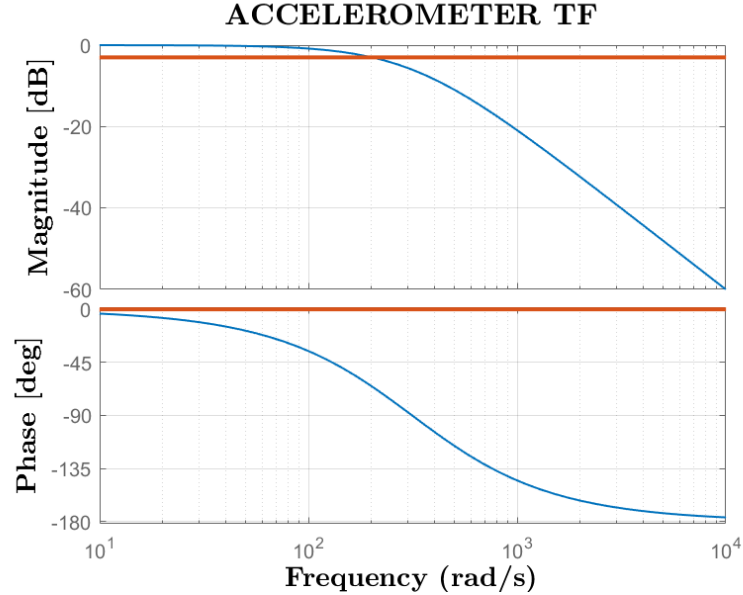
Figure 6.7: Accelerometers transfer function bode.

Integrator An integration is needed from the measured acceleration in order to obtain velocities and, in some cases also displacements. The choice depends on the type of controller in use.

The simplest integrator has transfer function $1/s$ and bode diagram of fig.6.8.

In this case in the model is inserted a pseudo-integrator with the purpose of having zero gain at zero frequency to reject constant drifts. The bode diagram of pseudo-integrator is in figure 6.9. The equation is in eq.6.4.

$$y_{speed} = \frac{s}{\mu \left(s^2 + 2\xi\omega_0 s + \omega_0{}^2\right)} u_{acc} \tag{6.4}$$

Where $\mu = 1000$ makes the plot start from -60 dB, two poles and a zero at $\omega = 1$ $(f = 0.16 Hz)$.

6.2 Wind tunnel tests

The tunnel tests are the final and main step to verify the effects of the application of the controller on the state model generated starting from the MSC/NASTRAN one. They also prove the reliability of the mathematical model.
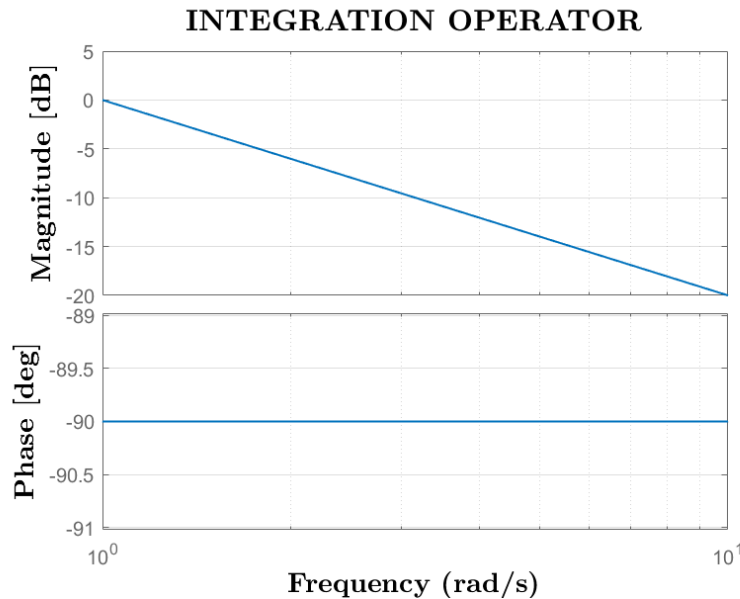
Figure 6.8: Integrator bode diagram.

The test session lasted a week, from 27/01/2020 to 02/02/2020, with representatives from different countries who came to observe the possibility of controlling a destructive aeronautical event in the test chamber.

The model is placed in the gallery reproducing the same free-free constraint used for the GVT tests (sec.3.1.1), in order to keep faithful to the previously studied model.

The checks necessary for the success of the test session are carried out: acquisition systems, accelerometric channels and anti-flutter device operation, etc.

In this phase of the tests, the anti-flutter device is essential for their success and for the safeguard of the model: for most tests the model is in unstable conditions and without a safety device the control system is the only in charge of the model integrity, whose functionality must be tested. The activation of the safety system occurs when the accelerometers read a value of 4 g, considered as the limit value for the entirety of the model. The mass inside the pod snaps forward and the new mass configuration keeps the modes prone to flutter separate, avoiding to flutter phenomenon to arise at the speeds in question.

Once the necessary checks have been made, tunnel tests can be started at ever higher speeds.

The tested controllers are those of the type previously presented: LQG,
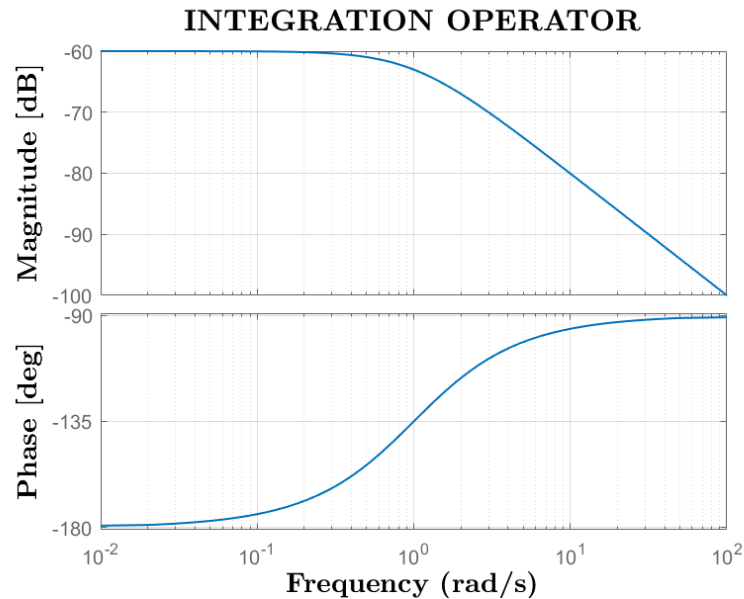
Figure 6.9: Pseudo-integrator bode diagram..

ILAF, SOF.

At the basis of the way to conduct the wind tunnel tests there is the main aim of the project: building an AFS system and make a sensitivity and robustness analysis on the closed loop system. Thus, different types of tests are carried out, every one with increasing velocity with the aim to highlight the trend of the structure and check how the system approach to flutter condition. During the increasing velocity steps, the same closed-loop configuration is kept. For robustness aspects, starting from the original design scheme, some parameters are changed, such as gain percentage and phase shift, in order to estimate how control law performances changes.
Tests of this type are carried out for all three types of control.

During the tests some changes were necessary on the designed controllers: an example is the washout filter introduced after noticing that the controller tended to interact with some rigid modes. An high-pass filter made possible to cut the frequencies for which these oscillations occurred. Other changes were needed during construction.
Another example: during tests at high speed (around 46-47 m/s) the model showed rigid modes oscillations along pitch axis. To avoid the repetition of this event in future sessions, a loose cable was added with the aim to limit the pitch angle of the model at an appropriate inclination, safeguarding the model and wind tunnel. The cable is loosely placed just to not affect the

characteristics of the model already studied in previous phases such as the GVT.

The types of excitation used have already been widely discussed: the impulse needs a deflection of the control surface of 10 degrees to sufficiently excite the system; the sweep signal in the band between 3-15 Hz is given with a 2 degrees amplitude excitation; white noise should excite sufficiently all frequencies with a value of about 0.5-1 degree.

All tests carried out are summarized in tab.6.10 cataloged per day, type of controller used, type of excitation, speed, percentage of gain and phase.

DATA TEST		28/01/2020					
TEST	NAME		INPUT	CONTROL TYPE	VELOCITY [m/s]	GAIN	DELAY [ms]
1	Sweep-S-20ms		Symmetric Sweep	No	20	-	-
2	Sweep-S-30ms		Symmetric Sweep	No	30	-	-
3	Sweep-S-40ms		Symmetric Sweep	No	40	-	-
DATA TEST		29/01/2020					
TEST	NAME		INPUT	CONTROL TYPE	VELOCITY [m/s]	GAIN	DELAY [ms]
da 1 a 10	WN-S-41_5ms-AC_ON-G=.....		White Noise	SOF	41,5	Da 0,15 a 0,7 passo 0,5	0
da 11 a 14	WN-S-41_5ms-AC_ON-G=.....		White Noise	SOF	41,5	0,8-0,9-1-1,2	0
DATA TEST		30/01/2020					
TEST	NAME		INPUT	CONTROL TYPE	VELOCITY [m/s]	GAIN [%]	DELAY [ms]
da 2 a 9	SOF-......ms-AC_ON-Delay=5ms		White Noise	SOF	Da 41,5 a 45 passo 0,5	100	5
da 16 a 25	WN-S-41_5ms-AC_ON-G=...		White Noise	SOF	41,5	Da 15 a 70 passo 5	0
da 25 a 30	WN-S-41_5ms-AC_ON-G=...		White Noise	SOF	41,5	80 90 100 120 200	0
da 43 a 49	ILAF_UW-......ms-AC-ON		White Noise	ILAF	Da 40 a 43,5 passo 0,5	100	0
da 53 a 61	ILAF_UW_41_5ms-AC-ON-Delay=5ms-G=...		White Noise	ILAF	41,5	Da 110 a 160 passo 10, 180 200	5
da 62 a 73	ILAF_UW_41_5ms-AC-ON-G=...		White Noise	ILAF	41,5	Da 60 a 160 passo 10	0
76	LQG42-UW-40ms-AC_ON		White Noise	LQG	40	100	0
77	LQG42-UW_41_5ms-AC_ON		White Noise	LQG	41,5	100	0
da 78 a 80	LQG42-UW-...ms-AC_ON-pulse		White Noise	LQG	41,42,43	100	0
DATA TEST		31/01/2020					
TEST	NAME		INPUT	CONTROL TYPE	VELOCITY [m/s]	GAIN [%]	DELAY [ms]
da 1 a 3	LQG-.......ms-AC_ON-G=0_9		White Noise	LQG at 45 m/s	41,5 42,5 43,5	90	0
da 4 a 11	LQG-.......ms-AC_ON-G=1_2		White Noise	LQG at 45 m/s	41-2-3,5 Da 44,5 a 46,5 (0,5)	120	0
da 12 a 17	LQG45-......ms-AC_ON		White Noise	LQG at 45 m/s	40 41,5 42 43 44 44,5	100	0
da 18 a 22	LQG45-UW-........ms-AC_ON-Delay=5ms		White Noise	LQG at 45 m/s	41,5 42,5 43,5 44 44,5	100	5
23	LQG45-UW-41-5ms-AC_ON-Delay=10ms		White Noise	LQG at 45 m/s	41,5	100	10
da 24 a 29	LQG45-UW-45ms-AC_ON-Pulse		Pulse	LQG at 45 m/s	41,5 42,5 43,5 44 44,5 45	100	0
da 30 a 31	LQGJ-UW-......ms		White Noise	LQGJ (John Berg's LQG)	40 41,5	100	0
32	SOFF-41_5ms-AC_ON		White Noise	SOFF	41,5	100	0
33	SOFFF-41_5ms-AC_ON		White Noise	SOFFF	41,5	100	0
da 34 a 35	SOFFF-......ms-AC_ON-GainPos-G=0_2		White Noise	SOFFF	41,5 42,5	20	0
da 36 a 50	SOFFF-......ms-AC_ON-GainPos-G=0_4		White Noise	SOFFF	Da 41,5 a 44,5 passo 1	40	0
da 36 a 50	SOFFF-......ms-AC_ON-GainPos-G=0_4		White Noise	SOFFF	Da 45 a 50 passo 0.5	40	0
da 51 a 53	SOFFF-......ms-AC_ON-GainPos-G=0_6		White Noise	SOFFF	46 48 50	60	0
da 54 a 56	SOFFF-46ms-AC_ON-GainPos-G=1_0		White Noise	SOFFF	46 48 50	100	0
DATA TEST		03/02/2020					
TEST	NAME		INPUT	CONTROL TYPE	VELOCITY [m/s]	GAIN [%]	DELAY [ms]
1 e 2	LQG45-UW-S-40-44_5ms-BW=12_0Hz		White Noise	LQG at 45 m/s BW 12 Hz	40 44,5	100	0
da 3 a 6	LQG45-UW-S-41_5ms-BW=12_0Hz		White Noise	LQG at 45 m/s BW 12 Hz	41,5 43 44 44,5	100	0
da 7 a 14	SOFFF2-......ms-AC_ON		White Noise	SOFFF 2nd version	41-2,5-Da 43 a 45,5 passo 0,5	100	0
da 15 a 19	SOFFF2-......ms-AC_ON-G=4.0		White Noise	SOFFF 2nd version	41,5 44 46 48 50	100	0
20	SOFFF2-41_5ms-AC_ON-OFF		White Noise	SOFFF 2nd version	41,5	100	0

Figure 6.10: Tests scheme.

The set of controllers tested is quite large. It contains several versions of the same control law, tuning gains or type of feedback data. For example two types of LQG are designed: one for 42 m/s and one for 45 m/s, or three type of SOF controller are used:

- **SOF**: it uses as feedback inputs accelerations, velocities and displacements extracted from the accelerometer ID: 2901 (left wing - LE) and

ID: 22 (right wing - LE), only accelerations from ID: 2902 (left wing - TE) and ID: 23 (right wing - TE). For a better clarification of ID location please refers to fig.3.6.

8 constant gains.

- **SOFF**: it uses as feedback input accelerations, speeds extracted by accelerometer of ID 2901, 2902, 2905 and 2906 for left wing and 22, 23, 25 and 26 for right wing.

  16 constant gains.

- **SOFFF**: it uses as feedback input velocities extracted by same sensors used in SOFF.

  8 constant gains.

  A second version (SOFFF2) is obtained tuning some values in the gain matrix.

The experimental campaign ended without any structural damage and proven the success of the AFS, with speeds up to 50 m/s. The results are promising, although the actual behavior differs in part from the numerical model one. The robustness of the controllers was able to fill this gap.

A summary of the stability of the tests as the gain varies for different controllers is inserted in fig.6.11.

Feedback gain	LQG designed at 45 m/s	Stability
0,9	43,5	Flutter speed
1,2	46,5	max speed reached still stable

Feedback gain	SOFFF	Stability
-0,2	43,5	max speed reached still stable
-0,4	50	max speed reached still stable
-0,6	50	max speed reached still stable
-1	50	max speed reached still stable

Feedback gain	SOFFF2	Stability
-1	45,5	Flutter speed
-4	50	max speed reached still stable

Feedback gain	ILAF UW + HP Filter	Stability
From 0,9 to 0,5 step 0,1	41,5	stable
0,5	41,5	stable (theoretical lower limit)
From 1,1 to 2 step 0,1	41,5	stable

Figure 6.11: Stability scheme.

The figure 6.11 is divided into three columns: the first indicates the test gain values; in the second is inserted the maximum speed reached with the gain of the first column and with the controller under examination; the last indicates whether instability is reached at the speed of the second column or if the controller has managed to keep the system damped enough.

In particular:
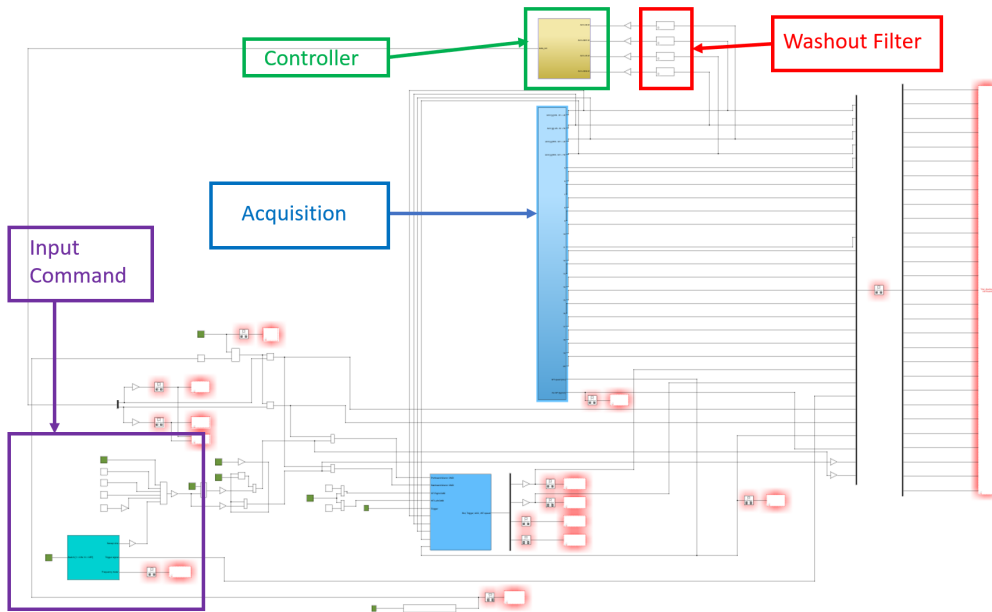
Figure 6.12: Test scheme.

- Max speed reached still stable: it indicates that the anti-flutter device is not activated at the speed and gain under consideration.

- Flutter speed: instability occurs in the conditions under examination and the controller is not able to dampen the system sufficiently. The anti-flutter device is activated by having the accelerometers read an acceleration value greater than $4g$.

- Stable: it is simply an indication of stability.

The scheme in fig.6.12 is the GUI used to conduct the wind tunnel tests. The blocks showed are the one explained in sec.6.1.2

- **Input command**: every block corresponds to the type of excitation described in sec.3.1.2 and it is possible to switch easily from one to another. All input are generated in degree and immediately converted to radians, considering that the control law deliver its outputs in this form.

- **Acquisition**: this block gathers all the measurement coming from sensors and delivers them to RTAI devices and to the controller.

- **Controller**: contains the control logic. Its plant depends on the philosophy adopted since the data extracted from sensor could change

(numbers and type of accelerometer). In the current figure it is shown the plant of first version of the SOF controller (fig.6.10).

- **Washout Filter**: as already said, their task is to avoid the interaction between the controller, designed to act on the deformable modes prone to instability, and the rigid body ones. Consequently they are placed just ahead of controller entries.

Chapter 7

Identification

Once all useful data are gathered thanks to wind tunnel tests, they are processed with the aim to extract indices expressing the dynamics of the closed loop system.

The wind tunnel tests and the acquisitions obtained have already been discussed enough in the previous chapter, here instead is illustrated the Simulink model of the corresponding numerical analysis representative of the entire wind tunnel test. By means of this simulation the numerical model is tested and its reliability is verified through a comparison with the result of the previous chapter.

In order to pursue the matching both types of data have to be manipulated and with them construct the relative FrFs.

Only at the end of this phase a stability analysis on the controllers can be carried out.

7.1   Numerical simulation

The experimental test chain is left the exact same also for numerical test, except for little necessary adjustments in order to run correctly the simulation.

First of all it is a numerical model, governed by matrix equations that depends on some parameters, such as velocity and density. In particular the aerodynamic of the model is expressed by $q\boldsymbol{H}_{am}(k, M)$ matrix resulting from DLM method. This makes necessary to build the ROM for discrete values of velocity and density, exploiting the dependence on the reduced frequency, Mach number and dynamic pressure.

Another aspect to remember, already discussed, is the contribution of the motor to the overall dynamics, expressed by eq.6.1.

Besides the plant dynamic, it is necessary to reproduce also the sensors dynamics. The accelerometer adopted during test are able to read accelerations until 50 Hz, value significantly above the frequencies of interest. Their response is modeled through the second order equation shown before (eq.6.3).

As well as done for the experimental setting, also for numerical one the GUI is presented in fig.7.1.
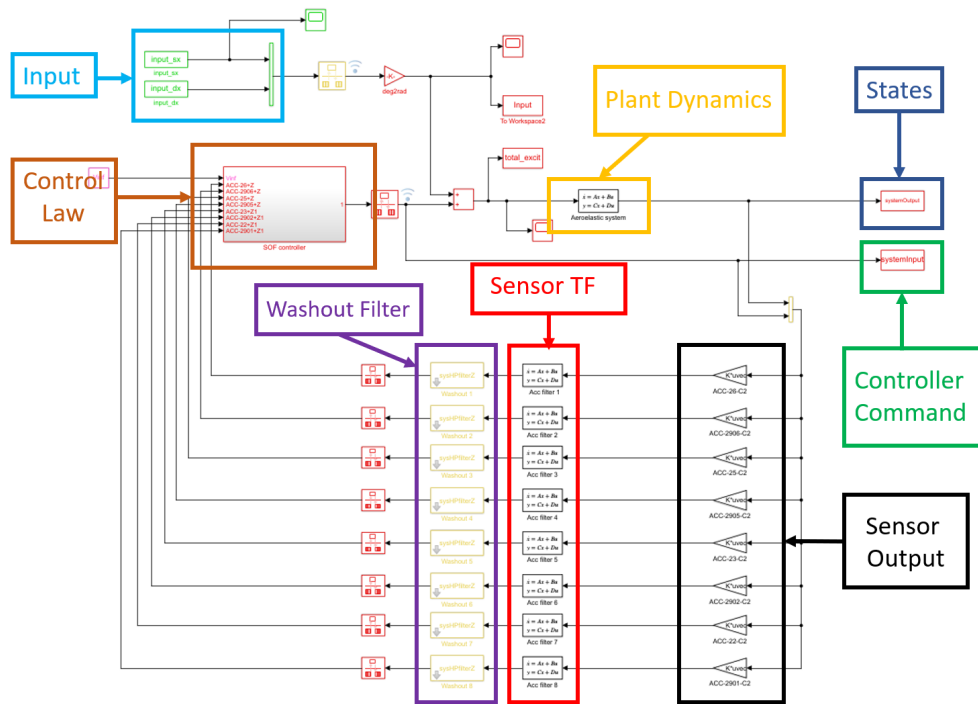
Figure 7.1: Simulink scheme.

It is possible to recognize:

- **Input**: the exciting signal is the same that forced the real aircraft during the experimental flutter test. So the same kind of control laws is tested with exactly the same input time signal.

- **Plant Dynamic**: state space representation of the ROM.

- **States**: time evolution of the system states.

- **Controller Command**: aileron deflection requested from the controller in order to prevent flutter.

- **Sensor Output**: numerical reconstruction of the $\boldsymbol{y}$ measurements. The outputs of the numerical model are the states, so it is necessary to obtain the measurement through the system matrices $\boldsymbol{C}$ and $\boldsymbol{D}$, recalling that $\boldsymbol{y} = \boldsymbol{C}\boldsymbol{x} + \boldsymbol{D}\boldsymbol{u}$.

- **Sensor TF**: transfer function of the accelerometer. It is represented in time domain through the system matrices.

- **Washout Filter**: the same filter applied also in experimental plant (fig.6.12).

- **Control Law**: the same block that appears in the experimental setting (fig.6.12). In the presented case the control logic is the velocity feedback SOF.

7.2 Identification phase

After the test activity and acquisition of a nourished database of FrF, the identification phase begins. It deals with the extraction of the modal parameters: it is a purely numerical phase in which the goal is to find values of modal parameters using a technique of parametric identification (the dynamics equations are known, but their coefficients are unknown).
The aim is to reconstruct the dynamic behavior of a system at hand through its excitation with suitable input, measuring its response and the input itself, if viable. So it is possible to classify identification techniques accordingly to having or not available measured input and the related processing can be carried out both in the time and frequency domain.

7.2.1 Methodology

For identification, being the acquired experimental signal affected by noise and errors, it is necessary to clean the database of time histories and find an interpolating polynomial that represents the input-output FrF.

The first step is to estimate the experimental function by means of the matlab function `tfestimate`. It finds a transfer function estimation given an input and an output signal, it returns a vector of frequencies expressed in terms of the sample rate at which the transfer function is estimated and its estimation.
Fig.7.2 is an example of estimation starting from wind tunnel test database values. The database from which the accelerometric measurements are drawn is that of the test at 41.5 m/s with SOF controller. As input is considered

the reading of the aileron encoder, as output data from sensor on left wing tip (ID 2901).
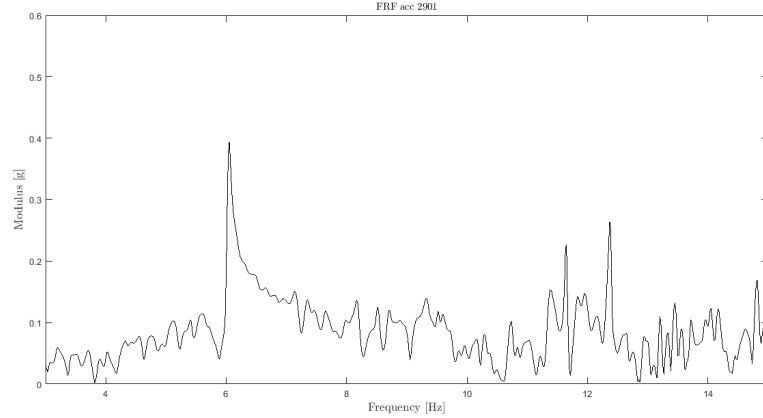
Figure 7.2: FrF input-output for accelerometer 2901 on the left wing.

This graph describes an example of a real FrF affected by noise: the frequency does not show a smooth trend throughout the field shown. Being at the flutter speed it is noted that the two modes, bending and torsional, are already in coalescence in a single 6 Hz peak.

The identified FrF is given by the transfer function calculated with the ARX method, below described.

ARX model The aim is finding a model capable of well identifying the flutter behaviour. The notation used will call Auto Regressive (AR) the model part, A, related to the system output y, eXogenous (X) the part, B, of the input variable u. Auto Regressive with eXogenous input (ARX). An ARX model is defined by the following synthetic form:

$$
\begin{aligned}
&A\left(z\right)y = B\left(z\right)u + w \\
&A\left(z\right) = 1 - \alpha_1 z^{-1} - \alpha_2 z^{-2} - ...\alpha_{n_\alpha} z^{-\alpha_{n_\alpha}} \\
&B\left(z\right) = \beta_1 z^{-1} + \beta_2 z^{-2} + ...\beta_{n_\beta} z^{-\beta_{n_\beta}}
\end{aligned}
\tag{7.1}
$$

expanded eq.7.1 into an explicit difference equation:

$$
\begin{aligned}
y\left(k\right) = &\alpha_1 y\left(k-1\right) + \alpha_2 y\left(k-2\right) + \alpha_{n\alpha} y\left(k - n_\alpha\right) + \\
&\beta_1 u\left(k-1\right) + \beta_2 u\left(k-2\right) + \beta_{n\beta} u\left(k - n_\beta\right) + w_k
\end{aligned}
\tag{7.2}
$$

With:

- α auto-regressive coefficients

- β exogenous part coefficients

- u input histories

- y output histories

- n_α ARX order for u

- n_β ARX order for u

- ω is the moving average

A scheme of this typology should be suitable for the identification of a system excited by a measurable excitation combined with external disturbances approximated through a generic unknown white noise.

In the case under examination the eq.7.2 is simplified like follow:

$$
\begin{aligned}
y\left(k\right) = &\alpha_1 y\left(k-1\right) + \alpha_2 y\left(k-2\right) + ...\alpha_p y\left(k-p\right) + \\
&\beta_1 u\left(k\right) + \beta_2 u\left(k-1\right) + \beta_p u\left(k-p\right)
\end{aligned}
\tag{7.3}
$$

p is the ARX order and β_i is the direct trasmission term. The output at the generic time instant k is written as a linear combination of a certain number of the passed input and output values, respectively p or in case of eq.7.2 n_α and n_β. The ARX function takes the input and output time histories as entries. In addition the order p of the polynomial ARX must be given. At the end of the ARX identification, the α_i and β_i coefficients are extracted.

The computational weight of the method is closely related to three parameters: sampling frequency, length of time histories and ARX order. The dimensions of the matrix to be inverted for the calculation of the coefficients is in fact connected to these values.

A brief explanation of how the coefficients are calculated and the consequent dependence in computational terms on the above parameters in the general case (where the system order is different: n_α and n_β, not only p) is given. For a correct identification it will need to perform an average to smooth out the effects of the disturbances, therefore many more samples will be available than the unknown parameters. The linear system will be overdetermined, since n_α and n_β will be less than the number of the sampled measures N. Therefore it will not be possible to satisfy the equation for each sample with the consequent presence of a residue ϵ within the solution equations. Then it is written system as:

Di Leone, Lo Balbo   135

$$\begin{Bmatrix} y_q \\ y_{q+1} \\ y_{q+2} \\ \vdots \\ y_N \end{Bmatrix} = \begin{bmatrix} y_{q-1} & y_{q-2} & \cdots & y_{q-na} & u_{q-1} & u_{q-2} & \cdots & u_{q-nb} \\ y_q & y_{q-1} & \cdots & y_{q-na+1} & u_q & u_{q-1} & \cdots & u_{q-nb+1} \\ y_{q+1} & y_q & \cdots & y_{q-na+2} & u_{q+1} & u_q & \cdots & u_{q-nb+2} \\ \vdots & \vdots & \vdots & \vdots & \vdots & \vdots & \vdots & \vdots \\ y_{q-1+N} & y_{q-2+N} & \cdots & y_{q-na+N} & u_{q-1+N} & u_{q-2+N} & \cdots & u_{q-nb+N} \end{bmatrix} \begin{Bmatrix} a_1 \\ \vdots \\ a_{na} \\ b_1 \\ \vdots \\ b_{nb} \end{Bmatrix} + \begin{Bmatrix} \varepsilon_q \\ \varepsilon_{q+1} \\ \varepsilon_{q+2} \\ \vdots \\ \varepsilon_N \end{Bmatrix}$$

Equation system is written beginning after q time instants have elapsed, i.e. starting from the q_{th} measure of the input and output (previous time instants are needed). The value of q is the maximum between n_α and n_β decreased by one.

Rewritten in a reduced way:

$$\{y\} = [A]\{\phi\} + \{\epsilon\} \tag{7.4}$$

Where $[A]$ as already said is a rectangular matrix and $\{\phi\}$ is the unknown vector of the model parameters.

Least Squares (LS) technique is used in order to find coefficients of the over-determined model and minimize residuals.

Objective function to minimize:

$$Obj = \frac{1}{2}\{\epsilon\}^T\{\epsilon\}$$

Whose derivation replacing in place of $\{\epsilon\} = \{y\} - [A]\{\phi\}$ is:

$$\delta Obj = \delta\{\phi\}^T\left(-[A]\{y\} + [A]^T[A]\{\phi\}\right)$$

for the minimization, being virtual variation of $\{\phi\}$ different from zero:

$$\{\phi\} = \left([A]^T[A]\right)^{-1}[A]^T\{y\} \tag{7.5}$$

In eq.7.5 it is clear that the computational cost for the calculation of the coefficients depends on the size of the matrix to be inverted, the pseudo-inverse matrix.

$$[A]^+ = \left([A]^T[A]\right)^{-1}[A]^T$$

Fig.7.3 is an example of ARX model identification starting from wind tunnel test database values. The database from which the accelerometric measurements are drawn is that of the test at 41.5 m/s with SOF controller like in 7.2. As input is considered the reading of the motor encoder, as output data from accelerometer placed on node with ID 2901.

In the example in 7.3 the order given to the ARX method is 300 poles. Obviously in this case it is an excessive number and in addition to taking the
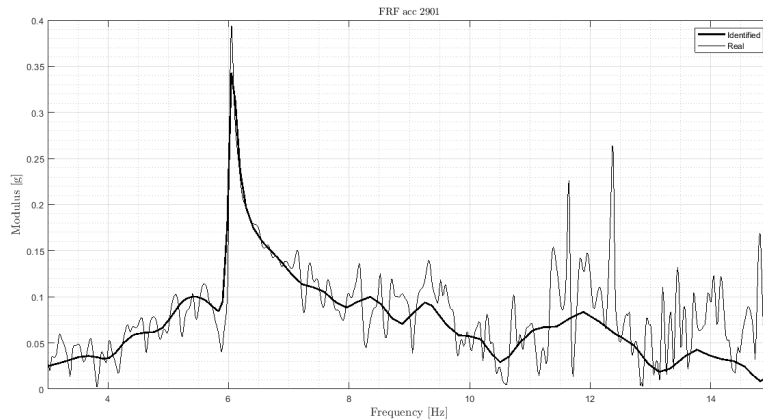
Figure 7.3: Tf input-output for accelerometer 2901 LE left wing with ARX method.

peak of the flutter it also reproduces frequencies of the noise band with higher amplitudes. Together with the identified function there is the representation of the real FrF estimated by `tfestimate`.

Some feature of computational cost of this particular case:

- Time to build $[A]$ matrix(14999x601) : 0.213758 s

- Time to compute pseudo-inverse of $[A]$: 2.945591 s

The size of matrix $[A]$ is determined by the duration of the time history (about 60 s), the sampling frequency (250 Hz) and the number of poles chosen or the order of the ARX method (300).
To calculate the transfer function identified starting from the coefficients it is necessary to use the matlab function `tf`. It creates a discrete-time transfer function with sample time that is the inverse of sample frequency used for acquisition.

ARMAX   At a certain point, during the identification phase, the need to use a more sophisticated method has come out. From here, the necessary to use an Auto Regressive with Moving Average and eXogenous input (AR-MAX) method to identify data particularly affected by noise or with abrupt variations.

The Moving Avarage (MA) part of the identification is important if the residue is not white, so it can be useful for 'accommodating' uncertainties of structure and disturbance, e.g. tunnel turbulence.

In the test conditions under consideration, tunnel turbulence should not be a problem. Furthermore, the model is validated and therefore the use of ARX is quite justifiable, although ARMAX can be more faithful despite its higher computational cost. In fact, the term $C(z)w$ is added to eq.7.1, therefore the size of the matrix to be inverted for the calculation of the unknown coefficients increases as a function of the order of the MA part of the system.

Following the additional coefficients to be introduced for the w part of the equation are presented:

$$C(z) = 1 + c_1 z^{-1} - c_2 z^{-2} - ...c_{n_c} z^{-n_c}$$

An ARMAX scheme should be suitable for the identification of a system excited through a measurable excitation combined with generic unknown disturbances, as shaped by $C(z)$.

7.2.2 Preliminary considerations

The presentation of the results starts from the first test day 28/01/2020 in which sweep excitation tests are performed with controller on and off at speeds of 20-30-40 m/s. The sweep input data from wind tunnel test is inserted with the same typology (bandwidth 3-15 Hz) and amplitude (2 degrees) as excitation in the Simulink model, in order to be able to compare the results with the real tests. The accelerometric data is available only for control-off configuration so it is not possible to perform a numerical-experimental comparison with control on treating the results before the flutter speed.

Open Loop For all three speeds, the input given to the system has the features shown in the figure 7.4. Three repetitions are performed for a duration of 45 seconds each one and with a pause of 10 seconds between one repetition and the next. It is acquired for a total time of about 170 seconds. The second figure in 7.4 represents the PSD of the input signal. It shows how the sweep covers the frequency spectrum required.
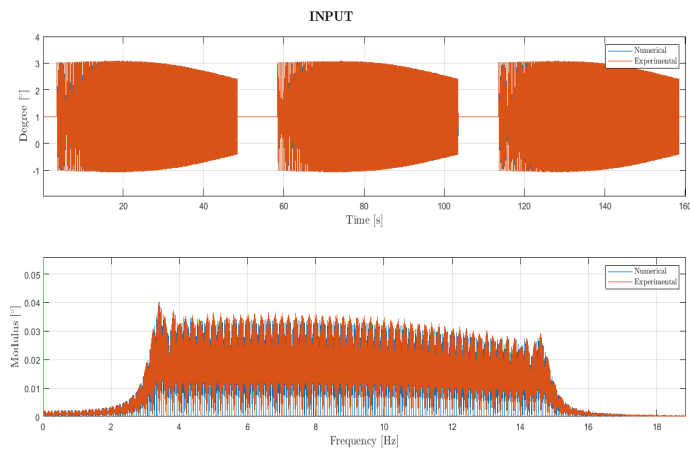
Figure 7.4: Input time history and corresponding PSD.

It is chosen to represent the time histories of the accelerometer 2902 (TE left wing) with the related PSDs as functions of speed, with excitation previously indicated. The comparison is made between data extracted from Simulink simulation and tunnel test data.
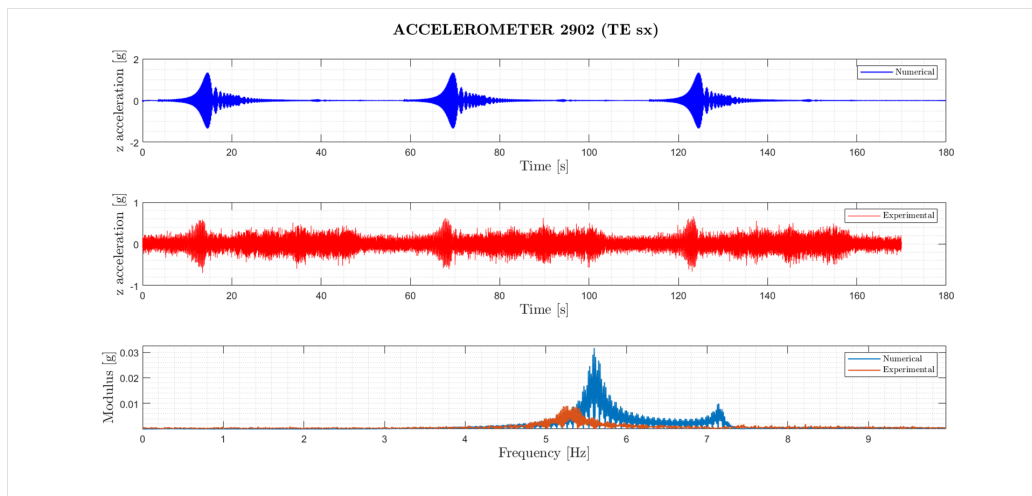
Figure 7.5: Time histories for acc 2902 and PSD at 20 m/s.
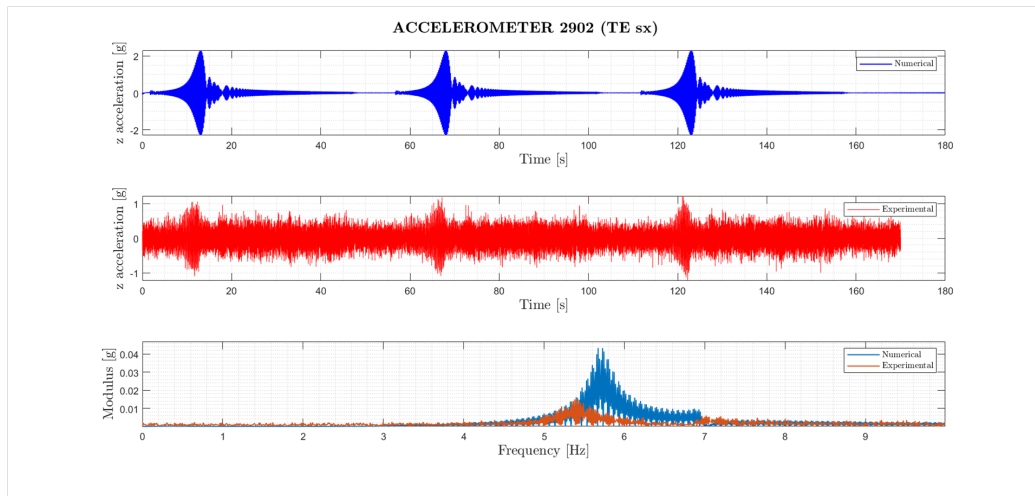
Figure 7.6: Time histories for acc 2902 and PSD at 30 m/s.
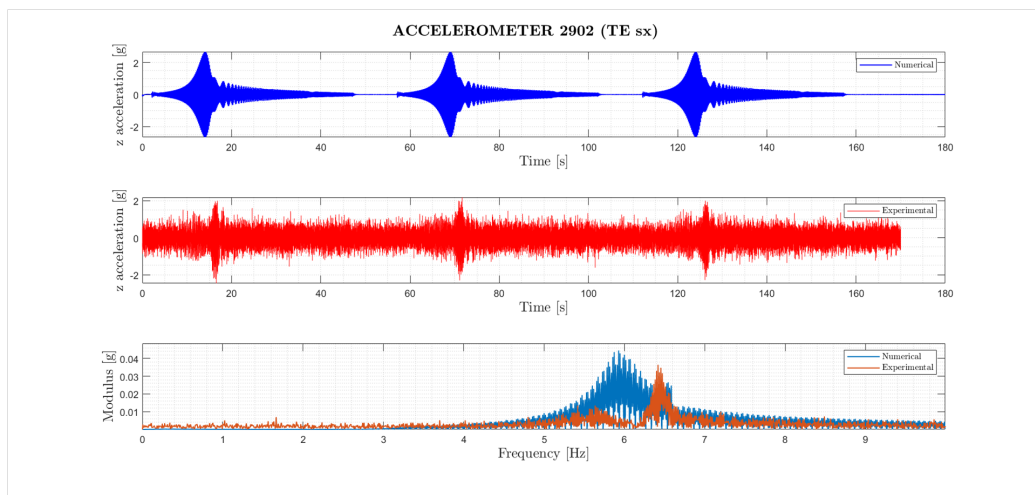
Figure 7.7: Time histories for acc 2902 and PSD at 40 m/s.

Remarks:

- The frequency shift is already observable from low speeds, the result of a non-perfect correlation of the frequency of the first bending mode in the ROM under analysis.

- In general, the numerical response is higher than the real one, an effect that can be seen both from the PSD and from the time history.

- The experimental data shows that the torsional mode at low speeds is not excited, as opposite to the numerical simulation.

- The coalescence of the unstable modes in the ROM begins to appear already around 30 m/s, while from experimental data it starts to be appreciable only from 40 m/s. In numerical simulation instability arises earlier.

The frequencies of the peaks are extracted from the graphs and compared in tab.7.8.

SPEED	FREQUENCY 20 M/S	FREQUENCY 30 M/S	FREQUENCY 40 M/S
BENDING TUNNEL	5.253 Hz	5.4 Hz	5.636 Hz
BENDING SIMULINK	5.6 Hz	5.672 Hz	5.928 Hz
BENDING PERCENTAGE ERROR	6.6 %	5.0 %	5.2 %
TORSIONAL TUNNEL	7.453 Hz	7.053 Hz	6.418 Hz
TORSIONAL SIMULINK	7.14 Hz	6.872 Hz	6.544 Hz
TORSIONAL PERCENTAGE ERROR	4.4 %	2.6 %	2.0 %

Figure 7.8: Frequency error to varying of the velocity.

Closed Loop   Then the controller is introduced in the plant and the loop is closed. In order to see how it impacts on the system dynamics a simulation is run at a speed of 40 m/s, neither so far from instability nor too close to cause the open-loop divergence. Thus a comparison is made between the outputs in open and closed loop. In fig.7.9a the actual command given to the aileron as the sum of input command and correction given by the controller (SOF). Showing the difference between open and closed loop command, the figure helps to understand how the AC command acts on time history of the signal and how the frequency content of the excitation changes.
The regulator tends to cancel the frequency content of the input up to 6.5 Hz, moving it at higher frequencies. The result is shown in the fig.7.9a.
    The same procedure is carried out for the LQG controller (fig.7.9b).
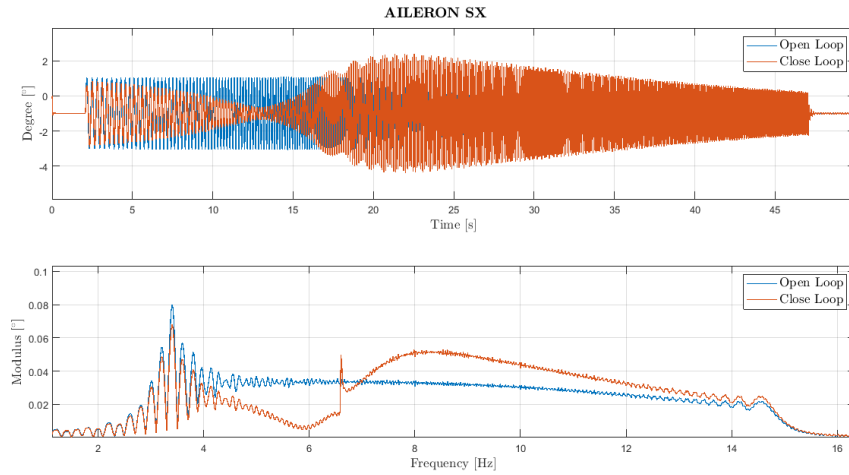
(a) SOF.
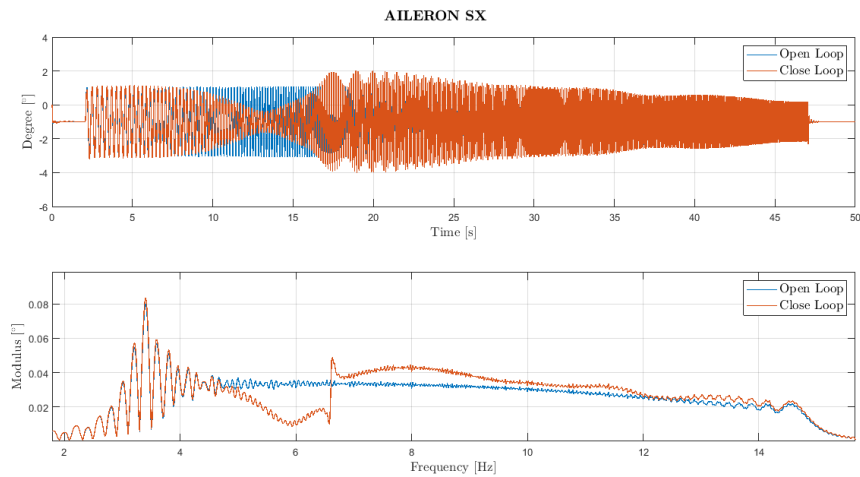
(b) LQG.

Figure 7.9: Deflection of left wing aileron in open and closed loop.

The correction effect introduced by the controllers appears to be similar to each other. Both work by lowering the frequency excitation modulus before the flutter frequency and increasing it after.

In fig.7.10 is presented the comparison in terms of time history and PSD also for accelerometer 2902 (TE - left wing), in open and closed loop with SOF. The figure is useful to understand the functioning of the controller and how it acts on the system.

According to the figure presented, the considerations made are two:

- The controller spreads the frequency content giving rise to a much more
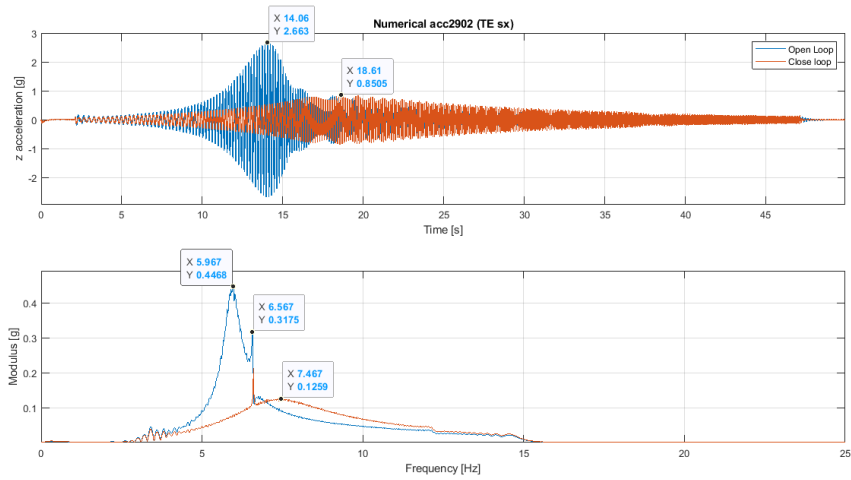
Figure 7.10: Comparison of time history and PSD of acc 2902 in open and closed loop (SOF).

damped peak, which goes from a maximum acceleration value of 2,663 g to a value of 0.851 g with control-on. A reduction of the 68%.

- It seems to act mainly on the bending mode, whose peak frequency, width and amplitude changes massively.

Finally, in fig.7.11 the same comparison open and closed loop using LQG controller.
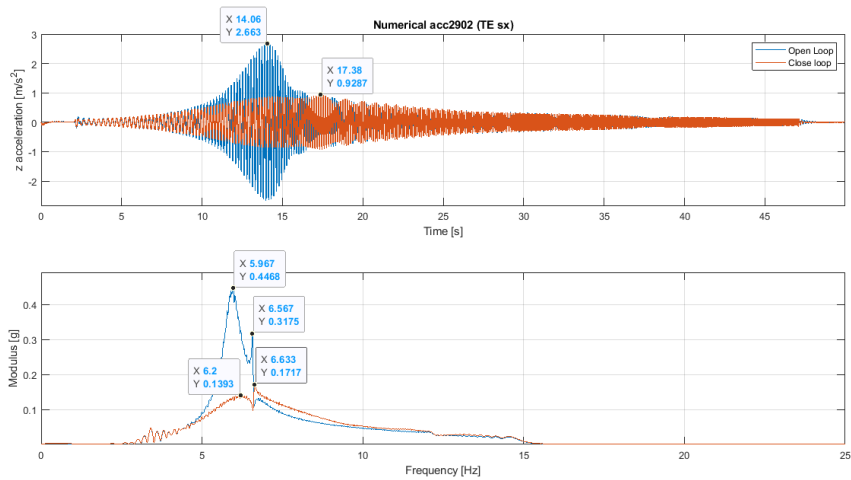
Figure 7.11: Comparison of time history and PSD of acc 2902 in open and closed loop (LQG).

Unlike the previous one, the bending mode peak is not spread and shifted in frequency but it is simply reduced in amplitude. In this occasion also the torsional mode is involved in AFS intervention. In view of the same acceleration level in open-loop case, LQG provides a closed-loop maximum acceleration value of 0.929 with a percentage reduction of 65% (fig.7.11).

A comparison between the two controllers is expressed in terms of PSD with respect to the open loop conditions and to their action on the two modes in examination.

Mode	Open loop modulus PSD	Closed loop modulus PSD	Percentage reduction
BENDING SOF	0.447	0.126	71.8 %
BENDING LQG	0.447	0.139	68.9 %
TORSIONAL SOF	0.318	0.213	33.0 %
TORSIONAL LQG	0.318	0.172	45.9 %

LQG seems to act more on the reduction of the torsional peak than SOF does.

7.2.3   Controller results

To provide a complete treatment of flutter stability, it is essential to appreciate how the dynamic behavior of the structure changes with the introduction of the controller.

Starting from experimental data (in: control surface deflection, out: accelerations) the identification permits to curve fitting the data using a predefined mathematical model of the measured structure, trying to derive all modal parameters in a analytical formula of an FrF using measurement data. The kind of identification implemented is explained in sec.7.2.1 and provides for a user action at every step.

Then, through the FrFs of the closed loop system, the stability performances are computed.

The structural behavior varies following the velocity changes, hence also the FrFs changes accordingly. For this reason a set of FrFs are computed in order to see their evolution in relation to velocity trend.

SOF

The first controller analysed is the SOF with velocity feedback. Choice justified firstly by the fact that the SOF version based on a velocity feedback leads to better performance relative to the acceleration direct feedback one. The second reason is a consequence of the first one, in fact the great effectiveness of this controller permits to cover a wide range of flight velocities, its strong performance permitted to gather a lot of data. Finally, the test session on this controller takes place with gain and phase equal to that of the preliminary design without any phase delay or changing in gain. The maximum velocity tested with this controller is 45.5 m/s, that means about a 10% increasing with respect to the flutter velocity.

Experimental FrFs The set of velocities tested contains the same configuration of the system (aircraft in configuration prone to flutter, controller with unitary gain and no extra delay). The roster of velocities is formed by: 41.5 - 42.5 - 43 - 43.5 - 44 - 44.5 - 45 - 45.5 m/s (refer to tab.6.10).

The identified FrF represents the relation between accelerometers data (g) and white noise aileron input (expressed in radiants).
The results of the identification regard the data reads from accelerometer 2901 (LE - left wing). The leading edge is more subjected to torsional effect, due to its bigger distance from elastic axis, with respect to the 2902 sensor (TE).
In fig.7.12 two curve are overlapped: the *identified* one is the FrF obtained with ARX method, the *real* one instead is the result of the classical procedure to compute transfer functions through estimations method [16]. The ARX algorithm tries to fit in least-square sense the estimated FrF with a number of poles indicated by the user. The order of the rational polynomial formula is the result to the attempt to fit as best as possible the peak, in terms of frequency, amplitude and width. Following this criteria, the order shows this tendency: the lower is the velocity and the higher is the order required, considering obviously velocity range around the flutter point (from 41.5 to 45.5 m/s). This is due to the interaction of two modes: when the velocity is not in the exactly proximity of the flutter condition, the modes coalescence has not completed yet, so they are enough distinct and the algorithm needs more poles to follows these abrupt changes in a so little band; indeed, when the flutter effects becomes important, the controller start to restrict the structural response producing only one distinguishable peak, easier to interpolate. Generally the number of poles used goes from 50 to 150.

The basic concept behind the SOF strategy can be summarized with an action aimed to spread the bending participation, avoiding the coalescence.

(a) Velocity: 41.5 m/s

(b) Velocity: 42.5 m/s

(c) Velocity: 43.5 m/s

(d) Velocity: 45.5 m/s
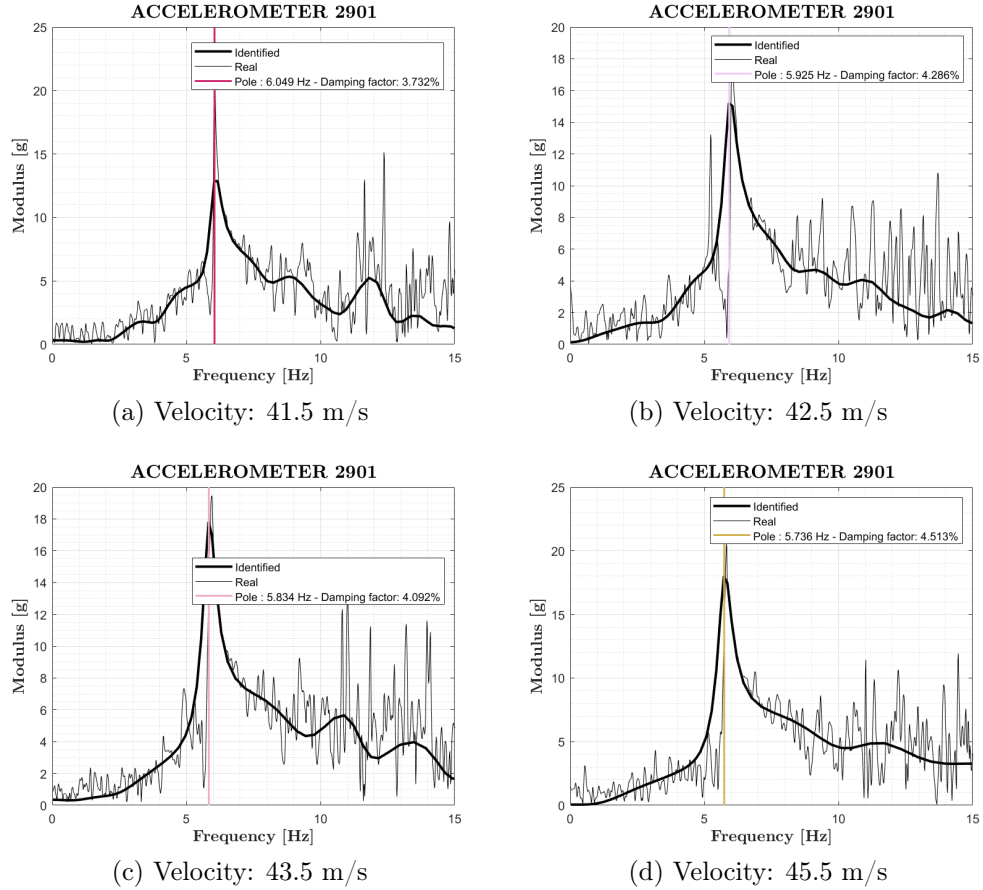
Figure 7.12: Experimental closed-loop trend with the increasing speed - SOF.

As a consequence a second dominant peak stands out, representing the torsional effect, since the SOF regulator is tuned on bending frequency.

Numerical FrFs The FrFs identified are the ratio between sensors acceleration output (m/s^2) and white noise input supplied by means of ailerons (measured in radians). These quantities are the ones presented in fig.7.1 and obtained with a numerical simulation with the aid of Simulink.

In order to make a profitable comparison the Simulink run is accomplished with the same controller version. However, the velocity set is different because the state space aeroelastic model was generated in correspondence of the following velocities: 40 - 42 - 45 - 47 m/s.
Again the choice fell on the accelerometer 2901 for the reasons illustrated before.

Not being present wind tunnel noise, the FrFs under consideration are

(a) Velocity: 40 m/s

(b) Velocity: 42 m/s

(c) Velocity: 45 m/s

(d) Velocity: 47 m/s
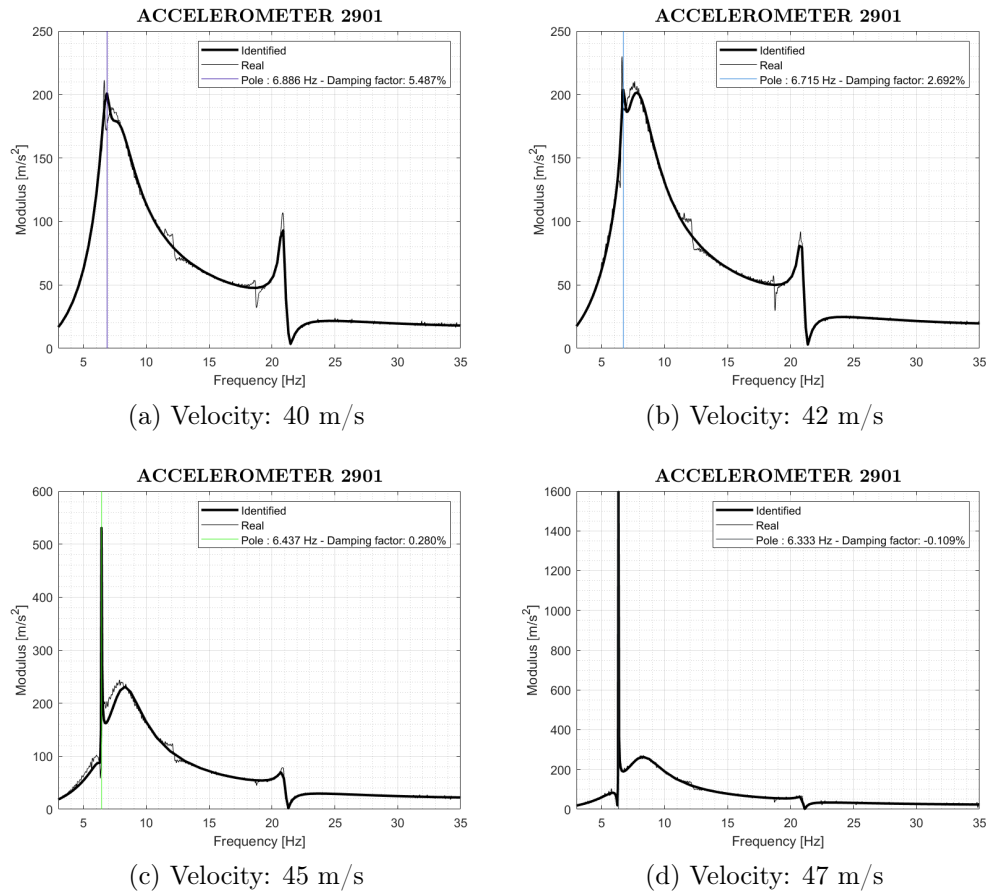
Figure 7.13: Numerical closed-loop trend with the increasing speed - SOF.

cleaner and consequently less poles are necessary to get a good overlap, around 70-100.

The high and very narrow peak stands out in correspondence of flutter frequency. This very evident effect occurs only in the numerical model and it can be due to the absence of structural damping that makes it very narrow and to discrepancies between the real model and the MSC/NASTRAN one.

Frequency and Damping For flutter purposes it is crucial to base the considerations in terms of frequency and damping ratio, since the flutter is actually a lack of damping. Therefore, from ARX identified FrFs are extracted these quantities and plotted all together, taken from experimental and numerical result, for both the right wing tip accelerometers and left ones.

DAMPING RATIO

(a) .

FLUTTER FREQUENCY
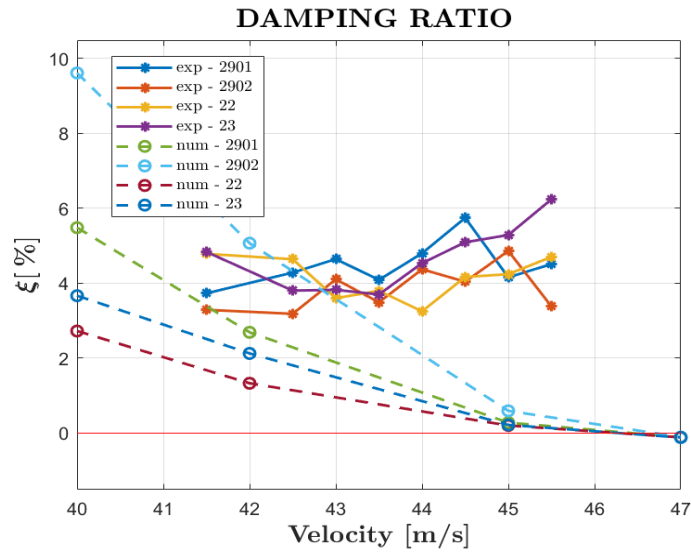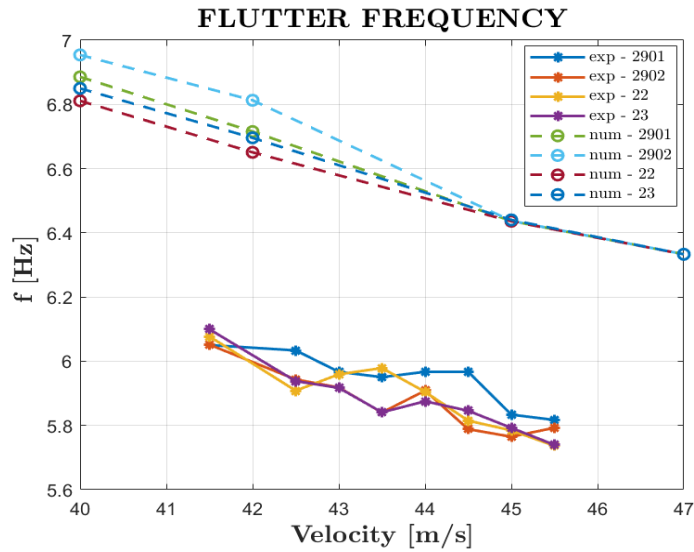
(b) .

Figure 7.14: Numerical and experimental closed loop results.

Some considerations can be inferedr from plot 7.14:

- As might be expected, in the numerical appears more plainly a tendency, also because the FrF interpolation is easier to carry out.

- Damping settles around value of 4% meaning that the controller is able to manage the instability with a certain effectiveness until the 45.5

m/s. On the contrary the numerical model diverges reaching negative damping ratios and remarkably high peaks. This is clearly a symptom of a lack damping affecting the mathematical model and a correlation not optimal yet of the first optimization run model.

- Both models keep a constant decreasing trend on flutter frequencies, but appears also a constant shift seen in the time histories of fig.7.7. This discrepancy is due to the shift already noted in the previous chapter in the V-f graph of the model after the first updating phase, i.e. the model turned out into state space form and used for the design of the controllers. It consists in a percentage variation of 9% with respect to the experimental frequencies.

LQG

The other controller under investigation is the LQG designed for 45 m/s, tested on 31/01 (see fig.6.10). This is the one that produced the best results, in fact its optimal response allowed to test a rich set of velocities. The maximum velocity tested is 46.5 m/s, meaning a 12% higher than open-loop flutter velocity.

Experimental FrFs The closed loop system dynamics, with LQG control law, is resumed in FrFs of fig.7.15
The LQG closed-loop system response seem to be more nervous than the SOF one, but the generally the amplitudes are smaller: that is, smaller accelerations and subsequently smaller loads. Another aspect to highlight is the presence of two close peaks even at high velocities: this control strategy acts differently relative to SOF control. Respectively, one attempts to limit the global level of acceleration, operating on the overall structural response and so both on bending and torsional contributions (as already discussed for fig.7.11), the other instead focuses its intervention especially on the bending mode. This explain why in LQG FrFs (fig.7.15) there are two peak with equal amplitude. LQG action, as a matter of fact, targets to limit the accelerations given that its design is based on those measures. In particular, it centers the efforts exactly at flutter frequency (around 5.8 Hz) with a powerful intervention to break down the response amplitude. This produce a split into the big merged mode, that ARX algorithm is not able to catch in view of the fact that it is a tool to grab global behaviors.

Numerical FrFs The numerical graphs follow the same pattern of the real ones, because it is easy to recognize the progressive arise of two different

(a) Velocity: 41.5 m/s

(b) Velocity: 43.5 m/s

(c) Velocity: 45.5 m/s

(d) Velocity: 46.5 m/s
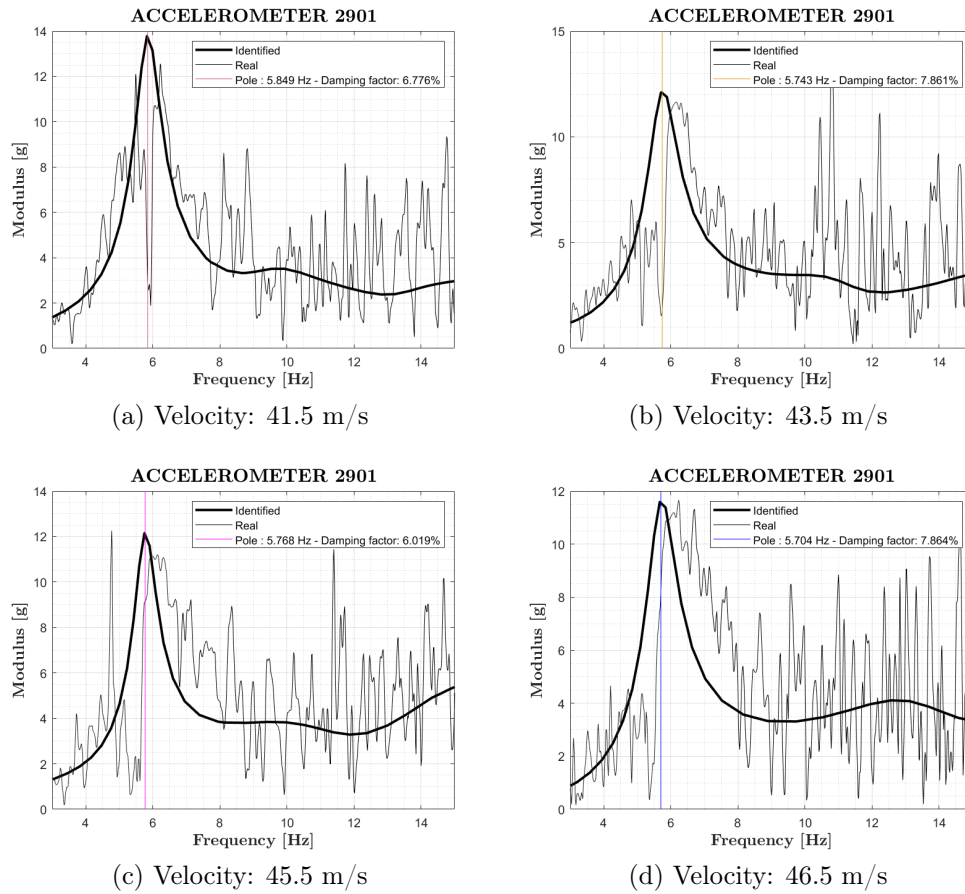
Figure 7.15: Experimental closed-loop trend with the increasing speed - LQG.

vertices from the one big instability mode. The absence of wind tunnel noise makes also the visual analysis easier.

The AFS system starts to take action after 40 m/s, reducing the overall amplitude and mostly addressing its efforts on the instability frequency, almost cancelling the structural response at that point, showing its effectiveness.

Another important aspect lies in the progressive decrease of the amplitude at higher velocity, indication of the good performances of the controller for a large range of velocities (the LQG is designed for 45 m/s).

Frequency and Damping   The fig.7.17 synthesizes the quantities useful to flutter analysis provided for most involved accelerometers.
Remarks:

(a) Velocity: 40 m/s

(b) Velocity: 42 m/s

(c) Velocity: 45 m/s

(d) Velocity: 47 m/s
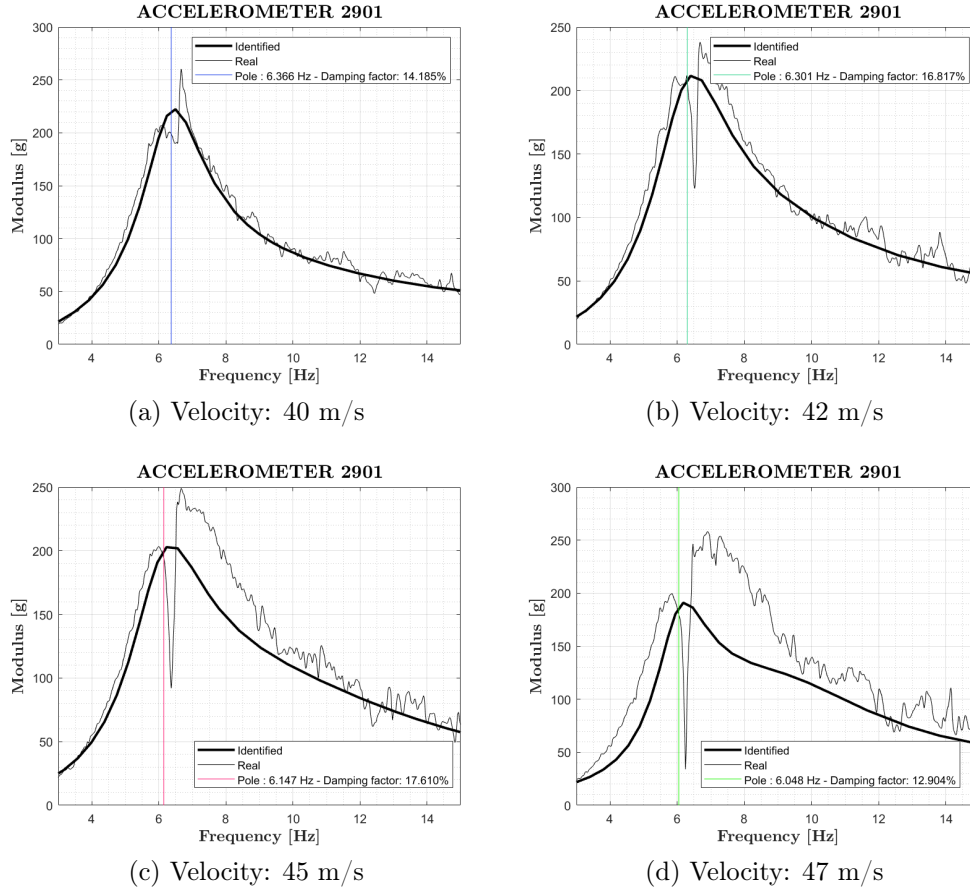
Figure 7.16: Numerical closed-loop trend with the increasing speed - LQG.

- The same frequency shift, seen previously, can be noticed. As with the SOF controller, the wind tunnel model has lower frequencies than the first updated version of FEM model.

- This time instead of decreasing in speed as expected from the graph V-f in fig.4.19a, the controller maintains the flutter frequency with a constant trend. The frequency of the mode settles and it does not vary with the increasing speed, except for some data oscillations.

- The damping ratio in this case is much larger than SOF's one. The coalescence of the two peaks remains unchanged (even if they are divided, they belong on the same unstable mode). As opposed to the former, LQG acts at the point of maximum instability by reducing its response. Instead of extensively damping only the bending mode, LQG acts simultaneously in the two modes in coalescence.

• LQG does not present any kind of instability, also for high velocities.
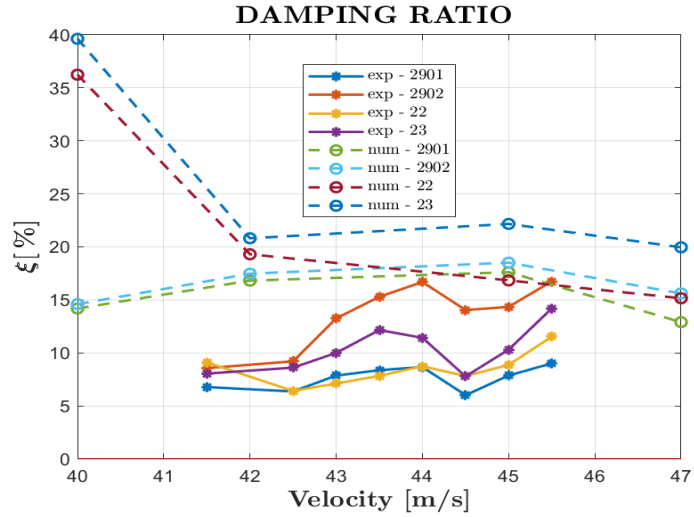
(a) .
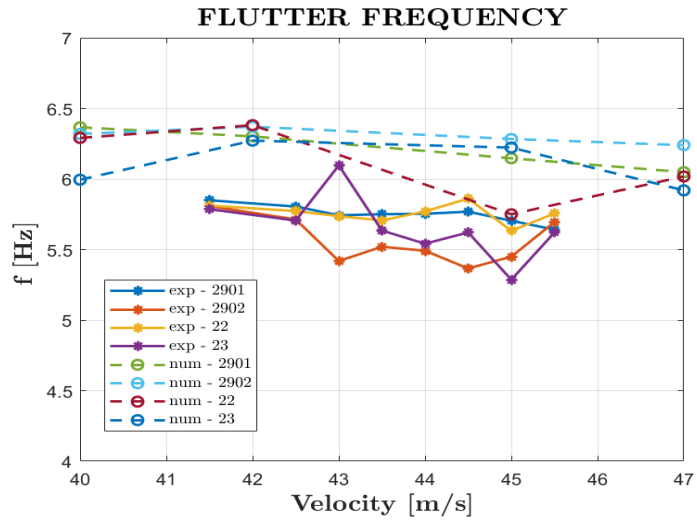
(b) .

Figure 7.17: Numerical and experimental closed-loop results.

7.3   Robust Stability

According to the control theory, the design of a controller, in order to be considered reliable and certified, has to pass from the study of its performances. It is not sufficient to fulfill the stability requirements, because they are related to a particular operating condition, it is also needed to verify how strong the stability is, called generally *robustness*.

For an AC system, and all the more for an explosive phenomenon controller, it is an essential requirement. The regulator has to be very performing at the design conditions but it has also to be able to tolerate perturbations that might affect the system's functioning, since the flutter condition can be unexpected, various and very intense. So, a robust controller is able to tolerate and approach to uncertainties affecting the plant dynamics.

7.3.1   Controller Margins

Common indices used to measure the immunity to the uncertainties of a control law design are the Gain Margin and Phase Margin [8]. Phase and gain margins indicate how close the system is to instability.

The experimental and numerical phase and gain margins are calculated both considering a the same SISO system (aileron rotation to AC command) to allow the comparison. With terminology 'numerical' it is intended the values extracted from Simulink simulations, while 'experimental' indicates data acquired from sensors during wind tunnel tests. During the execution of the tests, for this purpose, many kind of data were gathered by changing the controller's gains and adding a phase delay into the measurement chain, as indicated in fig.6.10. In fig.6.3 is pointed out the methodology with which the delay is inserted. To change the gain it is simply necessary to multiply the gain matrix by the percentage to which the controller has to be tested. In this thesis work the data to varying of gain and phase are not processed but a synthetic illustration of the stability and robustness of the closed loop system is treated (fig6.11).

To ensure firstly the system stability a check on the eigenvalue of the closed-loop system can be done. The roots of $[A(z)]$ in eq.7.1 represent the poles (or eigenvalues) of the identified system. This will be stable if all its poles are within the circle of radius 1, i.e. $|z| < 1$. In the cases analysed, the eigenvalues of the FrFs are within the unit circle and the modulus is usually close to the unit value. In fig.7.18 the stability region for a discrete-time transfer function.

The control laws tested are built around a design speed, so the evaluation of the robustness is conducted computing the stability margin of the system
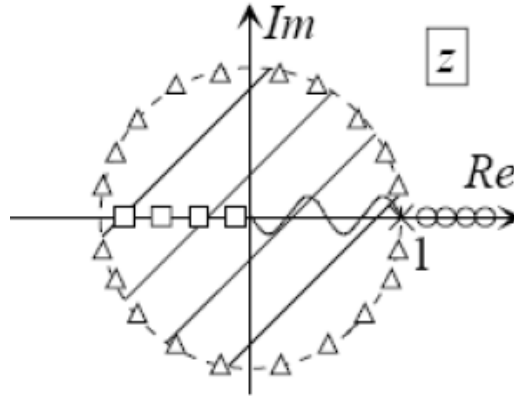
Figure 7.18: Stability region for discrete-time transfer function poles.

as the speed changes and an attempt is made to trace the phase and gain margins starting from the identified FrFs. The calculation of the stability margins for the SISO system chosen is carried out with the `margin` function of Matlab. This function studies the stability of loop transfer function, that is the product of the previously identified FrFs with the controller transfer function. To better explain, the relation between the reading of the encoder and the command required by the AC.

It is possible to appraise the results of the application of the stability margins on the identified function representing the feedback system for the different speeds under analysis in tab.7.2 for the only SOF controller.

RIGHT AILERON			LEFT AILERON		
	Minimum margins			Minimum margins	
V [m/s]	Gain Gm [-]	Phase Pm [°]	V [m/s]	Gain Gm [-]	Phase Pm [°]
41.5	1.204	15.942	41.5	1.212	15.573
42.5	1.643	15.359	42.5	1.605	15.016
43.0	1.680	20.112	43.0	1.788	19.099
43.5	1.996	20.477	43.5	1.980	19.783
44.0	1.636	26.905	44.0	1.627	26.237
44.5	1.782	23.932	44.5	1.779	23.342
45.0	1.875	32.999	45.0	1.798	32.609
45.5	1.878	37.487	45.5	1.888	36.860

Table 7.1: Minimum margins for right and left ailerons between.

All the margins value are find in a bandwidth of maximum 50 Hz. The number of poles used to reconstruct the loop transfer functions is found after a convergence analysis at the end of which the gain and phase margins settle around a stable value.

For the calculation of some margins at low speed (e.g. 41.5/42.5 m/s) it was necessary to use an alternative identification method compared to the ARX one used so far, the ARMAX. In fact, the ARX method is unable to reflect properly the trend of the peak at the flutter despite the continuous increase of poles inserted in the algorithm. This issue does not appear at higher speeds because the signal-noise ratio in the measurements is lower.

The reason why only the stability margins of the SOF controller are represented is that the action of the LQG controller is much more nervous and therefore it is quite difficult to identify the FrF, and consequently to trace the margins, of its closed-loop system.

An example of comparison between the estimated closed-loop FrFs for the SOF and LQG controllers at a speed of 41.5 m/s on the left wing are shown in fig.7.19. The frequency range under analysis is $3-50Hz$. Data are always reported to the configuration with mass in backward position.

(a) SOF closed-loop estimated FrF. (b) LQG closed-loop estimated FrF.
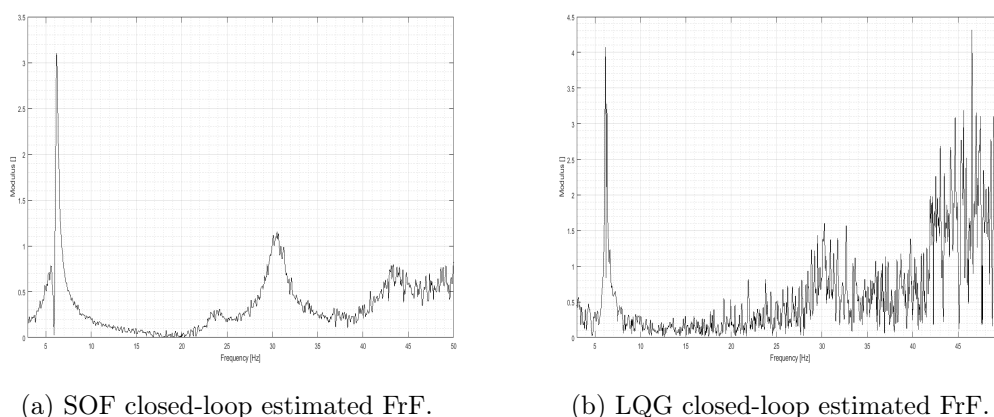
Figure 7.19: SOF and LQG closed loop results on left wing for 41.5 m/s.

Fig.7.19b has a signal that at high frequencies does not allow the ARX function to correctly represent the trend of the identified FrF, which therefore shows margins at high frequencies and without physical correspondence.

As regards the calculation of the margins by means of Simulink, following the same procedure previously indicated, it is possible to compute the margins for both controllers since there are no noises or disturbances in the numerical system.

The input for the closed-loop FrF is the same as for the calculation of the previously described SOF margins (encoder reading).

In the simulink simulation the model is symmetrical and the input between the right and left aileron is almost identical, consequently the difference be-

tween the right and left results are no longer considered. Consequently only the margins of one side are presented for both controllers. Exactly as for the FrF identified by the data acquired during the week of wind tunnel tests, the margins of the numerical simulations for the two controllers are shown in tab.7.2.

SOF controller			LQG controller		
Minimum margins			Minimum margins		
V [m/s]	Gain Gm [-]	Phase Pm [°]	V [m/s]	Gain Gm [-]	Phase Pm [°]
40	4.737	52.855	40	1.6397	39.651
42	4.307	44.916	42	1.7469	47.566
45	0.996	-0.2151	45	1.8204	63.544
47	1.168	7.356	47	1.9614	61.219

Table 7.2: Minimum margins for SOF and LQG controllers with speed

From the margins calculated thanks to numerical simulations it can be inferred how the SOF closed-loop is close to the instability at 45 m/s, instead the LGQ gains robustness with the increasing of speed, given that it is designed for 45 m/s.

Based on the Bode criterion, asymptotic stability is guaranteed if the gain μ of the loop function and the phase margin ϕ_m are both positive [1], within its validity assumptions. Always in [1], the criterion of bode and its hypothesis are stated. The feedback system referred to the Bode criterion is precisely the system reproduced by the FrF identified with the ARX method and fed to the `margin` function.

The `margin(sys)` function calculates the most critical margin among those obtained for the FrF (`sys`) entry. For some FrFs it is necessary to extract all the margins with the `allmargin(sys)` function of Matlab in order to check their values in the frequency range of interest.

The interest in using such a function is the study of possible conditions as shown in the figures 7.20a and 7.20b, where cases in which the loop function exceeds more than once the negative real half-axis and the unit radius circumference are represented.

(a) Multiple intersections of the negative real half-axis.
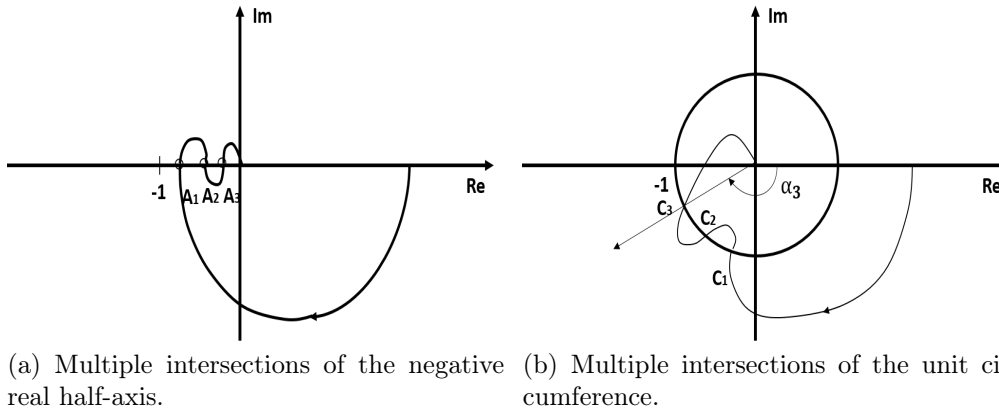
(b) Multiple intersections of the unit circumference.

Figure 7.20: Examples of noteworthy polar diagram.

Chapter 8

Conclusions and Further Improvements

The main objectives of the preset work are: building a new FEM model of the X-DIA, able to catch with an higher level of accuracy the flutter mechanism and starting from it, the implementation of a AFS system validating its functioning.

First part of the work is based on FEM model developments, in which the way chosen to improve the quality addresses to structural modeling aspect. An hybrid description of the structure is the best compromise between accuracy and computational burden. A **detailed modeling** of the wing is demanded due to the particular shape of the cross section: the omega configuration presents some sensitive issue about its torsional behavior, since it is dealing with an open section. So a shell element description is used for the wing-spar and solid one for the clamp with the fuselage in order to recover as best as possible the real torsional behavior.

This approach improves particularly the quality of the representation of the modal shapes, essential factor in flutter study.

Within this framework the pod influence fits: the safety device has a great impact on the dynamic and aerodynamic of the structure. From structural point of view it is a crucial element because substantially it consists in a big cantilever mass located in a zone affected by compliance. Consideration that the GVT's results confirmed.

Some discrepancies are bridged thanks to the **updating phase**. The success in a modeling updating is significantly related to a smart parameter selection, illustrated by some general rule already mentioned in sec.4.3.4. For simplicity and due to technical issues with the implementation of the SOL200 in MSC/NASTRAN, it was not possible to carry out an updating process acting directly on mode shapes, so on the basis of the previous rules

the optimization phase is set to address its intervention to the parameters that are directly involved in structural behavior, to restore torsional stiffness. A deeper approach could take in account for a modal test focused mainly on pod dynamic and run the solver including in the objective function also a MAC index.

The **anti-flutter device** alters a lot also the aerodynamic properties of the aircraft, undermining mostly on torsional modes. Thanks to numerical simulation it is possible to see the difference between the model equipped with the aerodynamic modeling of the pod and not: the aircraft approaches to instability condition much earlier with considering its aerodynamic properties. Thus, the flutter stability is very sensitive to this element.
A fine aerodynamic modeling of this element is a very challenging task because of its not slender shape and the presence of many slots that make it not a perfect interference body. A possible solution can lie in a parametric modeling of the component based on its diameter. At the moment its interference surface is reduced by a percentage to decrease its effectiveness but a more in-depth study can lead to a better representation.

All these efforts are aimed to the construction of a numerical model able to predict correctly the flutter outbreak as well as the capacity of the anti-flutter device to block this instability due to sliding mass. So the last part of the correlation is focused on recognizing the predicting abilities of the model. The results in terms of aerodynamic damping are pretty promising because both the trend and the flutter velocity are caught with a very low error, 2.4% with respect to experimental velocity found in wind tunnel tests.

The succeeding **identification phase** shows that generally the numerical response is larger than the real one, so adding a structural damping term in the equations might smooth this difference. A scaling process on the aerodynamic modeling provided by DLM moves in this direction as well. It is known that the effectiveness of the numerical aerodynamic forces usually is overstated.

Many types of AFS systems are tested with quite satisfactory results. This work focuses only on **SOF** and **LQG** since they are the control laws that produced better results and with a wide set of data available. The former has on its side the design simplicity and easy tuning. The closed-loop system turns out to be stable at the velocities at which the open-loop ones diverges, going beyond the instability point of about a 10%. The controller cuts the bending contribution at the flutter frequency and spreads it on a larger bandwidth, in fact the only remarkable peak is around 6.2 Hz. During wind tunnel test it was possible to appreciate visually how the airfoil twisted nervously but no bending effect was observable. Conversely, a torsional contribution is still present whom SOF is able only to limit.

The latter instead, despite an heavier computational burden, provides better results as for damping and response amplitude. The AC command is addresses to both modes and, as a consequence, the overall acceleration level is lower than SOF's. In this case two different peaks can be noticed but with lower amplitude and more damped. The action of the controller seems to be aimed to keep them separate, in fact with the increasing velocity the acceleration value in correspondence of the exact flutter frequency tends to decrease until to reach a level of acceleration 7 times lower than the maximum acceleration one. This provides a tested velocity of 46.5 m/s, that is 12% higher than the open-loop one.

A further check that should prove the goodness of the results consists in run a closed-loop flutter analysis in MSC/NASTRAN with SOL145. This test, as opposed to the Simulink simulation, does not contain errors due to reduction of the model since the complete FE model, after being correlated, could be considered as an high-fidelity model.

Nowadays a particular feature that a control synthesis can not miss in order to be certificated and installed on a real aircraft is the **robustness**. It is essential aspect in the industrial world, a control system must be able to overcome to small defect during production phase or differences between same flight vehicles but built in various establishments.

Thus it is praxis to, once tested and verified the control laws within the design conditions, vary some parameters in order to see its off-design attributes. Interesting procedures are:

- introduction of delays along test chain

- lowering gains

- adding noise numerically

- remove a measure to simulate a sensor failure

During the wind tunnel test, the type and configuration of the flight trials were designated (refers to fig.6.10) giving attention also to robustness purposes). A first insight of the robustness of the control plant is resumed in fig.6.11 that collects some consideration that was possible to drawn simply attending to the tests. Future works may process all the collected data and study how the variations impact on the controller performances. The data in possession of the experimental tests can be an aid to the research of these uncertainties thanks to the parametric studies carried out during the laboratory activity. This could lead to a redesign of the controller with possibly

improving on the robust stability and robust performance of the system, being aware of the variations and the transfer function of the uncertainties. Of particular interest is what is established in [17], where a study on robust stability and robust performance is carried out for SISO systems. In particular, it shows how to represent the uncertainty of a system and enclose it in a transfer function that combines within it uncertainties on the gain, poles, zeroes and delays of the nominal plant.

In any case the present work proves the robustness properties of the controllers analysed by means of the following factors:

- Both controller are designed for certain values of velocity (SOF for a range, LQG specifically for 45 m/s). Even though these limitations they are able to cover a larger set of velocities.

- the FEM model, and later the ROM, presents a frequency shift due to a correlation not perfect yet. Despite this anomaly the control law succeedes to stabilize the structure well beyond the flutter point.

In particular, as regards the former aspect, the results of tab.7.2 shows as the SOF controller succeedes to keep the system in the stability region for a large values of velocity, increasing its performances moving to 45 m/s. The numerical simulations show stables values of gain and phase margins for both the LQG and SOF controller. This result reflects what was possible to appreciate during the tunnel tests: even though the system was close to instability, both the controllers were able to keep the aircraft in a safety region.
Looking at SOF results, numerical and experimental data exhibit two different trends: with the increasing of velocity the real closed-loop system has an optimal performance as opposite to the mathematical which reveals an unstable tendency at higher velocities. This difference is inherited from the identification phase of sec.7.2.3.

The frequency aspect is very important also for interaction aspect. May happen that approaching to flutter condition a mode could fall in the band of interest of other control laws (flight control system, stability augmentation, gust alleviation etc..) and explode with dangerous couplings ([7] gives an general overview). Even if this will not lead to a complete flutter condition but only to a limit cycle oscillations (LCO) is an occurrence that should be avoided. For this reason controllers able to cover wide modes spectrum are desired. Thus, focusing exclusively on the phase and gain margins is not recommended nowadays, due to the widely application of active control system on airplanes. Further studies should be aimed to this aspect.

Moreover, since now it is available the latest updated model (sec.4.3.3) it could be very interesting to re-tune the controller on the basis of its response and carry out a new wind tunnel test session.

Besides the great risk of flutter constitutes, another reason for which AFS technologies are not approved and installed on flight vehicles is due to structural integrity, in particular for fatigue life and flight comfort. Even in the case flutter mechanism manifests as non-explosive phenomenon, it could give rise to LCOs, very dangerous for fatigue life, or simply acceleration level not acceptable for comfort of passengers. Hence future studies can be focused to implement a cooperation between AFS and dynamic load alleviation systems in order to maintain accelerations level under a certain threshold.

Acronyms

AC Active Control. 17, 28, 141, 153, 154, 161

AFS Active Flutter Suppression. 3, 5, 19, 21, 108, 109, 111, 117, 126, 128, 144, 150, 159, 160, 163

ARMAX Auto Regressive with Moving Average and eXogenous input. 137, 138, 155

ARX Auto Regressive with eXogenous input. 13, 134–138, 145, 147, 149, 155, 156

DAER Aeroespace Engineering Department. 43, 112

DLM Doublet Lattice Method. 30, 32, 37, 131, 160

DMAP Direct Matrix Abstract Program. 109, 110

DoF Degree of Freedom. 31, 34, 70–72, 74, 75, 77–79, 86

FAA Federal Aviation Administration. 18

FEM Finite Element Method. 18, 19, 29, 30, 36, 39, 68, 72–75, 85, 88–92, 105, 107–109, 151, 159, 162

FrF Frequency Response Function. 13, 46–50, 59, 131, 133, 134, 137, 144–149, 153–156

GUI Graphical User Interface. 117, 121, 129, 132

GVT Ground Vibration Test. 11, 38, 43, 44, 46, 47, 56, 78, 79, 86, 87, 89, 91–93, 97–99, 104, 125, 127, 159

ILAF Identical Location of Acceleration and Forces. 12, 111–113, 126

LCO limit cycle oscillations. 162, 163

LE Leading Edge. 13, 119, 120, 137, 145

LQE Linear Quadratic Estimator. 111, 112, 120

LQG Linear Quadratic Gaussian. 13, 15, 111, 119, 120, 125, 127, 141, 143, 144, 149–152, 155, 156, 160, 162

LQR Linear Quadratic Regulator. 112, 114, 120

MA Moving Avarage. 137, 138

MAC Modal Assurance Criterion. 50, 77, 78, 85–87, 98, 99, 104, 160

NeoCASS Next generation Conceptual Aero Structural Sizing. 110

PID Proportional-Integrative-Derivative. 26

PSD Power Spectral Density. 13, 59, 118, 138–140, 142–144

ROM Reduced Order Model. 117, 131, 140, 141

RTAI Real Time Application Interface. 27, 28, 129

SISO Single-Input Single-Output. 153

SOF Static Output Feedback. 15, 116, 119, 120, 127, 130, 133, 136, 141, 142, 144–146, 149, 151, 154–156, 160–162

TE Trailing Edge. 119, 145

X-DIA eXperimental Dipartimento di Ingegneria Aerospaziale. 3, 5, 11, 18, 19, 21–23, 25, 31, 39, 43, 46, 50, 61, 73, 77, 78, 109, 117, 159

Bibliography

[1] BOLZERN, P. G. E., SCATTOLINI, R., AND SCHIAVONI, N. L. *Fondamenti di controlli automatici.* McGraw-Hill, 2008.

[2] CAVAGNA, L., RICCI, S., AND TRAVAGLINI, L. Neocass: an integrated tool for structural sizing, aeroelastic analysis and mdo at conceptual design level. *Progress in Aerospace Sciences 47*, 8 (2011), 621–635.

[3] DE GASPARI, A., AND RICCOBENE, L. Progetto e validazione sperimentale di un modello di ala a freccia negativa con controllo attivo multi-superficie, 2006.

[4] FONTE, F., DE GASPARI, A., RICCOBENE, L., TOFFOL, F., MALIK, S., MARCHETTI, L., RICCI, S., MANTEGAZZA, P., AND LIVNE, E. Numerical and experimental investigations on active flutter suppression technologies.

[5] FONTE, F., RICCI, S., AND MANTEGAZZA, P. Gust load alleviation for a regional aircraft through a static output feedback. *Journal of Aircraft 52*, 5 (2015), 1559–1574.

[6] FRAZER, R. A., DUNCAN, W. J., COLLAR, A. R., ET AL. *Elementary matrices and some applications to dynamics and differential equations*, vol. 1963. Cambridge University Press Cambridge, 1938.

[7] FREYMANN, R. Interactions between an aircraft structure and active control systems. *Journal of Guidance, Control, and Dynamics 10*, 5 (1987), 447–452.

[8] FRIEDLAND, B. *Control System Design: An Introduction to State-Space Methods.* Dover Books on Electrical Engineering. Dover Publications, 2005.

[9] LIVNE, E. Aircraft active flutter suppression: State of the art and technology maturation needs. *Journal of Aircraft 55*, 1 (2018), 410–452.

[10] MARCHETTI, L., DE GASPARI, A., RICCOBENE, L., TOFFOL, F., FONTE, F., RICCI, S., MANTEGAZZA, P., LIVNE, E., AND HINSON, K. A. Active flutter suppression analysis and wind tunnel studies of a commercial transport configuration. In *AIAA Scitech 2020 Forum* (2020), p. 1677.

[11] MORI, A., NARDI, L., AND WYKES, J. Xb-70 structural mode control system design and performance analyses.

[12] NASTRAN, M. Aeroelastic analysis user's guide. *CA, USA, Version 68* (2004).

[13] NASTRAN, M. Design sensitivity and optimization user's guide. *MSC. SOFTWARE* (2004).

[14] NASTRAN, M. Quick reference guide. *MSC. SOFTWARE 1* (2004).

[15] PRANANTA, B., KANAKIS, A., VANKAN, W., AND VAN HOUTEN, M. Model updating of small aircraft dynamic finite element model using standard finite element software.

[16] ROCKLIN, G. Y. A comparison of h1, h2 and hv frequency response functions. In *Proceedings of the 3rd International Modal Analysis Conference, 1985* (1985), pp. 272–278.

[17] SKOGESTAD, S., AND POSTLETHWAITE, I. *Multivariable feedback control: analysis and design*, vol. 2. Wiley New York, 2007.

[18] STANFORD, B. K., AND DUNNING, P. D. Optimal topology of aircraft rib and spar structures under aeroelastic loads. *Journal of Aircraft 52*, 4 (2015), 1298–1311.

[19] VANDERPLAATS, R. Dot–design optimization tools–users manual–version 5.0. *Colorado Springs, Colorado* (1999).

[20] VICOTER. Experimental ground vibration testing of the complete x-diafaa wind tunnel model with pods, 2019.